# ANALYTICAL MODELING AND STABILITY ANAYLSIS OF SPINDLE-HOLDER-TOOL ASSEMBLY BY USING SPINNING AND NON-SPINNING TIMOSHENKO BEAM THEORIES

A THESIS SUBMITTED TO
THE GRADUATE SCHOOL OF NATURAL AND APPLIED SCIENCES
OF
MIDDLE EAST TECHNICAL UNIVERSITY

BY

HASAN YILMAZ

IN PARTIAL FULFILLMENT OF THE REQUIREMENTS
FOR
THE DEGREE OF MASTER OF SCIENCE
IN
MECHANICAL ENGINEERING

JANUARY-2013

Approval of the thesis:

# ANALYTICAL MODELING AND STABILITY ANAYLSIS OF SPINDLE-HOLDER-TOOL ASSEMBLY BY USING SPINNING AND NON-SPINNING TIMOSHENKO BEAM THEORIES

submitted by **HASAN YILMAZ** in partial fulfillment of the requirements for the degree of **Master of Science in Mechanical Engineering Department, Middle East Technical University by,**

Prof. Dr. Canan ÖZGEN
Dean, Graduate School of **Natural and Applied Sciences**

Prof. Dr. Süha ORAL
Head of Department, **Mechanical Engineering**

Assist. Prof. Dr. Ender CİĞEROĞLU
Supervisor, **Mechanical Engineering Dept., METU**

**Examining Committee Members:**

Prof. Dr. Suat KADIOĞLU
Mechanical Engineering Dept., METU

Assist. Prof. Dr. Ender CİĞEROĞLU
Mechanical Engineering Dept., METU

Assist. Prof. Dr. Gökhan O. ÖZGEN
Mechanical Engineering Dept., METU

Assist. Prof. Dr. Yiğit YAZICIOĞLU
Mechanical Engineering Dept., METU

Assist. Prof. Dr. Çağlar BAŞLAMIŞLI
Mechanical Engineering Dept., Hacettepe University

Date: 31.01.2013

**I hereby declare that all information in this document has been obtained and presented in accordance with academic rules and ethical conduct. I also declare that, as required by these rules and conduct, I have full cited and referenced all material and results that are not original to this work.**

Name, Last name : Hasan YILMAZ

Signature :

# ABSTRACT

## ANALYTICAL MODELING AND STABILITY ANAYLSIS OF SPINDLE-HOLDER-TOOL ASSEMBLY BY USING SPINNING AND NON-SPINNING TIMOSHENKO BEAM THEORIES

YILMAZ, Hasan

M. S., Department of Mechanical Engineering
Supervisor: Assist. Prof. Dr. Ender CİĞEROĞLU

January 2013, 75 pages

Chatter in high speed machining is an important problem which affects the product quality and the manufacturing time. In order to determine the optimum cutting parameters such as depth of cut, feed rate, spinning speed etc., dynamic characteristics of the spindle-holder-tool assembly should be modeled accurately. To determine optimum depth of cut and operating speed, frequency response function (FRF) of the tool point is required. However, in high speed machining, due to high rotational speeds, dynamic characteristics are affected by the spinning speed of the spindle. In this thesis, in order to include the effect of spinning speed into the dynamic analysis of the assembly, a spinning Timoshenko Beam Model is used. Spindle-holder-tool assembly is considered to be composed of several free-free beams having different cross-sections, which are coupled with each other by utilizing FRF coupling method. In the assembly, bearings are modeled as a spring and damper combination and structural modification method is used to include their effects. The developed method is verified by comparing the results for zero spinning speed and also the results obtained by FEM. Variation of the natural frequencies and FRF of an example spindle-holder-tool assembly for different spinning speeds are obtained. For non-spinning case, tool point FRF of the assembly is also obtained by using Rayleigh-Ritz method and results of which are compared with coupled system solution.  Finally, stability lobes are obtained for different spin speeds and the effect of gyroscopic forces are studied.

**Keywords:** Spinning Timoshenko Beam Model, Chatter, Frequency Response Function, Receptance Coupling, Rayleigh-Ritz.

# ÖZ

## DÖNEN VE DÖNMEYEN TİMOSHENKO KİRİŞ TEORİLERİNİ KULLANARAK MİL-TUTUCU-UÇ TAKIMININ ANALİTİK MODELLENMESİ VE KARARLILIK ANALİZİ

YILMAZ, Hasan

Yüksek Lisans, Makina Mühendisliği Bölümü
TezYöneticisi: Yrd. Doç. Dr. Ender CİĞEROĞLU

Ocak 2013, 75 sayfa

Tırlama yüksek hızlı talaşlı imalatta ürün kalitesini ve üretim zamanını etkileyen önemli bir problemdir. Kesme derinliği, besleme hızı, dönüş hızı gibi ideal kesme parametrelerinin belirlenmesi için mil-tutucu-uç birleşiminin dinamik sistem karakteristiği hassas bir şekilde modellenmelidir. Optimum kesme derinliği ve operasyon hızının bulunması için uç nokta frekans tepki fonksiyonu (FTF) bulunmalıdır. Ancak yüksek hızlı talaşlı imalatta sistem dinamiği dönüş hızına bağlı olarak etkilenmektedir. Bu tezde dönüş hızının sisteme etkisini modellemek için dönen Timoshenko kiriş modeli kullanılmıştır. Serbest-serbest sınır durumuna sahip farklı çap ve büyüklükteki kirişler birbirlerine FTF birleştirme yöntemi kullanılarak mil-tutucu-uç takımı oluşturulması için birleştirilmişlerdir. Bu takımda rulmanlar, yay ve damper olarak modellenmiş ve sisteme yapısal değişiklik (modifikasyon) yöntemiyle eklenmişlerdir. Geliştirilen model sıfır dönüş hızlı çözümlerle ve sonlu eleman analizleriyle doğrulanmıştır. Farklı dönüş hızlarına göre örnek yapının doğal frekans ve FTF değişimleri bulunmuştur. Dönüş hızının sıfır olduğu durum için Rayleigh-Ritz metodu kullanılarak uç nokta FTF'si bulunmuş ve sonuçları birleştirme yönteminінkilerle kıyaslanmıştır. Sonuç olarak yapının farklı dönüş hızlarına göre kararlılık bölgeleri belirlenmiş ve bunların dönüş hızına göre değişimleri incelenmiştir.

**Anahtar Kelimeler:** Dönen Timoshenko Kiriş Yöntemi, Tırlama, Frekans Tepki Fonksiyonu, Reseptans Birleştirme, Rayleigh-Ritz.

**To My Family**

## ACKNOWLEDGEMENTS

I am grateful to my thesis supervisor Assist. Prof. Dr. Ender CİĞEROĞLU for his guidance, endless support and helpful criticism throughout the progress of my thesis study.

I would like to thank Zekai Murat KILIÇ for his guidance about coupling algorithm.

I would also like to thank Orkun ÖZŞAHİN for his helpful comments about Spinning Timoshenko Beam Model.

I would like to thank Ufuk YİĞİT for his contribution to stability lobes.

I also want to thank my friends in ASELSAN for their helpful support.

I would like to thank Çağrı EMER for his scientific support and helpful comments from very long distance.

The cooperation and friendly support of my colleague Fatih DERE during my master study is kindly acknowledged.

Special thanks go to my father Hasan YILMAZ, my mother Hasine YILMAZ and my sister Fatma YILMAZ for their infinite support and everything they have done in my life.

# TABLE OF CONTENTS

CHAPTERS

APPENDICES

# LIST OF TABLES

TABLES

# LIST OF FIGURES

FIGURES

## LIST OF SYMBOLS

| | |
|---|---|
| $A$ | Area |
| $[A]$ | End point receptance matrix of beam A |
| $c_y$ | Translational damping coefficient |
| $c_\theta$ | Rotational damping coefficient |
| $d_i$ | Inner diameter |
| $d_o$ | Outer diameter |
| $E$ | Young’s Modulus |
| $F(t)$ | Harmonic force in transverse deflection |
| $G$ | Shear Modulus |
| $\gamma$ | Loss factor |
| $I$ | Area moment of inertia |
| $J_z$ | Mass moment of inertia |
| $l$ | Length of beam |
| $\kappa$ | Shear Correction Factor |
| $k_y$ | Translational spring coefficient |
| $k_\theta$ | Rotational spring coefficient |
| $\lambda$ | Eigenvalue |
| $\nu$ | Poisson ratio |
| $\omega$ | Frequency |
| $\Omega$ | Spinning Speed |
| $\rho$ | Density |
| $U$ | Transverse deflection |
| $\Psi$ | Shear Rotation |

# CHAPTER 1

# INTRODUCTION

## 1.1 Literature Review

As the countries become more industrialized, demand for the equipment produced by the industry increases accordingly. Moreover manufacturers try to reach higher production rates day by day. Machining is one of the most commonly used manufacturing methods, which can be described as a controlled material removal from the work piece. In order to supply demanded amount of production, high speed machining is commonly utilized.

In milling and turning operations, high-speed rotation is used to decrease operation time and the manufacturing cost. In addition to the higher speed, depth of cut can also be increased, nevertheless those might cause an unexpected vibration problem called chatter. Chatter is a phenomenon, which results in poor surface quality due to unstable machining operation. When chatter starts chip thickness is not stable anymore and it leaves wavy, undesired surface finish. Not only negative effect of chatter might be seen on the work piece but also tool and structure life could be degraded. In order to maximize economical gain, operating speed should be increased and negative effects of chatter on the work piece surface needs to be eliminated. Therefore, it is absolutely necessary that stable and unstable operating areas should be determined for the working machine. In Figure 1.1 example of a stability lobe diagram is shown.

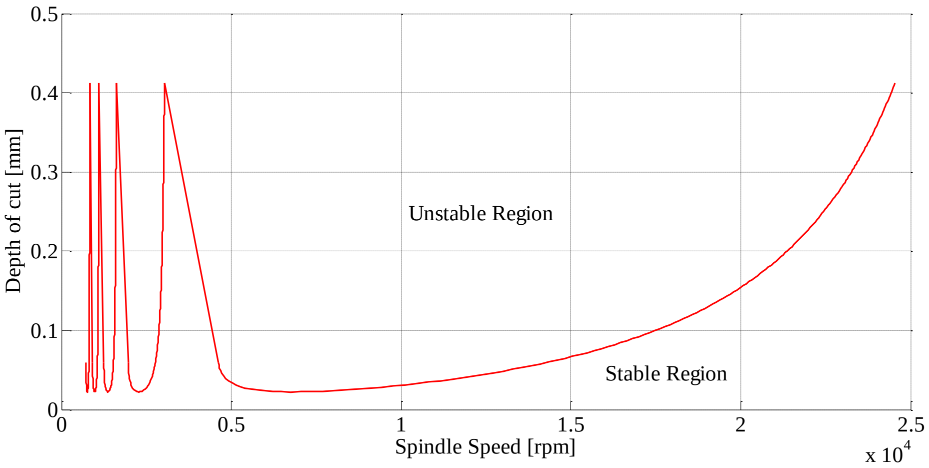

Figure 1.1 Example Stability Lobe Diagram

Regenerative chatter in orthogonal cutting was first explained by Tobias and Fishwick [1] and Tlusty and Polacek [2]. Merritt [3] proposed stability lobe calculations considering orthogonal cutting conditions. Orthogonal cutting is a time invariant process and limiting depth of cut in orthogonal cutting depends on Frequency Response Functions (FRF) of the tool point and cutting coefficient. Altintas [4] explained construction of stability lobes for orthogonal cutting operations using acquired FRF in detail.

Milling stability analysis is different than orthogonal cutting process. It includes time dependent geometry and variables. Tool contains a certain number of teeth and cutting forces also change with respect to rotation of the tool. Firstly, Tlusty and Koenigsberger [5] used orthogonal cutting formula assuming average cutting direction and average cutting teeth in order to simulate milling stability lobes. Sridhar [6] came up with an improved milling model described by differential equations with periodic coefficients. Minis and Yanushevsky [7] applied Fourier series expansion to the Floquet's theorem and obtained milling stability model. Altıntaş and Budak [8] developed an analytical stability method for milling process. In their study frequency domain is used and very fast and accurate results are obtained. Directional coefficients are related with immersion angles which depend on the type of milling. Altıntaş [4] also mentioned about this technique and showed some numerical examples. In this thesis for milling stability lobes equations given by reference [8] are used.

Excessive vibrations are observed when the exciting frequency of the structure is close to the chatter frequency. Dynamics of structure has a direct effect on the stability lobes. In order to construct reliable stability lobes, structural vibration information belonging to the real operating condition is required. This information could be obtained by impact hammer test in which an accelerometer is placed on the tool tip and system is excited by impact hammer in order to measure the response of the system. After analyzing harvested data, required tool point FRF is utilized in stability lobe calculations. On the other hand, experimental methods might not give accurate results, as it depends heavily on the accuracy of the experimental set-up. In addition, operational conditions such as rotational effects are hard to include into the results as it requires operational testing. Furthermore, if any change is required on the spindle-holder-tool assembly, tremendous time is needed for each iteration on the system. Therefore, before going deep into the experimental analysis, analytical model results are very helpful for the verification of the process.

Milling machine assembly is composed of spindle, holder and tool subassemblies. Spindle subassembly consists of main shaft and bearings that connect shaft to the main housing. Spindle shaft, holder and tool subassemblies are composed of several numbers of beams. Therefore, beam theories are to be investigated deeply. There are different beam theories in the literature. Euler beam theory is the simplest beam theory, which is also known as the classical beam theory and neglects shear deformation and rotary inertia. In Rayleigh beam theory, rotary inertia is added on top of the Euler beam model. The most commonly used model is Timoshenko beam model [9]. Since rotary inertia and shear deformation is included in Timoshenko beam model, it is very useful for modeling thick beams. Zu [10] added spinning effect to the Timoshenko beam model and obtained mode shapes for different boundary conditions.

On the other hand, shear correction factor should be defined in Timoshenko beam model. Cowper [11] advised shear correction factors considering different cross sections. Hutchinson [12] derived improved shear correction factors for Timoshenko beam model. Instead of Timoshenko's model, Levinson [13] proposed a higher order beam model (HOBM) which no longer needs shear correction factor. Eisenberger [14] compared HOBM and Timoshenko beam model considering different shear correction factors. Soldatos [15] derived characteristic equations and mode shapes for HOBM considering generally known boundary conditions.

In order to construct spindle shaft, beams can be coupled together using receptance coupling method. Schmitz [16] proposed receptance coupling method which is used in this thesis. Although it consumes longer time, impedance coupling method can be used as well.

Bearings are mounted on the main shaft in order to support it from various locations. Two sets of bearings are usually placed as front and rear bearings. Aim of the bearing is to resist axial and radial cutting forces. Preload is applied to the bearings in order to make them work stable in the operating conditions. Angular contact ball bearings are commonly used in order to withstand axial and radial forces. Analytically, bearings are modeled as a spring and damper combination. Arakere [17] proposed spring and damping coefficients for the spindle bearings. Özgüvens's structural modification method [18] is used to add bearings to the system.

Not only bearings but also interfaces between spindle-holder and holder-tool are modeled as a spring and damper combination. Schmitz's method [16] can be used in flexible connections as well. Namazi [19] studied contact parameters between spindle and tool holder connection. Cao [20] and Schmitz [21] investigated second generation contacts extensively. In their work, contact parameters are measured with respect to different overhang tool lengths and they are fitted into the analytical model accordingly. Özşahin [22] applied neural network analysis to the measured contact parameters in order to predict those parameters considering different cases.

Whole assembly can be constructed by analytical model or using FEM. Movahhedy [23] outlined FEM of the full assembly including gyroscopic effects. It is claimed in this work that gyroscopic effects lower the axial depth of cut. Altintaş and Cao [24] showed spindle-bearing model and investigated the effect of preload force on the natural frequencies of the assembly. In addition, forward and backward natural frequencies are expressed in detail. Ertürk [25] constructed analytical model of spindle-holder-tool assembly. In his work, natural frequencies of the system are identified and effect of change in bearing and contact parameters are observed for the assembly extensively. Kılıç [26] used a nonlinear bearing model and examined the effect of nonlinearity on the stability lobes. Nonlinear bearing model is an important research topic as bearing itself is a nonlinear model. Hence balls of bearings makes a point touch with the inner and outer races of the bearing. Stiffness of bearing changes with respect to spindle speed. Another uncertainty source for the bearings is temperature. After long period of operation, temperature of bearings may be increased. Inevitably, stiffness properties of bearings are affected by temperature changes.

## 1.2 Objective

The aim of this study is to obtain chatter free operating range for the milling machines considering different spindle speeds. Effect of spinning speed is included using spinning Timoshenko beam model in the calculations. Different case studies are obtained in order to investigate the change in the tool point FRF and stability lobes with respect to spinning speed. In addition, it is aimed to utilize Rayleigh-Ritz method in construction process of spindle-holder-tool assembly as an alternative to coupling of beams. Results of two methods are compared using different case studies.

## 1.3 Scope of the Thesis

The outline of the thesis is given as follows:

In Chapter 2, Spinning Timoshenko Beam model is explained in order to obtain dynamic characteristics of a simple beam component. Natural frequencies and mode shapes are obtained for simple beam under free-free end conditions. Besides, Eigenfunction expansion method is applied to find the receptance of the beam. Bickford HOBM is detailed and natural frequency equations for free-free end conditions are given. Also, rigid beam coupling and impedance coupling is described in order to obtain the end point receptances of rigidly coupled beams. Afterwards, structural modification method is presented which is used to add bearing properties on to the spindle assembly. In addition, elastic coupling method is considered for the connection of the holder and tool subassemblies. Rayleigh Ritz method for Timoshenko beam model is presented in order to find approximate natural frequencies and mode shapes of the spindle assembly. Also, FEM of the assembly is briefly explained.

In Chapter 3, cutting geometry and force equations for orthogonal cutting are explained. Limiting depth of cut equation for orthogonal cutting is obtained. For milling operation, related directional cutting coefficients are studied and limiting depth of cut equation is given.

In Chapter 4, using spindle geometry and other related design parameters, tool point FRF of the system is obtained. Case studies are performed with changing the spindle speed of the assembly. Using the obtained FRF information, stability lobes are constructed and they are compared with each other in order to find the effect of spinning speed. Timoshenko and higher order beam models are compared in order to observe the effect of shear coefficient in the model. In addition, approximate Rayleigh-Ritz solution is compared with coupled system solution and FEM solution for zero spin speed. Recommendations are given according to these results in order to obtain chatter free operating range.

In Chapter 5, conclusions are made considering results of Chapter 4 and suggestions for the future work are proposed.

Conference papers related with this thesis are given in the Appendices.

# CHAPTER 2

# MODELING OF SPINDLE ASSEMBLY

## 2.1 Beam Models

In literature, there exist several beam theories which are used to obtain structural and modal characteristics of beams. First beam theory is Euler beam theory. It neglects shear deformation and rotary inertia. If thin beams (high slenderness ratio) are considered, it is seen that shear deformation and rotary inertia have less impact on the beam characteristic. As a result, Euler beam model gives acceptable results for these types of beams. In Rayleigh beam theory, rotary inertia is added on to the Euler beam theory. Rayleigh beam model is more precise than Euler's theory. Later, Timoshenko [9] added both shear deformation and rotary inertia on to the Euler beam model. If thick beams are considered, shear deformation has more important role in beam dynamics. Thus, Timoshenko's model gives more accurate results with respect to Euler's and Rayleigh's beam models. Comparison of those beam theories are given by [27] in detail.

In order to compare dynamics of rotating structure with the nonrotating one, spinning Timoshenko beam model is used in this study. Analytical solution for the spinning Timoshenko beam model for various boundary conditions is given by Zu [10]. Separation in natural frequencies which are known as forward and backward natural frequencies is observed in spinning beam model solution. It is seen that amount of separation of natural frequencies depends on the spinning speed.

One deficiency of Timoshenko beam model is that shear correction factor should be defined for the beam model. Cowper [11] recommended applicable shear correction factors considering different cross sections of beams, for example circular and hollow cross sections.

In HOBM model, deformed plane can have both shear rotation and warping in addition to the Timoshenko beam model. Thus, HOBM eliminates the shear correction factor requirement in equations as it includes warping function.

In this thesis Spinning Timoshenko beam model and HOBM are used in beam modeling. Results of these two models are compared with nonrotating Timoshenko beam results. In the next section, spinning Timoshenko beam model and HOBM are explained in detail.

### 2.1.1 Spinning Timoshenko Beam Model

In this model, to simulate each beam segment, spinning Timoshenko beam model with free-free boundary conditions is used. Coordinate frame and rotation axis for a finite length free- free beam is shown in Figure 2.1.

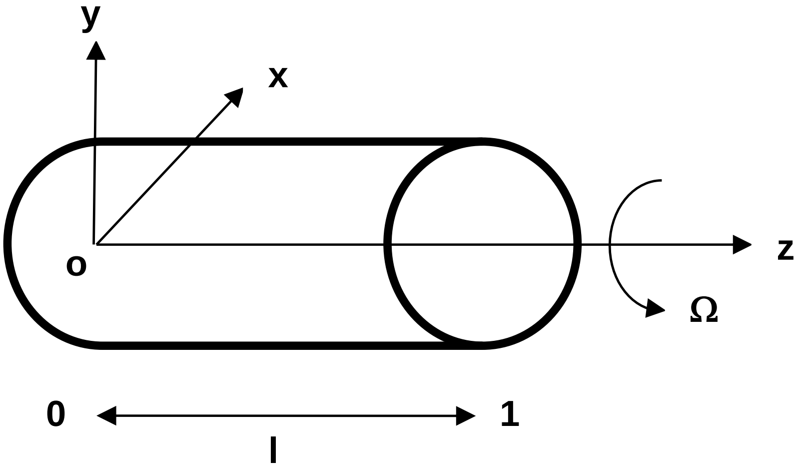

Figure 2.1 Reference Frame for Spinning Shaft

In order to derive equations of motion, kinetic and potential energy equations are obtained and then Hamilton’s Principle is applied. Non-dimensional partial differential equations of motion are given as follows by Zu [10]:

$$\frac{\partial^2 u}{\partial t^2}+\frac{\kappa G}{\rho l^2}\left(l\frac{\partial \psi}{\partial \zeta}-\frac{\partial^2 u}{\partial \zeta^2}\right)=F, \tag{2.1}$$

$$\frac{\partial^2 \psi}{\partial t^2}-i\frac{\Omega J_z}{\rho I}\frac{\partial \psi}{\partial t}-\frac{E}{\rho l^2}\frac{\partial^2 \psi}{\partial \zeta^2}+\frac{\kappa AG}{\rho Il}\left(l\psi-\frac{\partial u}{\partial \zeta}\right)=0\,, \tag{2.2}$$

where $u$ is the transverse displacement, $\psi$ is the bending angle of the beam, $F$ is the applied transverse force, $\rho$ is density, $I$ is transverse moment of inertia, $J_z$ is polar mass moment of inertia, $E$ is Young`s modulus, $G$ is shear modulus, $A$ is area, $\Omega$ is spin speed $\kappa$ is shear correction coefficient and $\zeta$ is the non-dimensional axial position which is equal to $z/l$ . $z$ is axial position on the beam and $l$ is total length of the beam. Cowper [11] recommended shear factor coefficient for hollow circular cross sections as follows,

$$\kappa=\frac{6(1+\nu)(1+(di/do)^2)^2}{(7/6\nu)(1+(di/do)^2)^2+(20+12\nu)(di/do)^2}\,, \tag{2.3}$$

where $di$ and $do$ are inner and outer diameters of beams and $\nu$ is Poisson ratio of beam. Uncoupled equations of motion for the spinning Timoshenko beam with $F=0$ is obtained using Eqs. (2.1) and (2.2) as follows,

$$\frac{\rho^2 I}{\kappa G}\frac{\partial^4 u}{\partial t^4}-i\Omega\frac{\rho J_z}{\kappa G}\frac{\partial^3 u}{\partial t^3}+\rho A\frac{\partial^2 u}{\partial t^2}-\frac{\rho I}{l^2}\left(1+\frac{E}{\kappa G}\right)\frac{\partial^4 u}{\partial \zeta^2 \partial t^2}+i\Omega\frac{J_z}{l^2}\frac{\partial^3 u}{\partial \zeta^2 \partial t}+\frac{EI}{l^4}\frac{\partial^4 u}{\partial \zeta^4}=0, \tag{2.4}$$

$$\frac{\rho^2 I}{\kappa G}\frac{\partial^4 \psi}{\partial t^4}-i\Omega\frac{\rho J_z}{\kappa G}\frac{\partial^3 \psi}{\partial t^3}+\rho A\frac{\partial^2 \psi}{\partial t^2}-\frac{\rho I}{l^2}\left(1+\frac{E}{\kappa G}\right)\frac{\partial^4 \psi}{\partial \zeta^2 \partial t^2}+i\Omega\frac{J_z}{l^2}\frac{\partial^3 \psi}{\partial \zeta^2 \partial t}+\frac{EI}{l^4}\frac{\partial^4 \psi}{\partial \zeta^4}=0\,. \tag{2.5}$$

In Eqs. (2.1), (2.2), (2.4) and (2.5),

$$u=u_x+iu_y\,, \tag{2.6}$$

$$\psi = \psi_x + i\psi_y , \tag{2.7}$$

where $u_x$ and $u_y$ are the deflections of the beam in $x$ and $y$ directions, respectively. Similarly, $\psi_x$ and $\psi_y$ are the corresponding bending angles in $x$ and $y$ directions. Boundary conditions for the free-free beam can be given as follows,

$$\begin{aligned} &\psi'(\zeta_0, t) = 0, \quad \zeta_0 = 0,1 \\ &\frac{1}{l}u'(\zeta_0, t) - \psi(\zeta_0, t) = 0, \quad \zeta_0 = 0,1. \end{aligned} \tag{2.8}$$

The following forms of solutions satisfy the partial differential equations given by Eqs. (2.4) and (2.5)

$$u(\zeta, t) = U_0 e^{ik_u\zeta} e^{i\omega t} , \tag{2.9}$$

$$\psi(\zeta, t) = \Psi_0 e^{ik_\psi\zeta} e^{i\omega t} , \tag{2.10}$$

where $U_0$ and $\Psi_0$ are complex amplitudes and $\omega$ is the natural frequency. It should be noted that, there is no damping in the free-free system. Substituting Eqs. (2.9) and (2.10) into Eqs. (2.4) and (2.5), the following relations are obtained,

$$ak_u^{\ 4} - bk_u^{\ 2} + c = 0 , \tag{2.11}$$

$$ak_\psi^{\ 4} - bk_\psi^{\ 2} + c = 0 . \tag{2.12}$$

In these equations $k_u$ and $k_\psi$ indicate the normal modes of the solution. Coefficients of these equations are given as

$$a = \frac{EI}{l^4 \rho \mathrm{A}}, \quad b = \frac{I}{l^2 \mathrm{A}}\left(1 + \frac{E}{\kappa G}\right)\omega^2 - \frac{\Omega J_z}{l^2 \rho \mathrm{A}}\omega, \quad c = \frac{\rho I}{\kappa \mathrm{A} G}\omega^4 - \frac{\Omega J_z}{\kappa \mathrm{A} G}\omega^3 - \omega^2 . \tag{2.13}$$

Since the constants of Eqs. (2.11) and (2.12) are the same, their solutions are also same as well and both depends on $\omega$. Two different forms of solutions are obtained for $\sqrt{b^2 - 4ac} > b$ and $\sqrt{b^2 - 4ac} < b$. For the former case the solution becomes,

$$k_{1,2} = \pm i s_1, \pm s_2 \tag{2.14}$$

where

$$s_1 = \sqrt{\frac{-b + \sqrt{b^2 - 4ac}}{2a}} , \tag{2.15}$$

$$s_2 = \sqrt{\frac{b + \sqrt{b^2 - 4ac}}{2a}} . \tag{2.16}$$

Using Eqs. (2.15) and (2.16) normal modes of $u$ and $\psi$ can be obtained as follows,

$$U(\zeta) = \mathrm{A}_1 \cosh(s_1\zeta) + \mathrm{A}_2 sinh(s_1\zeta) + \mathrm{A}_3 \cos(s_2\zeta) + \mathrm{A}_4 \sin(s_2\zeta) , \tag{2.17}$$

$$\Psi(\zeta) = \mathrm{A}_1' \sinh(s_1\zeta) + \mathrm{A}_2' \cos h(s_1\zeta) + \mathrm{A}_3' \sin(s_2\zeta) + \mathrm{A}_4' \cos(s_2\zeta) , \tag{2.18}$$

where,

$$A_1' = c_1 A_1, \quad A_2' = c_1 A_2, \quad A_3' = c_2 A_3, \quad A_4' = -c_2 A_4 , \tag{2.19}$$

$$c_i = \frac{1}{s_i}\left(\frac{\rho l}{\kappa G}\omega^2 + (-1)^{i+1}\frac{1}{l}s_i^{\ 2}\right), \quad i = 1,2 . \tag{2.20}$$

For $\sqrt{b^2-4ac}<b$, the solution becomes,

$$k_{1,2}=\pm s_1', \pm s_2, \tag{2.21}$$

where,

$$s_1'=\sqrt{\frac{b-\sqrt{b^2-4ac}}{2a}}\ . \tag{2.22}$$

Using Eqs. (2.16) and (2.22) normal modes of $u$ and $\psi$ can be found as follows

$$U(\zeta)=\mathrm{A}_1\cos(s_1'\zeta)+\mathrm{A}_2 \mathit{sin}(s_1'\zeta)+\mathrm{A}_3\cos(s_2\zeta)+\mathrm{A}_4\sin(s_2\zeta), \tag{2.23}$$

$$\Psi(\zeta)=\mathrm{A}_1'\sin(s_1'\zeta)+\mathrm{A}_2'\cos(s_1'\zeta)+\mathrm{A}_3'\sin(s_2\zeta)+\mathrm{A}_4'\cos(s_2\zeta), \tag{2.24}$$

where ,

$$A_1'=c_1'A_1,\ A_2'=-c_1'A_2,\ A_3'=c_2A_3,\ A_4'=-c_2A_4, \tag{2.25}$$

$$c_1'=\frac{1}{s_1'}\left(\frac{\rho l}{\kappa G}\omega^2+\frac{1}{l}s_1'^2\right). \tag{2.26}$$

In order to obtain the solution, free-free end boundary conditions given in Eq. (2.8) are applied to Eqs. (2.17), (2.18), (2.23) and (2.24). Then the characteristic equations and the mode shapes for free-free boundary condition are obtained. For the case of $\sqrt{b^2-4ac}>b$, they are given as,

$$\begin{aligned}&c_1s_1\left(\frac{1}{l}s_1-c_1\right)\left[\cosh(s_1)-\cos(s_2)\right]^2-\left(c_1s_1\sinh(s_1)-\frac{s_1/l-c_1}{s_2/l+c_2}c_2s_2\sin(s_2)\right)\\&*\left[\left(\frac{1}{l}s_1-c_1\right)\sinh(s_1)+\frac{c_1s_1}{c_2s_2}\left(\frac{1}{l}s_2+c_2\right)\sin(s_2)\right]=0\end{aligned}\ , \tag{2.27}$$

$$U(\zeta)=U_0\left[\cosh(s_1\zeta)-\frac{d}{s_1/l-c_1}\sinh(s_1\zeta)-\frac{c_1s_1}{c_2s_2}\cos(s_2\zeta)+\frac{d}{s_2/l+c_2}\sin(s_2\zeta)\right], \tag{2.28}$$

$$\Psi(\zeta)=\Psi_0\left[c_1\sinh(s_1\zeta)-\frac{dc_1}{s_1/l-c_1}\cosh(s_1\zeta)-\frac{c_1s_1}{s_2}\sin(s_2\zeta)-\frac{dc_2}{s_2/l+c_2}\cos(s_2\zeta)\right], \tag{2.29}$$

where,

$$d=\frac{\left(\frac{1}{l}s_1-c_1\right)\sinh(s_1)+\frac{c_1s_1}{c_2s_2}\left(\frac{1}{l}s_2+c_2\right)\sin(s_2)}{\cosh(s_1)-\cos(s_2)}\ . \tag{2.30}$$

For the case of $\sqrt{b^2-4ac}<b$, the characteristic equation and the mode shapes become as follows,

$$\begin{aligned}&c_1's_1'\left(\frac{1}{l}s_1'+c_1'\right)\left[\cos(s_1')-\cos(s_2)\right]^2+\left(c_1's_1'\sin(s_1')-\frac{s_1'/l+c_1'}{s_2/l+c_2}c_2s_2\sin(s_2)\right)\\&*\left[\left(\frac{1}{l}s_1'+c_1'\right)\sin(s_1')-\frac{c_1's_1'}{c_2s_2}\left(\frac{1}{l}s_2+c_2\right)\sin(s_2)\right]=0,\end{aligned} \tag{2.31}$$

$$U(\zeta)=U_0\left[\cos(s_1'\zeta)+\frac{d'}{s_1'/l-c_1'}\sin(s_1'\zeta)-\frac{c_1's_1'}{c_2s_2}\cos(s_2\zeta)-\frac{d'}{s_2/l+c_2}\sin(s_2\zeta)\right], \tag{2.32}$$

$$\Psi(\zeta)=\Psi_0\left[c_1'\sin(s_1'\zeta)-\frac{d'c_1'}{s_1'/l+c_1'}\cos(s_1'\zeta)-\frac{c_1's_1'}{s_2}\sin(s_2\zeta)+\frac{d'c_2}{s_2/l+c_2}\cos(s_2\zeta)\right], \tag{2.33}$$

$$d'=\frac{\left(\frac{1}{l}s_1'+c_1'\right)\sin(s_1')-\frac{c_1's_1'}{c_2s_2}\left(\frac{1}{l}s_2+c_2\right)\sin(s_2)}{\cos(s_1')-\cos(s_2)}. \tag{2.34}$$

Natural frequencies of the beam can be found by searching roots of Eqs. (2.27) and (2.31). If obtained natural frequencies are put into Eqs. (2.28), (2.29), (2.32) and (2.33), related mode shapes can be found. Interesting point in spinning beam model is that dynamic characteristics of rotating beams change with respect to the spinning speed. Natural frequencies split as backward and forward natural frequencies. As spinning speed increases, difference between backward and forward natural frequencies increases as well. Example of natural frequency split will be explained in the following sections. There are translational and rotational rigid body modes for free-free beam which are given as follows,

$$\begin{aligned}
&U_{tr}(\zeta)=A_{tr},\\
&\Psi_{tr}(\zeta)=0,\\
&U_{rot}(\zeta)=A_{rot}(\zeta l-l/2),\\
&\Psi_{rot}(\zeta)=A_{rot}.
\end{aligned} \tag{2.35}$$

If mass normalization is applied to rigid body modes, $A_{tr}$ and $A_{rot}$ are obtained as follows,

$$\begin{aligned}
&A_{tr}=\frac{1}{\sqrt{l\rho\mathrm{A}}},\\
&A_{rot}=\frac{1}{\sqrt{\rho lI+\frac{\rho Al^3}{12}}}.
\end{aligned} \tag{2.36}$$

Since the Eqs. (2.1) and (2.2) are not orthogonal, in order to find the response of the beam to an applied force and moment, state space representations of Eqs. (2.1) and (2.2) are formed.

$$[M]\{\dot{W}(\zeta,t)\}-[K]\{W(\zeta,t)\}=\{F\}, \tag{2.37}$$

$$\{W\}=\{\dot{U}(\zeta,t)\ \ U(\zeta,t)\ \ \dot{\Psi}(\zeta,t)\ \ \Psi(\zeta,t)\}^T, \tag{2.38}$$

$$\{F\}=\{0\ \ F\ \ 0\ \ 0\}^T, \tag{2.39}$$

where $[M]$ and $[K]$ matrices are given as follows

$$[M]=\begin{bmatrix}0 & \rho A & 0 & 0\\ \rho A & 0 & 0 & 0\\ 0 & 0 & 0 & \rho I\\ 0 & 0 & \rho I & -i\Omega J_z\end{bmatrix},\quad [K]=\begin{bmatrix}\rho A & 0 & 0 & 0\\ 0 & \frac{\kappa AG}{l^2}\frac{\partial^2}{\partial\zeta^2} & 0 & -\frac{\kappa AG}{l}\frac{\partial}{\partial\zeta}\\ 0 & 0 & \rho I & 0\\ 0 & \frac{\kappa AG}{l}\frac{\partial}{\partial\zeta} & 0 & \frac{E}{l}\frac{\partial^2}{\partial\zeta^2}-\kappa AG\end{bmatrix}. \tag{2.40}$$

In state space representation matrix size is increased from 2x2 to 4x4 and consequently Eq. (2.37) becomes orthogonal. Using the modal expansion theorem, solution of this system can be written in terms of its mode shapes as

$$\{W(\zeta,t)\} = \sum_{r=-N_m}^{N_m} z_r(t)\{W_r(\zeta)\}, \tag{2.41}$$

where $z_r$ is the modal coefficient of the $r^{th}$ mode. Multiplying each side of Eq.(2.37) by $\{W_s\}^T$, integrating over the length and using the orthogonality conditions, the following equation of motion is obtained;

$$M_r\dot{z}_r(t) - K_r z_r(t) = Q_r(t), \tag{2.42}$$

where $M_r$, $K_r$ and $Q_r(t) = U_r(\zeta_k)F(t)$ are the modal mass, modal stiffness and the modal forcing for the $r^{th}$ mode, respectively. Solution of this uncoupled differential equation for a harmonic forcing of $F(t) = Fe^{i\omega t}$ applied at $\zeta = \zeta_k$ becomes as follows

$$z_r(t) = \frac{U_r(\zeta_k)Fe^{i\omega t}}{M_r(i\omega - \lambda_r)}, \tag{2.43}$$

where $\lambda_r$ is $i\omega_r$ and $\omega_r$ is natural frequency at $r^{th}$ mode. $U_r(\zeta_k)$ and $\omega_r$ values can be directly taken from Eqs. (2.28),(2.32), (2.27) and (2.31). Total response of the beam becomes as follows,

$$\{W(\zeta,t)\} = \sum_{r=-N_m}^{N_m} \frac{U_r(\zeta_k)Fe^{i\omega t}}{M_r(i\omega - \lambda_r)}\{W_r(\zeta)\} \tag{2.44}$$

where $N_m$ is the number of modes used in the modal expansion. Using the mass normalized eigenfunctions, receptances of the end points of the free-free beam can be obtained for a transverse forcing applied on the beam. Receptance functions are denoted as $H_{jk}, N_{jk}, L_{jk}, P_{jk}$. $H_{jk}$ and $L_{jk}$ represent linear displacement receptance of point $j$ due to a unit force and moment applied at point $k$, respectively. Similarly, $N_{jk}$ and $P_{jk}$ represent angular displacement receptance of point $j$ due to a force and moment applied at point $k$, respectively. Small structural damping is assumed as $(1+i\gamma)$. Following a similar procedure, receptance for an applied moment can be obtained and all these receptances can be defined as follows,

$$\begin{aligned}
H_{jk} &= \sum_{r=-N_m}^{N_m} \frac{U_r(\zeta_j)U_r(\zeta_k)}{i\omega - \lambda_r(1+i\gamma)}, \quad & N_{jk} &= \sum_{r=-N_m}^{N_m} \frac{\Psi_r(\zeta_j)U_r(\zeta_k)}{i\omega - \lambda_r(1+i\gamma)}, \\
L_{jk} &= \sum_{r=-N_m}^{N_m} \frac{U_r(\zeta_j)\Psi_r(\zeta_k)}{i\omega - \lambda_r(1+i\gamma)}, \quad & P_{jk} &= \sum_{r=-N_m}^{N_m} \frac{\Psi_r(\zeta_j)\Psi_r(\zeta_k)}{i\omega - \lambda_r(1+i\gamma)},
\end{aligned} \tag{2.45}$$

where $\gamma$ is the loss factor for structural damping, which is assumed to be a very small value (0.002) in the case studies considered.

### 2.1.2 Higher Order Beam Model

Deformed plane cross-sections for Euler, Timoshenko and higher order beams are given in Figure 2.2. HOBM is firstly explained by [13, 28, 33] and it allows rotation and warping of deformed cross section which can be seen in Figure 2.2.c. In other words, it has shear distribution over the cross section and the need for a shear correction factor is eliminated.

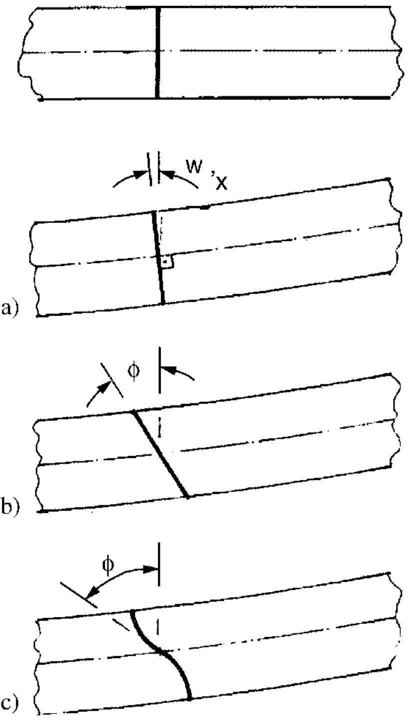

Figure 2.2 Cross-section Displacements in Different Beam Theories: (a) Bernoulli-Euler Beam; (b) Timoshenko Beam; and (c) High Order Beam Theory [14]

Natural frequencies and mode shapes of rectangular beams with different boundary conditions are given by Soldatos [15] in detail. Uncoupled equations of motion for transverse deflection and shear rotation are given below,

$$\frac{\partial^6 u}{\partial \zeta^6}+(2\Lambda^2+A_1)\frac{\partial^4 u}{\partial \zeta^4}+(\Lambda^4+(A_1+A_2)\Lambda^2)\frac{\partial^2 u}{\partial \zeta^2}+(A_2\Lambda^4-kA_1\Lambda^2)u=0, \tag{2.46}$$

$$\frac{\partial^6 \psi}{\partial \zeta^6}+(2\Lambda^2+A_1)\frac{\partial^4 \psi}{\partial \zeta^4}+(\Lambda^4+(A_1+A_2)\Lambda^2)\frac{\partial^2 \psi}{\partial \zeta^2}+(A_2\Lambda^4-kA_1\Lambda^2)\psi=0, \tag{2.47}$$

where

$$\begin{aligned} A_1&=\frac{A_{55}L^2}{A'D^c_{11}},\quad A_2=\frac{\rho_0\rho_{02}L^2}{A'\rho_2^{\,2}},\\ A'&=\frac{\rho_{11}^{\,2}-\rho_2\rho_{02}}{\rho_2^{\,2}},\quad k=\frac{\rho_0L^2}{\rho_2},\quad \Lambda^2=\frac{\omega^2\rho_2L^2}{D^c_{11}}. \end{aligned} \tag{2.48}$$

Terms in Eq. (2.48) include rigidity and elastic stiffness terms which are given below;

$$\begin{aligned} A_{55}&=\int_{-h/2}^{h/2} Q_{55}\left[\phi'(z)\right]^2 dz,\quad D^c_{11}=\int_{-h/2}^{h/2} Q_{11}z^2dz,\\ \rho_i&=\int_{-h/2}^{h/2} b\rho z^i dz,\quad \rho_{ij}=\int_{-h/2}^{h/2} b\rho z^i\left[\phi(z)\right]^j dz,\quad \phi(z)=z\left(1-\frac{4z^2}{3h^2}\right). \end{aligned} \tag{2.49}$$

Here, $b$ is the width of the beam, $h$ is the height of beam and $\rho$ is the density. If isotropic beams are considered, $Q_{11}$ is equal to $E$ and $Q_{55}$ is equal to $G$. $\phi(z)$ is the shape function which introduces warping effect into the plane section of the deformed beam as shown in Figure 2.2.c. Eqs. (2.46) and

(2.47) are 6th order differential equations and both have the same solution. In order to solve these differential equations, Eqs. (2.46) and (2.47) are converted into the following form,

$$\lambda^6 + (2\Lambda^2 + A_1)\lambda^4 + (\Lambda^4 + (A_1 + A_2)\Lambda^2)\lambda^2 + (A_2\Lambda^4 - kA_1\Lambda^2) = 0. \tag{2.50}$$

Eq.(2.50) is actually third order polynomial in terms of $\lambda^2$ and the resulting six roots can be obtained exactly as follows,

$$\lambda_i^2 = \mu_i - \frac{1}{3}(2\Lambda^2 + A_1), \tag{2.51}$$

where

$$\begin{aligned} \mu_1 &= -\left[\frac{16(r^2 - s^2)}{27}\right]^{1/6} \cos\left[\frac{1}{3}\tan^{-1}\left(\frac{s}{r}\right) + \frac{\pi}{3}\right], \\ \mu_2 &= -\left[\frac{16(r^2 + s^2)}{27}\right]^{1/6} \cos\left[\frac{1}{3}\tan^{-1}\left(\frac{s}{r}\right) - \frac{\pi}{3}\right], \\ \mu_3 &= \left[\frac{16(r^2 + s^2)}{27}\right]^{1/6} \cos\left[\frac{1}{3}\tan^{-1}\left(\frac{s}{r}\right)\right], \end{aligned} \tag{2.52}$$

$$r = 3\sqrt{3}\left[\frac{2}{27}\left(A_1 + 2\Lambda^2\right)^3 - \frac{1}{3}\left(A_1 + 2\Lambda^2\right)\left(A_1 + A_2 + \Lambda^2\right)\Lambda^2 + \left(A_2\Lambda^2 - kA_1\right)\Lambda^2\right], \tag{2.53}$$

$$s^2 = 4\left[\frac{1}{3}\left(2\Lambda^2 + A_1\right)^2 - \left(A_1 + A_2 + \Lambda^2\right)\Lambda^2\right]^3 - r^2. \tag{2.54}$$

Having obtained roots the ( $\lambda_i$ ) of Eq.(2.50), general solution of Eqs. (2.46) and (2.47) can be obtained as well. There are two different cases in the solution. In the first case, non-dimensional natural frequency is smaller than pure shear frequency. However in the second case, it is bigger than pure shear frequency. Non-dimensional natural frequency and pure shear frequency are given as follows,

$$\begin{aligned} \bar{\omega}^2 &= \omega^2 \frac{\rho_0 L^4}{D^c_{11}}, \\ \eta_B &= 12\left(\frac{L}{h}\right)^2 \sqrt{\frac{14Q_{55}}{17Q_{11}}}. \end{aligned} \tag{2.55}$$

For the case $\bar{\omega} < \eta_B$ general solution is given below,

$$U(\zeta) = C_1\cos(\lambda_1\zeta) + C_2 sin(\lambda_1\zeta) + C_3\cosh(\lambda_2\zeta) + C_4\sinh(\lambda_2\zeta) + C_5\cosh(\lambda_3\zeta) + C_6\sinh(\lambda_3\zeta), \tag{2.56}$$

$$\Psi(\zeta) = D_1\cos(\lambda_1\zeta) + D_2 sin(\lambda_1\zeta) + D_3\cosh(\lambda_2\zeta) + D_4\sinh(\lambda_2\zeta) + D_5\cosh(\lambda_3\zeta) + D_6\sinh(\lambda_3\zeta). \tag{2.57}$$

If $\bar{\omega} > \eta_B$,

$$U(\zeta) = E_1\cos(\lambda_1\zeta) + E_2 sin(\lambda_1\zeta) + E_3\cos(\lambda_4\zeta) + E_4\sin(\lambda_4\zeta) + E_5\cosh(\lambda_3\zeta) + E_6\sinh(\lambda_3\zeta), \tag{2.58}$$

$$\Psi(\zeta) = F_1\cos(\lambda_1\zeta) + F_2 sin(\lambda_1\zeta) + F_3\cos(\lambda_4\zeta) + F_4\sin(\lambda_4\zeta) + F_5\cosh(\lambda_3\zeta) + F_6\sinh(\lambda_3\zeta), \tag{2.59}$$

where $\lambda_4^2$ is equal to $-\lambda_2^2$ in the second case. $C_i$, $D_i$, $E_i$ and $F_i$'s are arbitrary constants. Desired boundary conditions can be applied to the general solution in order to obtain the characteristic equation. Shear force, bending moment and higher order moment terms are used to obtain the boundary conditions. In higher order beam theory, there are three constraints for each end. In total, there are six equations and six unknowns. On the contrary, in Timoshenko beam model, two boundary conditions for each end are enough as the order of differential equation is four. Characteristic equations for different sets of boundary conditions and related mode shapes are given in [15]. Characteristic equations considering free-free end conditioned beam is given below.

For the case $\bar{\varpi} < \eta_B$

$$\begin{gathered}\frac{P_2P_3}{\lambda_2{}^2\lambda_3{}^2}\sin(\lambda_1)(1-\cosh(\lambda_2)\cosh(\lambda_3))-\frac{P_1P_3}{\lambda_1{}^2\lambda_3{}^2}\sinh(\lambda_2)(1-\cosh(\lambda_1)\cosh(\lambda_3)) \\ +\frac{P_1P_2}{\lambda_1{}^2\lambda_2{}^2}\sinh(\lambda_3)(1-\cos(\lambda_1)\cosh(\lambda_2))+\frac{1}{2}\left(-\frac{P_1^2}{\lambda_1{}^4}+\frac{P_2^2}{\lambda_2{}^4}+\frac{P_3{}^2}{\lambda_3{}^4}\right)\sin(\lambda_1)\sinh(\lambda_2)\sinh(\lambda_3)=0\end{gathered} \tag{2.60}$$

where

$$\begin{aligned}P_1&=\lambda_1(\lambda_2{}^2-\lambda_3{}^2)(h^2\bar{\varpi}^2-12\lambda_1{}^2)(h^2\bar{\varpi}^2+12\lambda_2{}^2+12\lambda_3{}^2),\\ P_2&=\lambda_2(\lambda_1{}^2+\lambda_3{}^2)(h^2\bar{\varpi}^2+12\lambda_2{}^2)(h^2\bar{\varpi}^2-12\lambda_1{}^2+12\lambda_3{}^2),\\ P_3&=\lambda_3(\lambda_1{}^2+\lambda_2{}^2)(h^2\bar{\varpi}^2+12\lambda_3{}^2)(h^2\bar{\varpi}^2-12\lambda_1{}^2+12\lambda_2{}^2).\end{aligned} \tag{2.61}$$

For the case $\bar{\varpi} > \eta_B$

$$\begin{gathered}\frac{S_2S_3}{\lambda_4{}^2\lambda_3{}^2}\sin(\lambda_1)(1-\cosh(\lambda_4)\cosh(\lambda_3))-\frac{S_1S_3}{\lambda_1{}^2\lambda_3{}^2}\sin(\lambda_4)(1-\cos(\lambda_1)\cosh(\lambda_3)) \\ -\frac{S_1S_2}{\lambda_1{}^2\lambda_4{}^2}\sinh(\lambda_3)(1-\cos(\lambda_1)\cos(\lambda_4)) \\ +\frac{1}{2}\left(\frac{S_1{}^2}{\lambda_1{}^4}+\frac{S_2{}^2}{\lambda_4{}^4}-\frac{S_3{}^2}{\lambda_3{}^4}\right)\sin(\lambda_1)\sin(\lambda_4)\sinh(\lambda_3)=0\end{gathered} \tag{2.62}$$

where

$$\begin{aligned}S_1&=\lambda_1(\lambda_4{}^2+\lambda_3{}^2)(h^2\bar{\varpi}^2-12\lambda_1{}^2)(h^2\bar{\varpi}^2-12\lambda_4{}^2+12\lambda_3{}^2),\\ S_2&=\lambda_4(\lambda_1{}^2+\lambda_3{}^2)(h^2\bar{\varpi}^2-12\lambda_4{}^2)(h^2\bar{\varpi}^2-12\lambda_1{}^2+12\lambda_3{}^2),\\ S_3&=\lambda_3(\lambda_1{}^2-\lambda_4{}^2)(h^2\bar{\varpi}^2+12\lambda_3{}^2)(h^2\bar{\varpi}^2-12\lambda_1{}^2-12\lambda_4{}^2).\end{aligned} \tag{2.63}$$

## 2.2 Spindle-Holder-Tool Modeling

The aim of constructing spindle-holder-tool assembly is to obtain tool point FRF of the assembly. Effect of each component should be included in the tool point FRF. Firstly, main shaft of spindle which is composed of several beams which are rigidly attached to each other is constructed. Then bearings are added on to the main shaft. In order to simulate the bearings, connected spindle shaft at various locations, spring and damper elements are used in the model. There is also holder and tool in front of the main shaft. Both the holder and the tool are as well composed of several beams. Similarly, beams are rigidly connected to each other in order to form holder and tool. Holder and tool are attached to each other using elastic connection and there is also elastic connection between holder and spindle assembly. Details of the coupling methods are explained in the following sections.

### 2.2.1 Rigid Beam Coupling

Having obtained receptances of each beam element with sufficient number of modes, beams are coupled to each other in order to obtain the combined receptance information. After the coupling operation, receptance data of the connection points is lost and only the end point FRF information is acquired. Figure 2.3 shows connection points before and after coupling operation. It should be noted that, in the receptance coupling of the beam elements, only inverse of 2x2 matrices is needed.

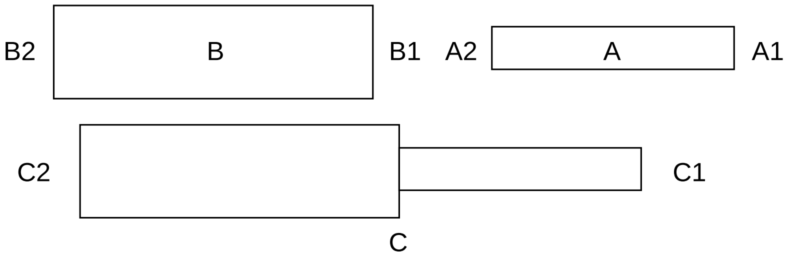

Figure 2.3 Coupling Operation

Receptance matrices of beam A and B can be written as follows

$$[A]=\begin{bmatrix}[A_{11}] & [A_{12}]\\ [A_{21}] & [A_{22}]\end{bmatrix},\quad [B]=\begin{bmatrix}[B_{11}] & [B_{12}]\\ [B_{21}] & [B_{22}]\end{bmatrix}. \tag{2.64}$$

$[A_{11}]$ is given as an example below,

$$[A_{11}]=\begin{bmatrix}H_{A1A1} & L_{A1A1}\\ N_{A1A1} & P_{A1A1}\end{bmatrix}. \tag{2.65}$$

Remaining submatrices of $[A]$ and $[B]$ can be obtained similarly. End points of the new coupled structure are represented by points $C_1$ and $C_2$. After writing proper displacement and force relations at connection point for which details are given in [25], receptance matrix of the new structure, $C$ can be given as follows

$$[C]=\begin{bmatrix}[C_{11}] & [C_{12}]\\ [C_{21}] & [C_{22}]\end{bmatrix}, \tag{2.66}$$

where

$$\begin{aligned}
[C_{11}]&=[A_{11}]-[A_{12}]\big[[A_{22}]+[B_{11}]\big]^{-1}[A_{21}],\\
[C_{12}]&=[A_{12}]\big[[A_{22}]+[B_{11}]\big]^{-1}[B_{12}],\\
[C_{21}]&=[B_{21}]\big[[A_{22}]+[B_{11}]\big]^{-1}[B_{21}],\\
[C_{22}]&=[B_{22}]-[B_{21}]\big[[A_{22}]+[B_{11}]\big]^{-1}[B_{12}].
\end{aligned} \tag{2.67}$$

Alternatively, impedance coupling method can also be applied. Drawback of impedance coupling is that it requires inverse of higher order matrices. It requires more time with respect to receptance coupling method. In impedance coupling method, inverse of $[A]$ and $[B]$ matrices are obtained and then two matrices are added together. Inverses of $[A]$ and $[B]$ matrices are given below,

$$[z_A]=\begin{bmatrix}
z_{A1A1}^{H} & z_{A1A1}^{L} & z_{A1A2}^{H} & z_{A1A2}^{L}\\
z_{A1A1}^{N} & z_{A1A1}^{P} & z_{A1A2}^{N} & z_{A1A2}^{P}\\
z_{A2A1}^{H} & z_{A2A1}^{L} & z_{A2A2}^{H} & z_{A2A2}^{L}\\
z_{A2A1}^{N} & z_{A2A1}^{P} & z_{A2A2}^{N} & z_{A2A2}^{P}
\end{bmatrix} \tag{2.68}$$

$$\left[z_B\right]=\begin{bmatrix} z_{B1B1}^{H} & z_{B1B1}^{L} & z_{B1B2}^{H} & z_{B1B2}^{L} \\ z_{B1B1}^{N} & z_{B1B1}^{P} & z_{B1B2}^{N} & z_{B1B2}^{P} \\ z_{B2B1}^{H} & z_{B2B1}^{L} & z_{B2B2}^{H} & z_{B2B2}^{L} \\ z_{B2B1}^{N} & z_{B2B1}^{P} & z_{B2B2}^{N} & z_{B2B2}^{P} \end{bmatrix} \tag{2.69}$$

Adding operation is applied to only common nodes.

$$\left[z_C\right]=\left[z_A\right]\oplus\left[z_B\right] \tag{2.70}$$

$$\left[z_C\right]=\begin{bmatrix} z_{A1A1}^{H} & z_{A1A1}^{L} & z_{A1A2}^{H} & z_{A1A2}^{L} & 0 & 0 \\ z_{A1A1}^{N} & z_{A1A1}^{P} & z_{A1A2}^{N} & z_{A1A2}^{P} & 0 & 0 \\ z_{A2A1}^{H} & z_{A2A1}^{L} & z_{A2A2}^{H}+z_{B1B1}^{H} & z_{A2A2}^{L}+z_{B1B1}^{L} & z_{B1B2}^{H} & z_{B1B2}^{L} \\ z_{A2A1}^{N} & z_{A2A1}^{P} & z_{A2A2}^{N}+z_{B1B1}^{N} & z_{A2A2}^{P}+z_{B1B1}^{P} & z_{B1B2}^{N} & z_{B1B2}^{P} \\ 0 & 0 & z_{B2B1}^{H} & z_{B2B1}^{L} & z_{B2B2}^{H} & z_{B2B2}^{L} \\ 0 & 0 & z_{B2B1}^{N} & z_{B2B1}^{P} & z_{B2B2}^{N} & z_{B2B2}^{P} \end{bmatrix} \tag{2.71}$$

Eq. (2.71) explains logic of impedance coupling. Only impedances of $z_{A2A2}$ and $z_{B1B1}$ points are added because point A2 is common with point B1. Matrix size is also increased to 6x6 since there are unshared nodes in the matrix. Then, inverse of $\left[z_C\right]$ matrix is taken to get the final receptance $\left[C\right]$ matrix. Receptance matrix $\left[C\right]$ is given below,

$$\left[C\right]=\begin{bmatrix} H_{C1C1} & L_{C1C1} & H_{C1com} & L_{C1com} & H_{C1C2} & L_{C1C2} \\ N_{C1C1} & P_{C1C1} & N_{C1com} & P_{C1com} & N_{C1C2} & P_{C1C2} \\ H_{comC1} & L_{comC1} & H_{comcom} & L_{comcom} & H_{comC2} & L_{comC2} \\ N_{comC1} & P_{comC1} & N_{comcom} & P_{comcom} & N_{comC2} & P_{comC2} \\ H_{C2C1} & L_{C2C1} & H_{C2com} & L_{C2com} & H_{C2C2} & L_{C2C2} \\ N_{C2C1} & P_{C2C1} & N_{C2com} & P_{C2com} & N_{C2C2} & P_{C2C2} \end{bmatrix} \tag{2.72}$$

where $"com"$ refers to connection point of beams. It is seen that impedance coupling process stores receptance of the connection point. If it is not required, common point receptances can be deleted and matrix size could be reduced to 4x4.

In order to construct different cross sectioned continuous beams, both techniques can be performed iteratively. Although both methods can be implemented, the first method is preferred in the calculations as it is faster.

### 2.2.2 Structural Modification Method

In order to support the spindle, bearings are used at different locations. Effect of bearings are included into the model as spring and damper elements by using Özgüven`s structural modification method [18]. Figure 2.4 shows structural modification method schema for adding bearings. After adding bearing to point $C_2$, rigid beam coupling operation is proceeded from point $C_2'$ in order to construct remaining parts of spindle shaft.

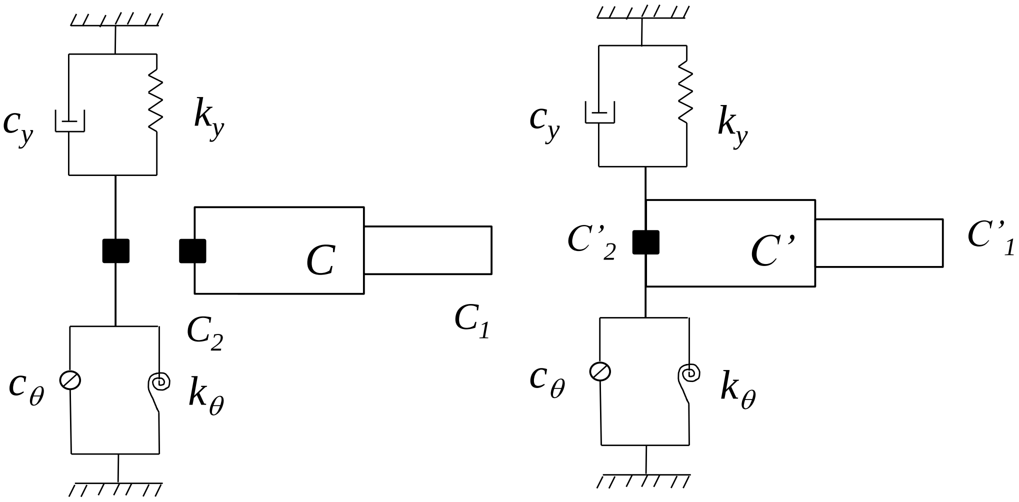

Figure 2.4 Connection of Bearing Using Structural Modification

Including the effects of bearings, the receptance of the structure can be written as follows

$$[\alpha_{c'}] = \left[[I] + [\alpha_c][D]\right]^{-1}[\alpha_c], \tag{2.73}$$

$$[\alpha_c] = \begin{bmatrix} H_{C1C1} & L_{C1C1} & H_{C1C2} & L_{C1C2} \\ N_{C1C1} & P_{C1C1} & N_{C1C2} & P_{C1C2} \\ H_{C2C1} & L_{C2C1} & H_{C2C2} & L_{C2C2} \\ N_{C2C1} & P_{C2C1} & N_{C2C2} & P_{C2C2} \end{bmatrix}, \tag{2.74}$$

In Eq. (2.73) effect of bearing is included in $[D]$ matrix and $[I]$ is unit matrix. If bearing is located at $C_2$ in Figure 2.4, dynamic stiffness matrix of bearing can be written as follows,

$$[D] = \begin{bmatrix} 0 & 0 & 0 & 0 \\ 0 & 0 & 0 & 0 \\ 0 & 0 & k_y + i\omega c_y & 0 \\ 0 & 0 & 0 & k_\theta + i\omega c_\theta \end{bmatrix}. \tag{2.75}$$

Where $(k_y, c_y)$ and $(k_\theta, c_\theta)$ are translational and rotational stiffness and damping coefficients of the bearings, respectively. Computational effort in the calculation of Eq. (2.73) can be decreased by reordering matrices such that the connection degrees of freedoms are grouped at the upper left corner. The reordered dynamic stiffness matrix can be written in the following form,

$$[D] = \begin{bmatrix} [D_{11}] & 0 \\ 0 & 0 \end{bmatrix}, \quad [D_{11}] = \begin{bmatrix} k_y + i\omega c_y & 0 \\ 0 & k_\theta + i\omega c_\theta \end{bmatrix}. \tag{2.76}$$

In addition to this, $[\alpha_c]$ is rearranged in the same manner. Reordering these matrices as described above, size of the inverted matrix decreases from 4x4 to 2x2. Therefore, the receptance matrix of the coupled system including the bearings can obtained as follows

$$\begin{aligned}&\left[\alpha_{c'}^{11}\right]=\left[[I]+\left[\alpha_{c}^{11}\right]\left[D^{11}\right]\right]^{-1}\left[\alpha_{c}^{11}\right],\\&\left[\alpha_{c'}^{12}\right]^{T}=\left[\alpha_{c'}^{21}\right]=\left[\alpha_{c}^{21}\right]\left[[I]-\left[D^{11}\right]\left[\alpha_{c'}^{11}\right]\right],\\&\left[\alpha_{c'}^{22}\right]=\left[\alpha_{c}^{22}\right]-\left[\alpha_{c}^{21}\right]\left[D^{11}\right]\left[\alpha_{c'}^{12}\right].\end{aligned} \tag{2.77}$$

The receptances obtained by Eq. (2.77) should be reordered back to the original form in order to get similar submatrices as before. Instead of structural modification method, impedance coupling method can also be used as explained before. Firstly, inverse of Eq. (2.74) is taken and Eq. (2.75) is added to proper nodes of Eq. (2.74). Then, inverse of newly composed matrix gives coupled receptance of the system. In the calculations first method is preferred concerning time efficiency.

### 2.2.3 Elastically Coupling of Beams

Up to here spindle beams are rigidly connected to each other and bearings are added using structural modification method. Yet, if holder and tool are rigidly connected to the spindle, real operating conditions are not represented because relative movement is observed between spindle-holder and holder-tool subassemblies. Therefore, for the coupling of these elements, flexible receptance coupling is needed on the contrary to the rigid beam coupling. Elastic elements are placed in between required parts shown in Figure 2.5.

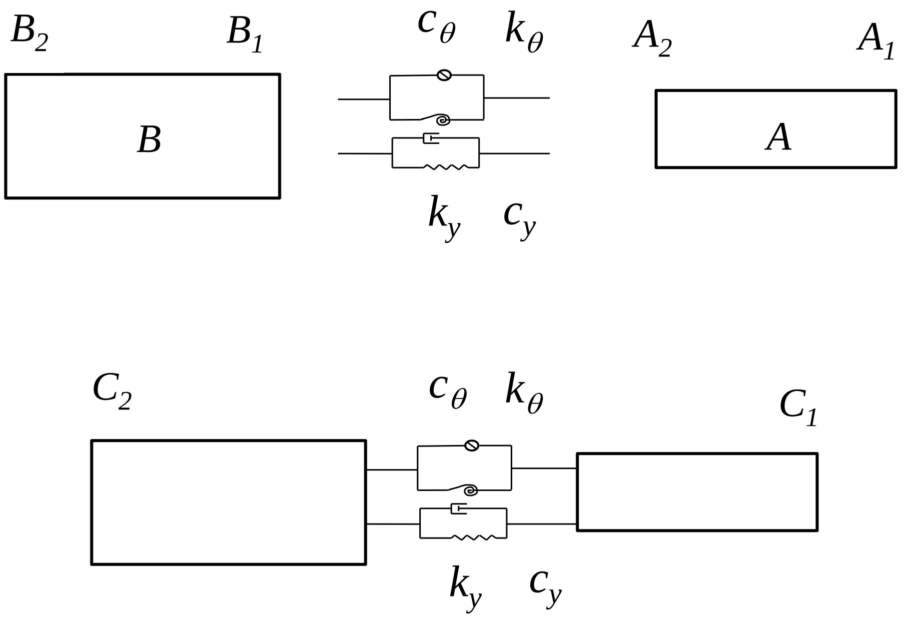

Figure 2.5 Elastic Beam Coupling

Formulation of flexible receptance coupling includes spring and damper elements between two beam segments (A and B). The coupling stiffness matrix can be written in the following form

$$\left[K_{AB}\right]=\begin{bmatrix}k_{y}^{AB}+i\omega c_{y}^{AB} & 0\\ 0 & k_{\theta}^{AB}+i\omega c_{\theta}^{AB}\end{bmatrix}, \tag{2.78}$$

where $k_y^{AB}$ and $k_\theta^{AB}$ are translational and rotational stiffnesses, and, $c_y^{AB}$ and $c_\theta^{AB}$ are translational and rotational damping coefficients of the flexible connection. In flexible receptance coupling, force and displacement relations are written at the connection point where stiffness and damping elements are as well included in equations. The resulting equations for the receptance are given as follows,

$$\begin{aligned}
[C_{11}] &= [A_{11}] - [A_{12}]\left[[A_{22}] + [K_{AB}]^{-1} + [B_{11}]\right]^{-1}[A_{21}], \\
[C_{12}] &= [A_{12}]\left[[A_{22}] + [K_{AB}]^{-1} + [B_{11}]\right]^{-1}[B_{12}], \\
[C_{21}] &= [B_{21}]\left[[A_{22}] + [K_{AB}]^{-1} + [B_{11}]\right]^{-1}[B_{21}], \\
[C_{22}] &= [B_{22}] - [B_{21}]\left[[A_{22}] + [K_{AB}]^{-1} + [B_{11}]\right]^{-1}[B_{12}].
\end{aligned} \tag{2.79}$$

It is noticed that resulting equations are very similar to Eq. (2.67). Only difference between them is that $[K_{AB}]^{-1}$ terms added into the summation of $[A_{22}]+[B_{11}]$ in Eq. (2.67). If $[K_{AB}]$ term goes to infinity eventually rigid coupling equations are obtained because $[K_{AB}]^{-1}$ goes to zero.

The other alternative way is to use impedance coupling method for elastic coupling. As explained before, impedances of $[A]$ and $[B]$ are obtained by taking inverses of each matrices. Later, three stiffness matrices are added together as shown below.

$$[z_C] = [z_A] \oplus [z_B] \oplus [K_{AB}]. \tag{2.80}$$

### 2.3 Approximate Methods for Spindle Holder Tool Assembly

In Section 2.1, analytical solution for spinning Timoshenko beam and HOBM is obtained. After getting the analytical solution, natural frequency and mode shape information are utilized to obtain repectance of a single beam. In order to perform accurate coupling operation, huge amount of natural frequency and mode shape data should be stored in the memory for each beam. As the slenderness ratio of beam gets smaller and smaller, natural frequencies of the beam increases to very large numbers. Then characteristic equation of the beam should be searched up to very high frequencies. Frequencies which satisfy characteristic equation are stored as the natural frequencies and they are obtained by iteratively increasing frequency. As a result solution time for natural frequencies increases dramatically as huge number of iterations are required for the low slenderness ratio beam. In the spindle assembly, several low slenderness ratio-beams must be coupled together. Coupling operations are repeated for each frequency step increment; as a result, all these operations require high amount of mathematical operations. In order to reduce the calculation time, approximate methods is to be utilized in the modeling.

Firstly, Rayleigh's Quotient Method is used to estimate the lowest eigenvalue. Estimation result is highly dependent on the chosen trial function. Estimated eigenvalue is larger than the lowest eigenvalue, unless the chosen trial function is equal to the exact eigenfunction. Rayleigh-Ritz method estimates not only the lowest frequency but also the desired number of lowest frequencies. Any number of trial functions could be used in Rayleigh-Ritz method. Again all natural frequencies obtained are larger than the exact natural frequencies unless exact eigenfunctions are used. Meirovitch [29] explains Rayleigh-Ritz method for an Euler beam. Mode shapes are obtained as follows,

$$Y(x) = \sum_{i=1}^{n} a_i \phi_i(x), \tag{2.81}$$

where $a_i$'s are undetermined coefficients and $\phi_i$'s are the trial functions. According to Rayleigh's quotient, lowest eigenvalue is the ratio of the maximum potential energy to the reference kinetic energy as shown below,

$$\lambda = \frac{V_{\max}}{T_{ref}}, \tag{2.82}$$

where

$$V_{\max} = \frac{1}{2}\sum_{i=1}^{n}\sum_{j=1}^{n} k_{ij} a_i a_j, \tag{2.83}$$

$$T_{ref} = \frac{1}{2}\sum_{i=1}^{n}\sum_{j=1}^{n} m_{ij} a_i a_j, \tag{2.84}$$

$k_{ij}$ and $m_{ij}$ are stiffness and mass coefficient matrices for the given system. Finally eigenvalues are obtained by Eq. (2.82). Kinetic and potential energy for Timoshenko beam are given by Zhou [30] as follows

$$\begin{aligned} U &= \frac{1}{2}\int_0^L \left\{ EI\left[\frac{\partial \psi(x,t)}{\partial x}\right]^2 + \kappa GA\left[\psi(x,t) - \frac{\partial u(x,t)}{\partial x}\right]^2 \right\} dx, \\ T &= \frac{1}{2}\int_0^L \left\{ \rho A\left[\frac{\partial u(x,t)}{\partial t}\right]^2 + \rho I\left[\frac{\partial \psi(x,t)}{\partial t}\right]^2 \right\} dx. \end{aligned} \tag{2.85}$$

In Eq. (2.85) transverse deflection and rotation angle can be denoted as follows;

$$u(x,t) = U(x)e^{i\omega t}, \quad \psi(x,t) = \Psi(x)e^{i\omega t}. \tag{2.86}$$

Lagrangian function can be written,

$$\begin{aligned} L = U_{\max} - T_{\max} &= \frac{1}{2}\int_0^l \left\{ EI\left[\frac{d\Psi(x)}{dx}\right]^2 + \kappa GA\left[\Psi(x) - \frac{dU(x)}{dx}\right]^2 \right\} dx \\ &- \frac{1}{2}\omega^2 \int_0^l \left[\rho A U^2(x) + \rho I \Psi^2(x)\right] dx \end{aligned} \tag{2.87}$$

If Timoshenko beam theory is considered, Eq. (2.81) is not sufficient because there are two uncoupled differential equations which are transverse deflection and rotation angle. Two sets of trial functions are described as below,

$$U(x) = \sum_{i=1}^{N} a_i U_i(x), \tag{2.88}$$

$$\Psi(x) = \sum_{i=1}^{N} b_i \Psi_i(x), \tag{2.89}$$

where $a_i$ and $b_j$ unknown coefficients and $U_i(x)$ and $\Psi_j(x)$ are trial functions. If Rayleigh-Ritz method ($\partial L / \partial a_n = 0$ and $\partial L / \partial b_n = 0$) is applied to Eq. (2.87) the following eigenvalue problem is obtained

$$\begin{bmatrix} [K_{n\bar{n}}] & [K_{n\bar{m}}] \\ [K_{m\bar{n}}] & [K_{m\bar{m}}] \end{bmatrix} \begin{bmatrix} \{A\} \\ \{B\} \end{bmatrix} - \omega^2 \begin{bmatrix} [M_{n\bar{n}}] & [M_{n\bar{m}}] \\ [M_{m\bar{n}}] & [M_{m\bar{m}}] \end{bmatrix} \begin{bmatrix} \{A\} \\ \{B\} \end{bmatrix} = \begin{Bmatrix} 0 \\ 0 \end{Bmatrix} \tag{2.90}$$

where

$$
\begin{aligned}
&\left[K_{n\bar{n}}\right]=\int_0^1 \kappa GA\frac{dU_n(x)}{dx}\frac{dU_{\bar{n}}(x)}{dx}dx, &&\left[K_{n\bar{m}}\right]=\int_0^1 \kappa GA\frac{dU_n(x)}{dx}\Psi_{\bar{m}}(x)dx,\\
&\left[K_{mn}\right]=\int_0^1 \kappa GA\Psi_m(x)\frac{dU_n(x)}{dx}dx, &&\left[K_{m\bar{m}}\right]=\int_0^1\left[EI\frac{\Psi_m(x)}{dx}\frac{\Psi_{\bar{m}}(x)}{dx}+\kappa GA\Psi_m(x)\Psi_{\bar{m}}(x)\right]dx,\\
&\left[M_{n\bar{n}}\right]=\int_0^1 \rho AU_n(x)U_{\bar{n}}(x)dx, &&\left[M_{n\bar{m}}\right]=\left[M_{m\bar{n}}\right]=0,\\
&\left[M_{mm}\right]=\int_0^1 \rho I\Psi_m(x)\Psi_{\bar{m}}(x)dx,\\
&\{A\}=\left[a_1,a_2....a_N\right], &&\{B\}=\left[b_1,b_2....b_N\right]\\
&m,n,\overline{m},\overline{n}=1,2...,N.
\end{aligned}
\tag{2.91}
$$

Natural frequencies and related coefficients of trial functions can be obtained by solving Eq.(2.90). Mass normalization is applied to the coefficients of trial functions and mass normalization coefficient $m^r$ for the $r^{th}$ mode can be found as follows;

$$
m^r=\left(\begin{Bmatrix}A^r\\B^r\end{Bmatrix}^T\begin{bmatrix}\left[M_{n\bar{n}}\right] & \left[M_{n\bar{m}}\right]\\ \left[M_{m\bar{n}}\right] & \left[M_{m\bar{m}}\right]\end{bmatrix}\begin{Bmatrix}A^r\\B^r\end{Bmatrix}\right)^{-\frac{1}{2}}
\tag{2.92}
$$

Important point is to obtain proper trial functions for desired boundary conditions. Main focus is to find proper trial functions for spindle shaft, holder and tool of the spindle. Instead of partitioned structure, an average diameter shaft is assumed for spindle, holder and tool assemblies in order to obtain simple trial functions, example shown in Figure 2.6.

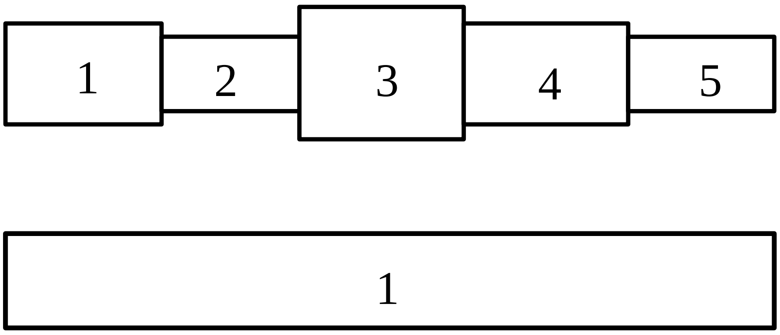

Figure 2.6 Partitioned and Average Diameter Shaft

Then, average diameter shaft is modeled using equations in Section 2.1.1 and related mode shapes are directly used as trial functions in Rayleigh-Ritz solution.

Another method is to use polynomials as a trial function. $x^{r-1}$ type polynomials or orthogonal polynomials such as Legendre, Chebyshev polynomials, can be used for both transverse deflection and bending rotation trial functions. Kocatürk [31] explained Rayleigh Ritz Method with Timoshenko beam model using $x^{r-1}$ type trial functions in the solution. In addition, spring can be added at various locations of the beam in order to simulate bearings by using the following potential energy expression given below,

$$K_i U_n(\zeta) U_{\bar{n}}(\zeta) \tag{2.93}$$

where $K_i$ is the stiffness coefficient. Eq. (2.93) is directly added to the $\left[K_{n\bar{n}}\right]$ value in Eq. (2.91). As a final step, holder and tool assemblies can be added using elastic coupling method to the end of the spindle shaft. Now system is ready for tool point FRF calculations.

## 2.4 FEM of Spindle Holder Tool Assembly

In order to compare results of current work with FEM software, ANSYS 11.0 is employed to construct finite element model of the spindle-holder-tool assembly. In the software BEAM188 element type which is based on Timoshenko Beam Theory is used to model beam elements. It is suitable for moderately thick beam types. BEAM188 includes shear deformation and rotary inertia. Also, this element type has two nodes and each node has six degrees of freedoms. Non-required degrees of freedoms are constrained in order to match both analytical and FEM. Irrelevant modes such as axial and torsional modes are suppressed. COMBIN14 element is used in order to implement spring and damper characteristics in to the assembly. It allows both longitudinal and rotational springs and damper properties. Bearing and flexible connection requirements are fulfilled by COMBIN14 element.

Same geometry and material properties are utilized in both analytical and FEM. In order to include the spinning effect into the FEM, Coriolis effects are enabled and rotational velocity is assigned. In order to observe the effect of spinning on modal analysis results, QR Damped Mode Extraction Method should be employed and complex eigenvectors should be calculated. Also, the same geometry is modelled using 3D solid element. Results of 3D solid element model are presented for only the non-spinning case.

Comparison of ANSYS and analytical results are given in the results and comparison chapter.

# CHAPTER 3

# STABILITY LOBE CONSTRUCTION

Excessive machine tool vibration which is called chatter may cause undesired surface finish on the work piece. During the cutting operation, wavy surface may be left on the work piece because of each tool pass. Generated wavy surface roughness depends on phase shift between each successive cutting. If the cutting frequency is close to chatter frequency, surface finish becomes very rough. Therefore, stability lobe diagram gives useful information about whether there will be chatter or not. As turning is an orthogonal cutting process; nevertheless milling is not, turning and milling stability lobe calculations are different from each other. Milling stability analysis includes time dependent geometry and variables. Derivations for turning and milling stability lobes are given below.

## 3.1 Turning Stability Lobes

In orthogonal cutting, fed direction is assumed perpendicular to the axis of the workpiece. Orthogonal cutting condition is shown in Figure 3.1. Feeding force causes the system to vibrate. Chip thickness changes with respect to vibration frequency of the system.

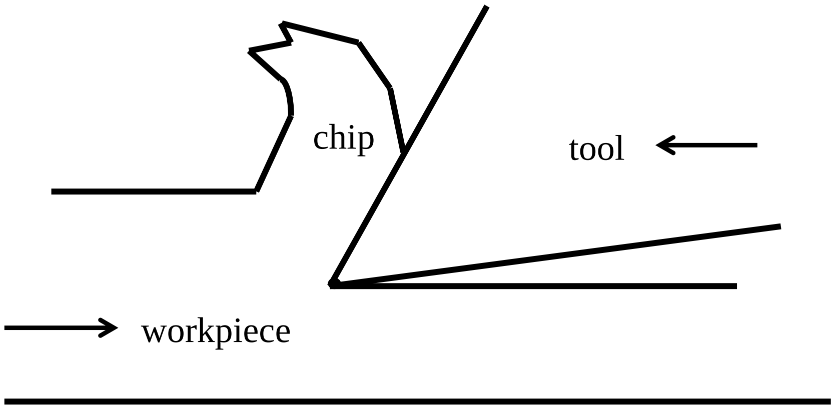

Figure 3.1 Cutting Instance for Orthogonal Cutting

Cutting force is proportional to the cutting area which is written as follows,

$$F(t) = K_f a(x(t-T) - x(t)), \tag{3.1}$$

where $K_f$ is the cutting constant in the feed direction, $a$ is the depth of cut and $x(t-T) - x(t)$ is the dynamic chip thickness produced in one period, which is shown as $T$. Total structure is excited by the cutting force. Therefore force equilibrium can be written considering a one degree of freedom system and feed force as follows,

$$m\ddot{x}+c\dot{x}+kx=F(t). \tag{3.2}$$

Eq. (3.2) can be solved in Laplace domain and after proper operations [4] characteristic equation including real and complex part of FRF is obtained as

$$\left\{1+K_f a_{\lim}\left[G_r(1-\cos(\omega_c T)-G_c\sin(\omega_c T)\right]\right\}+j\left\{K_f a_{\lim}\left[G_r\sin(\omega_c T)+G_c(1-\cos(\omega_c T))\right]\right\}=0, \tag{3.3}$$

where $G_r$ is real and $G_c$ is imaginary part of FRF. $w_c$ is chatter frequency which is very close to the natural frequency of the structure. If the imaginary part of Eq.(3.3) is equated to zero following equations are obtained,

$$\begin{aligned}&G_r\sin(\omega_c T)+G_c(1-\cos(\omega_c T))=0,\\&\tan\beta=\frac{G_c}{G_r}=\frac{\sin(\omega_c T)}{1-\cos(\omega_c T)},\end{aligned} \tag{3.4}$$

where $\beta$ is the phase shift of the FRF of the structure. After some trigonometric manipulations phase shift can be related to the spindle speed $n$ as given below,

$$\begin{aligned}&\omega_c T=\varepsilon+2k\pi,\\&\varepsilon=3\pi+2\beta,\\&\beta=\tan^{-1}\frac{G_c(\omega_c)}{G_r(\omega_c)},\\&n=\frac{60}{T},\end{aligned} \tag{3.5}$$

where $\varepsilon$ is the phase shift between inner and outer modulations, $k$ is the corresponding vibration waves within one period.

Limiting depth of cut in order to avoid chatter is obtained by equating the real part of Eq.(3.3) to zero and for $G_c$ is eliminated by using (3.4). Limiting depth of cut is given below,

$$a_{\lim}=\frac{-1}{2K_f G_r(w_c)}, \tag{3.6}$$

where $G_r(w_c)$ is the real part of transfer function or tool point FRF. Only negative values of $G_r(w_c)$ is employed in Eq. (3.6) in order to have positive depth of cut.

### 3.2 Milling Stability Lobes

The analytical formulation for milling operation is obtained by Budak [32]. In the milling dynamics, two orthogonal degrees of freedom are assumed in the cutting operation as shown in Figure 3.2.

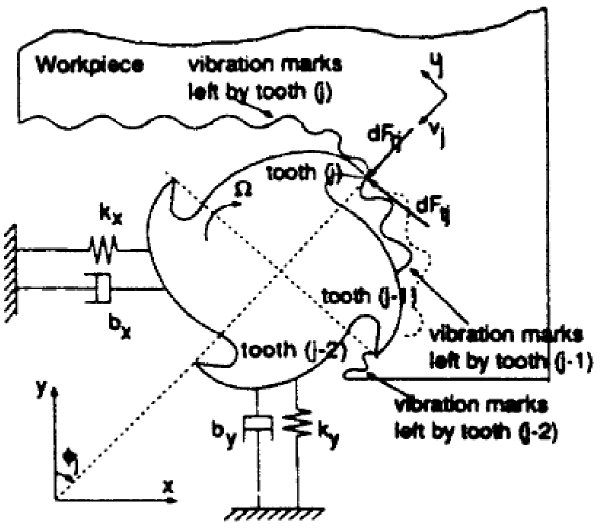

Figure 3.2 Cross Sectional View of an End Mill Showing Differential Forces [32]

Equation of motion for milling is given below as,

$$\{F\}e^{i\omega_c t} = \frac{1}{2}aK_t\begin{bmatrix}\alpha_{xx} & \alpha_{xy}\\ \alpha_{yx} & \alpha_{xx}\end{bmatrix}\left[G(i\omega_c)\right]\{F\}e^{i\omega_c t}, \tag{3.7}$$

where $a$ is axial depth of cut, $K_t$ is cutting force coefficient, $\left[\alpha\right]$ is the matrix of average directional cutting coefficients and $\left[G(i\omega_c)\right]$ is the summation of tool point FRF and work piece FRF matrices identified in the orthogonal cutting directions. For simplicity only tool point FRF matrices is used in this formulations and work piece is assumed as a rigid. $\left[G(i\omega_c)\right]$ and $\left[\alpha\right]$ is given as

$$\left[G(i\omega_c)\right] = \begin{bmatrix}G(i\omega_c)_{xx} & G(i\omega_c)_{xy}\\ G(i\omega_c)_{yx} & G(i\omega_c)_{yy}\end{bmatrix}, \tag{3.8}$$

$$\begin{aligned}
\alpha_{xx} &= \frac{1}{2}\left[\cos 2\phi - 2K_r\phi + K_r \sin 2\phi\right]_{\phi_{st}}^{\phi_{ex}},\\
\alpha_{xy} &= \frac{1}{2}\left[-\sin 2\phi - 2\phi + K_r \cos 2\phi\right]_{\phi_{st}}^{\phi_{ex}},\\
\alpha_{yx} &= \frac{1}{2}\left[-\sin 2\phi + 2\phi + K_r \cos 2\phi\right]_{\phi_{st}}^{\phi_{ex}},\\
\alpha_{xx} &= \frac{1}{2}\left[-\cos 2\phi - 2K_r\phi - K_r \sin 2\phi\right]_{\phi_{st}}^{\phi_{ex}}.
\end{aligned} \tag{3.9}$$

Average directional cutting factors depend on $K_r$, $\phi_{ex}$ and $\phi_{st}$ which are radial cutting constant, entry angle and exit angle, respectively. Entry and exit angles are related to the cutting type (e.g. end milling, down milling and up milling). Eq.(3.7) has a non-trivial solution if

$$\det\left[\left[I\right] + (\Lambda)\left(\left[A_0\right]\left[G(i\omega_c)\right]\right)\right] = 0, \tag{3.10}$$

where

$$\Lambda = -\frac{N_t}{4\pi}aK_t(1 - e^{i\omega_c T}), \qquad [A_0] = \frac{N_t}{2\pi}\begin{bmatrix}\alpha_{xx} & \alpha_{xy}\\ \alpha_{yx} & \alpha_{xx}\end{bmatrix}. \tag{3.11}$$

For orthogonal cutting condition off-diagonal terms $G(i\omega_c)_{yx}$ and $G(i\omega_c)_{xy}$ can be taken as zero. Then, using Eq. (3.10) eigenvalue $\Lambda$ can be found as

$$\Lambda = -\frac{1}{2a_0}\left(a_1 \pm \sqrt{a_1^{\,2} - 4a_0}\right), \tag{3.12}$$

where

$$\begin{aligned} a_0 &= G(i\omega_c)_{xx} G(i\omega_c)_{yy} (\alpha_{xx}\alpha_{yy} - \alpha_{xy}\alpha_{yx}), \\ a_1 &= \alpha_{xx} G(i\omega_c)_{xx} + \alpha_{yy} G(i\omega_c)_{yy}. \end{aligned} \tag{3.13}$$

FRFs at the tool point have complex values; hence, $\Lambda$ is a complex number. Since depth of cut must be a real value, $\Lambda$ is decomposed into real and imaginary components as $\Lambda = \Lambda_R + i\Lambda_I$. After some manipulations, to get only real valued depth of cut, real and imaginary part of $\Lambda$ should have the following proportion

$$\vartheta = \frac{\Lambda_I}{\Lambda_R} = \frac{\sin \omega_c T}{1 - \cos \omega_c T}, \tag{3.14}$$

where $T$ is spindle period and $\omega_c$ is chatter frequency. Eq. (3.14) can be related with the spindle speed $n$ as follows [32],

$$\begin{aligned} \omega_c T &= \varepsilon + 2k\pi, \\ \varepsilon &= \pi - 2\beta, \\ \beta &= \tan^{-1} \vartheta, \\ n &= \frac{60}{N_t T}. \end{aligned} \tag{3.15}$$

$\varepsilon$ is the phase shift between inner and outer modulations, $k$ is the corresponding vibration waves with in period, and $N_t$ is the tooth number. Finally stable limiting depth of cut is found from Eq.(3.11) as,

$$a_{\lim} = -\frac{2\pi\Lambda_R}{N_t K_t}(1 + \vartheta^2). \tag{3.16}$$

Eqs. (3.16) and (3.15) can be utilized to find the related spindle speed for a given depth of cut or limiting depth of cut for a given spindle speed.

# CHAPTER 4

# NUMERICAL RESULTS AND COMPARISON

## 4.1 Spindle Geometry and Related Parameters

The spindle-holder-tool model given by Ertürk [25] is used in this study. Figure 4.1 shows the spindle, holder and tool parts and their final shape. There are ten rigidly coupled beams in the spindle shaft and there are bearings at four points which are shown as black discs in Figure 4.1. Holder has six rigidly coupled beams and tool has only two. Spindle, holder and tool dimensions starting from the right ends, shown in Figure 4.1, are given in the Table 4.1 to 4.3. The first three segments of the spindle subassembly have the same diameter with the last three segments of the holder subassembly. Therefore, the holder subassembly is clamped to the front end of the spindle subassembly by using three common diameter segments. Similarly tool is mounted inside of the first segment of the holder subassembly. Therefore tool is mounted to the holder subassembly such that final length of the overhang tool is 85 mm. As explained before there are flexible connections between the spindle-holder and the holder-tool. They are assumed to exist at the points shown in Figure 4.2.

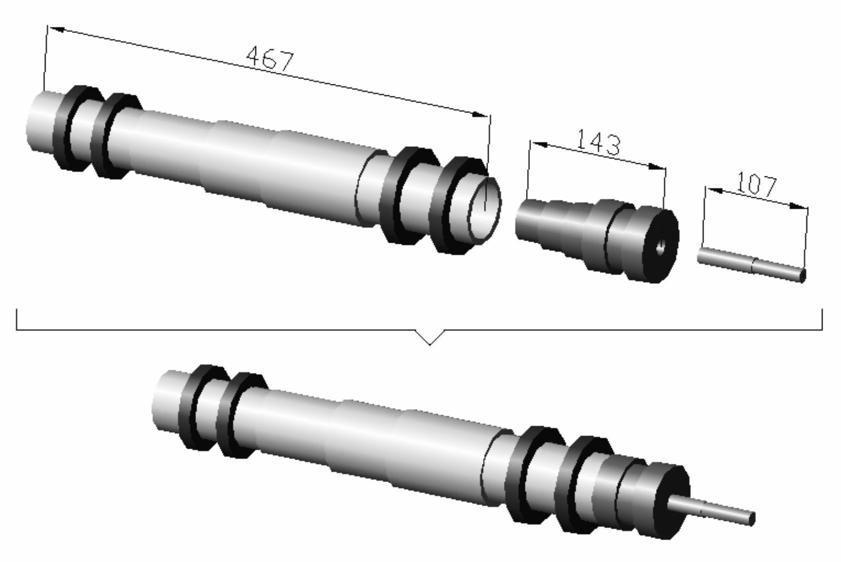

Figure 4.1 Spindle Components and Total Assembly [25]

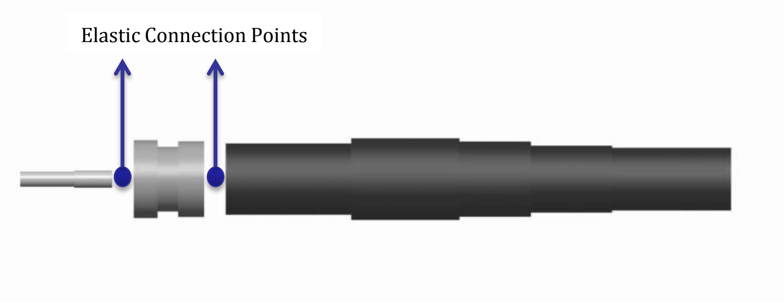

Figure 4.2 Elastic Connection Locations

Table 4.1 Spindle Dimensions [25]

| Segment Number | 1 | 2 | 3 | 4 | 5 | 6 | 7 | 8 | 9 | 10 |
|---|---|---|---|---|---|---|---|---|---|---|
| Length [mm] | 26 | 26 | 26 | 38 | 100 | 66 | 75 | 30 | 40 | 40 |
| Outer Diameter [mm] | 66 | 66 | 66 | 66 | 76 | 70 | 62 | 58 | 58 | 58 |
| Inner Diameter [mm] | 54 | 48 | 40 | 32 | 32 | 32 | 32 | 32 | 32 | 32 |

Table 4.2 Holder Dimensions [25]

| Segment Number | 1 | 2 | 3 | 4 | 5 | 6 |
|---|---|---|---|---|---|---|
| Length [mm] | 22 | 19 | 24 | 26 | 26 | 26 |
| Outer Diameter [mm] | 72 | 60 | 70 | 54 | 48 | 40 |
| Inner Diameter [mm] | 16 | 16 | 16 | 16 | 16 | 16 |

Table 4.3 Tool Dimensions [25]

| Segment Number | 1 | 2 |
|---|---|---|
| Length [mm] | 50 | 57 |
| Outer Diameter [mm] | 14 | 16 |
| Inner Diameter [mm] | 0 | 0 |

Steel is assigned to all materials in the assembly. Very little loss factor (0.002) is assumed in the model in order to get finite peaks in the tool point FRF. Related material properties are given in Table 4.4.

Table 4.4 Material Properties [25]

| $\rho$ (Density) | 7800 kg/m^3 |
|---|---|
| $\nu$ (Poisson Ratio) | 0.3 |
| E (Young's Modulus) | 200 GPa |

For stiffness and damping coefficients, the same values of Arakere [17] are used to simulate the bearings. For elastic connection coefficients the same values given in [16] are used. Table 4.5 gives used bearing and interface properties. Four bearing locations starting from the first segment of the spindle shaft are given in Table 4.6.

Table 4.5 Bearing and Interface Properties [25]

| | Translational Stiffness [N/m] | Rotational Stiffness [N.m/rad] |
|---|---|---|
| Front Bearings (for each) | $7.5 \times 10^5$ | - |
| Rear Bearings (for each) | $2.5 \times 10^6$ | - |
| Spindle Holder Interface | $5 \times 10^7$ | $1.5 \times 10^6$ |
| Holder Tool Interface | $2 \times 10^7$ | $1.5 \times 10^6$ |

Table 4.6 Bearing Locations [25]

| Bearing No | Bearing 1 | Bearing 2 | Bearing 3 | Bearing 4 |
|---|---|---|---|---|
| Distance [mm] | 26 | 78 | 387 | 427 |

### 4.2 Tool Point FRF Results

Before going to the complete assembly results, end point FRF of a single example beam is investigated in order to show effect of spinning clearly. It is expressed before that with respect to spinning speed natural frequencies are separated as forward and backward natural frequencies. In order to examine forward and backward frequencies, a steel cylinder of 1 m length and 0.2 m diameter is studied. First, considering non-spinning case natural frequencies are obtained. Taking the first natural frequency of the non-spinning case as a reference ($\omega_1 = 841.9\, Hz$), spinning speed is increased to $\omega_1$ and $2\omega_1$ respectively. The first three natural frequencies of three different cases are given in Table 4.7. It is observed that at higher modes the difference between the forward and backward frequencies increases. In addition to natural frequencies, end point receptance of the free-free beam is obtained for $\Omega = 0$ and $\Omega = \omega_1$ spin speeds, which are given in Figure 4.3. It is observed, single modes split into two modes having natural frequencies lower and larger than the zero spin case as predicted by the natural frequencies. Moreover, there is an additional mode at a very low frequency (49 Hz) for the case including gyroscopic effects. This frequency is not presented in Table 4.7 for easy comparison.

Table 4.7 Natural Frequencies $0$, $\omega_1$ and $2\omega_1$ Hz

| | | $\Omega = \omega_1$ | | | | $\Omega = 2\omega_1$ | | | |
|---|---|---|---|---|---|---|---|---|---|
| | $\Omega = 0$ | FWD | % Diff. wrt $\Omega = 0$ | BWD | % Diff. wrt $\Omega = 0$ | FWD | % Diff. wrt $\Omega = 0$ | BWD | % Diff. wrt $\Omega = 0$ |
| 1. Mode | 841.9 | 923.9 | 9.7 | 762.7 | 9.4 | 1010.2 | 20.0 | 690.4 | 18.0 |
| 2. Mode | 2032.4 | 2159.6 | 6.3 | 1904.0 | 6.3 | 2286.6 | 12.5 | 1780.3 | 12.4 |
| 3. Mode | 3466.4 | 3615.5 | 4.3 | 3311.9 | 4.5 | 3761.1 | 8.5 | 3159.5 | 8.9 |

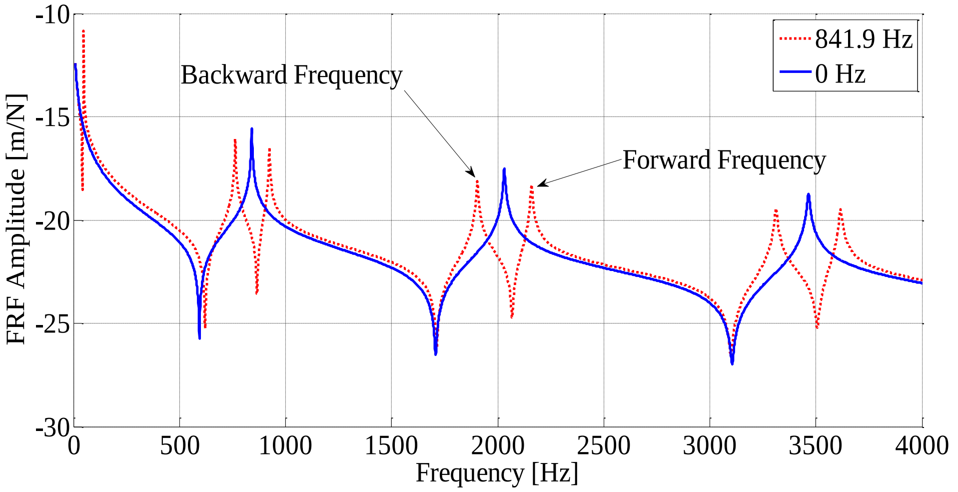

Figure 4.3 Comparison of Forward and Backward Natural Frequencies at 841.9 and 0 Hz

After constructing the total assembly using the coupling method, natural frequencies and tool point FRF of the spindle assembly is obtained. 0.1 Hz frequency increments are applied in FRF calculations; hence, the resolution of the system is 0.1 Hz. Very small loss factor 0.002 is considered in the analysis. The first 100 modes for each component are employed in the tool point FRF calculations in order to reduce truncation errors. In the first case, 0 and 10000 rpm spindle speeds are obtained and the comparison of them is presented in Figure 4.4. It can be seen that results of both FRF's are nearly coincident and difference is not clear. However, if natural frequency points are zoomed in, forward and backward separations can be observed.

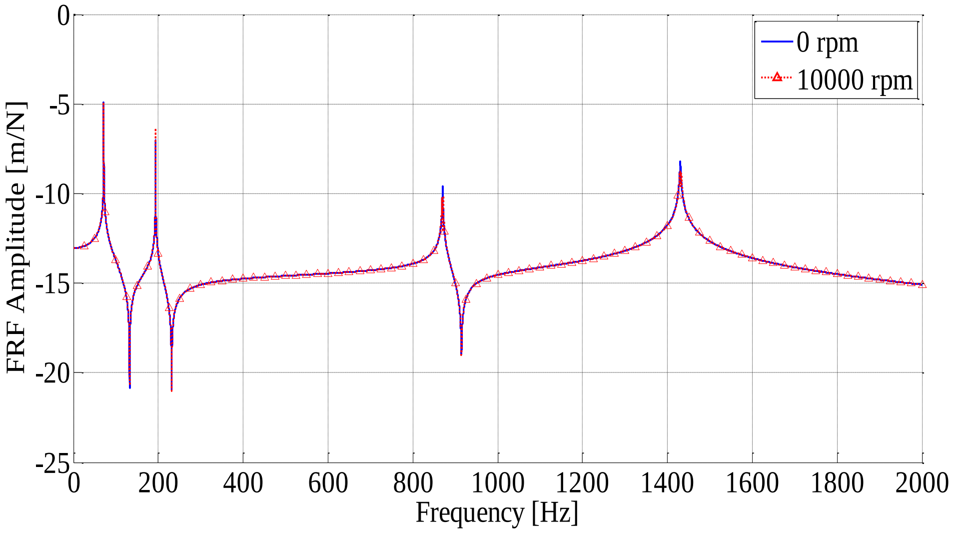

Figure 4.4 Comparison of Tool Point FRF at 0 and 10000 rpm

Forward and backward frequencies are shown in Figure 4.5 to 4.7 for the 3rd, the 4th and the 5th modes. The effect of separation of forward and backward frequencies on the FRF is only dominant around the natural frequencies; whereas, other parts of the FRFs are quite similar to the zero spin speed case.

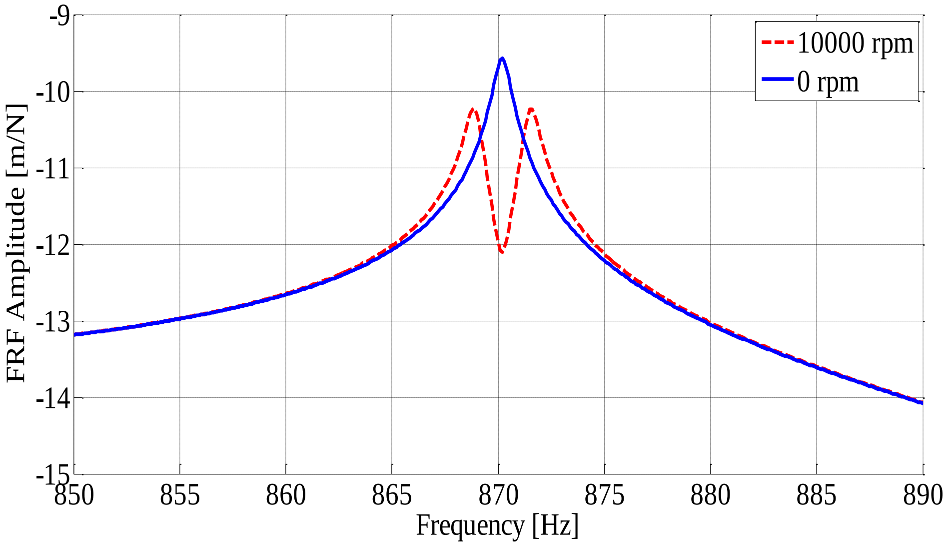

Figure 4.5 Forward and Backward Frequencies around 3rd Mode

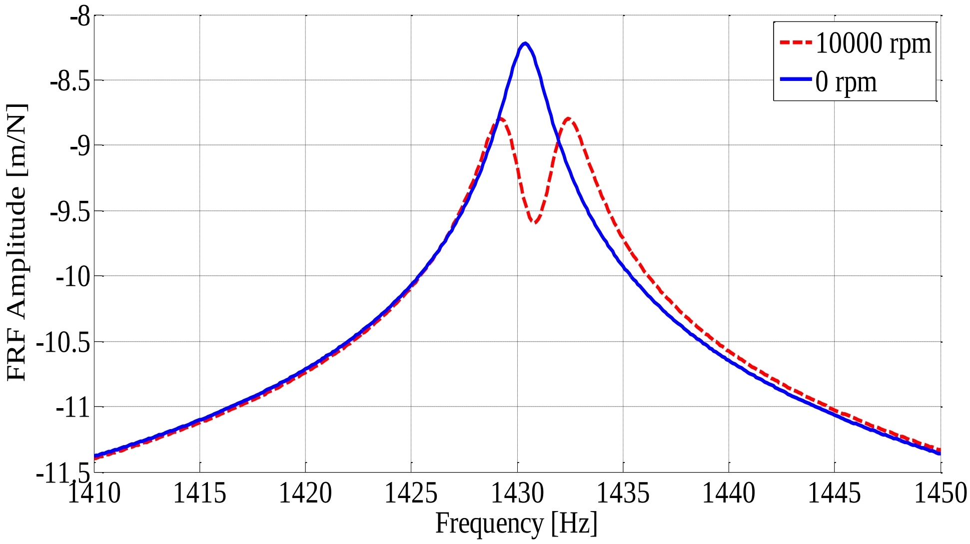

Figure 4.6 Forward and Backward Frequencies around 4th Mode

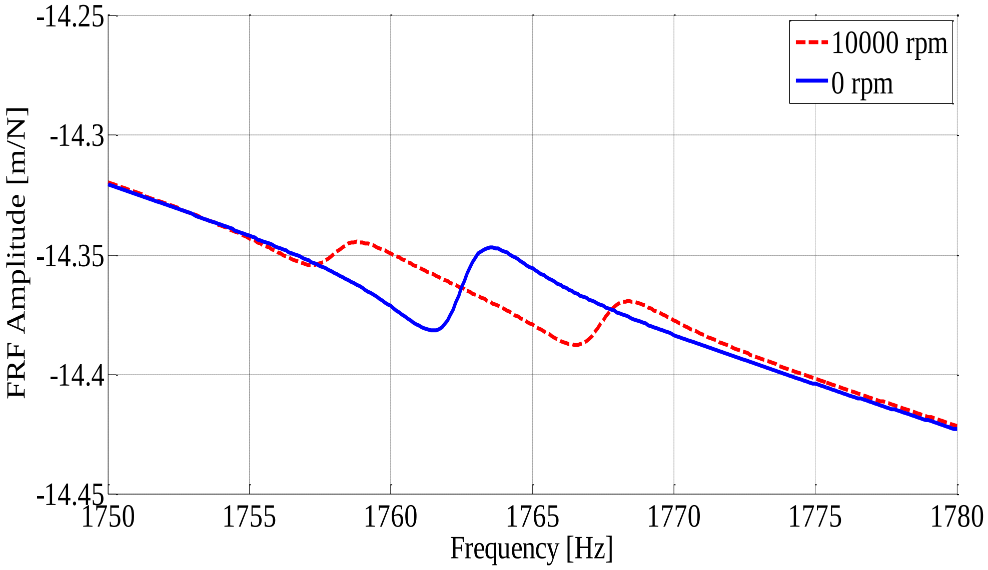

Figure 4.7 Forward and Backward Frequencies around 5th Mode

In Table 4.8 natural frequencies of the system for 0 and 10000 rpm are given. In the coupled model solution, the first two modes do not change, since they correspond to the rigid body modes of the spindle dominated by bearings. However, finite element solution splits them as forward and backward modes as presented in Table 4.9.

Table 4.8 Coupled Model Results for 0 and 10000 rpm Spindle Speed

| 0 rpm | 10000 rpm | |
|---|---|---|
| Natural Frequencies [Hz] | Backward Natural Frequencies [Hz] | Forward Natural Frequencies [Hz] |
| 71.6 | 71.6 | 71.6 |
| 193.8 | 193.8 | 193.8 |
| 870.2 | 868.8 | 871.6 |
| 1430.9 | 1429.2 | 1432.5 |
| 1763.5 | 1758.8 | 1768.4 |
| 3465.5 | 3457.3 | 3474.6 |
| 3648.1 | 3644.1 | 3652.7 |

Table 4.9 ANSYS Results for 0 and 10000 rpm Spindle Speed

| 0 rpm | 10000 rpm | |
|---|---|---|
| Natural Frequencies [Hz] | Backward Natural Frequencies [Hz] | Forward Natural Frequencies [Hz] |
| 71.6 | 71.0 | 72.3 |
| 193.9 | 192.0 | 195.7 |
| 867.5 | 865.2 | 869.7 |
| 1424.0 | 1423.1 | 1424.9 |
| 1752.1 | 1743.5 | 1760.8 |
| 3441.3 | 3414.6 | 3467.0 |
| 3634.3 | 3629.3 | 3639.7 |

If the elastic modes starting with the third mode are considered, analytical solution also splits as backward and forward modes and their comparison with FEM results give a maximum error less than 1%. Good agreement is obtained at elastic modes.

If spindle speed is further increased to 20000 and 30000 rpm, separation between forward and backward frequencies increases slightly in elastic modes whereas the first two natural frequencies are constant as before. Model and ANSYS simulation results at 20000 and 30000 rpm are given in Table 4.10 and Table 4.11. Again, good agreement is obtained at elastic modes for both 20000 and 30000 rpm.

Table 4.10 Forward and Backward Natural Frequencies at 20000 rpm

| 20000 rpm | | 20000 rpm | |
|---|---|---|---|
| Ansys Backward [Hz] | Ansys Forward [Hz] | Model Backward [Hz] | Model Forward [Hz] |
| 70.3 | 72.9 | 71.6 | 71.6 |
| 190.2 | 197.7 | 193.8 | 193.8 |
| 862.9 | 872.0 | 867.6 | 872.8 |
| 1422.2 | 1425.8 | 1428 | 1433.7 |
| 1734.9 | 1769.5 | 1754.2 | 1773.1 |
| 3386.9 | 3491.4 | 3449.1 | 3483.2 |
| 3624.6 | 3645.8 | 3640.5 | 3656.8 |

It is observed that at higher natural frequencies difference between forward and backward frequencies increases; nevertheless, it is not significant. FRF of spinning case is nearly identical to FRF of non-spinning case. Clearly spinning has very limited effect on the tool point FRF of the spindle-holder-tool assembly, in addition spinning effect on the stability lobes will be discussed in the coming sections.

Table 4.11 Forward and Backward Natural Frequencies at 30000 rpm

| 30000 rpm | | 30000 rpm | |
|---|---|---|---|
| Ansys Backward [Hz] | Ansys Forward [Hz] | Model Backward [Hz] | Model Forward [Hz] |
| 69.6 | 73.6 | 71.6 | 71.6 |
| 188.5 | 199.7 | 193.8 | 193.8 |
| 860.7 | 874.2 | 866.3 | 874.1 |
| 1421.3 | 1426.7 | 1426.7 | 1435.1 |
| 1726.4 | 1778.2 | 1749.4 | 1777.8 |
| 3358.4 | 3514.5 | 3440.8 | 3490.2 |
| 3620.2 | 3652.7 | 3636.8 | 3660.8 |

Change in the bearing and connection parameters of the assembly is as well investigated by changing the original stiffness and damping values used in the analysis. In Figure 4.8 both front and rear stiffness values are multiplied and divided by two at 20000 rpm. It is seen from Figure 4.8 that bearing stiffness values mostly effect the first two natural frequencies of the system which are rigid body modes constrained by the bearings. Stiffer bearings shift the first two modes of the system to higher natural frequencies and vice versa. It is observed that higher modes are not significantly affected by bearing parameters.

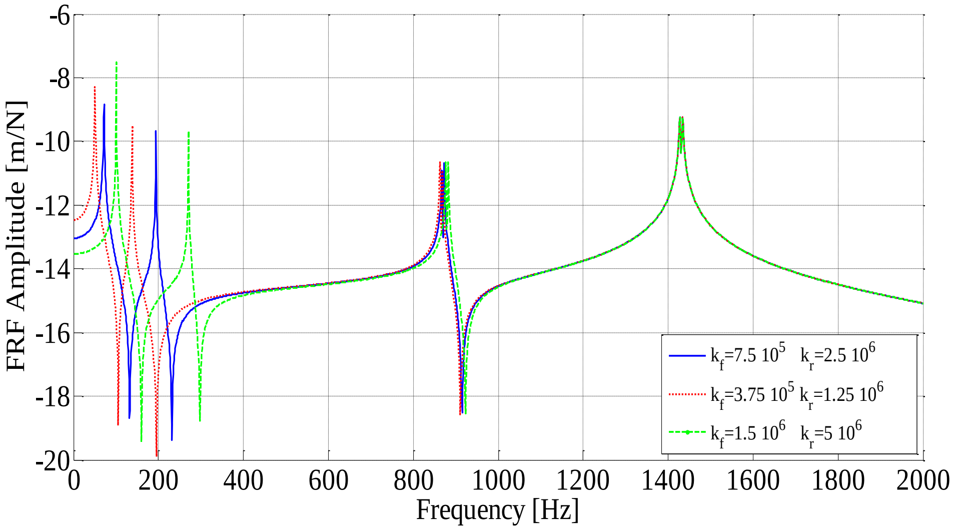

Figure 4.8 Effect of front and rear bearings parameters on the tool point FRF

Another case is to change the contact parameters between spindle-holder and holder-tool subassemblies. Again considering 20000 rpm spin speed, contact values are halved and doubled as in the previous case. It is observed in Figure 4.9 that first two modes are not affected due to the change in the elastic elements; however, higher modes are affected significantly. Increase in the stiffness of the connection parameters resulted in an increase in the natural frequencies of the modes higher or equal to 3. If elastic modes of the spindle assembly are considered, interface connection parameters are more important rather than bearing parameters.

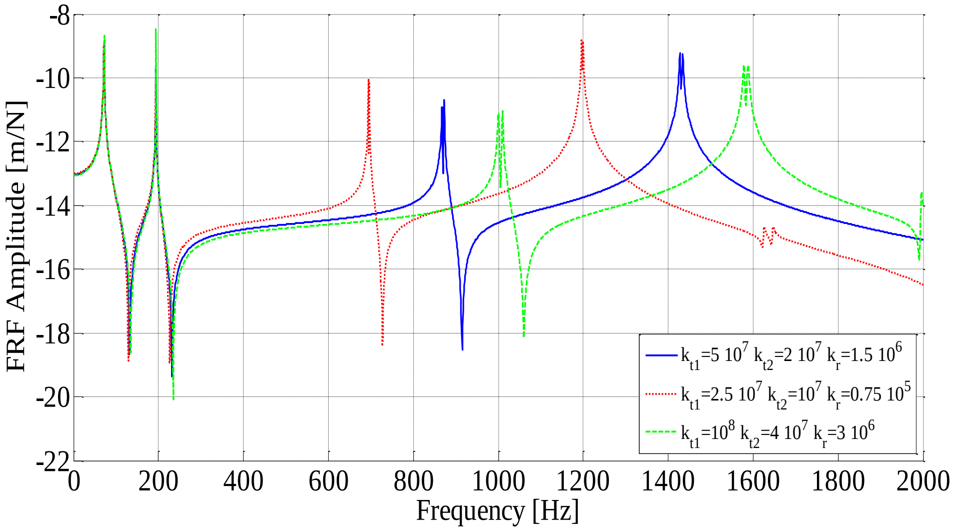

Figure 4.9 Effect of elastic connection elements on the tool point FRF

If micromachining is considered, spindle speeds could reach very high speeds. As an example, 50000 rpm is tried on the existing system and FRF of the tool point is observed with respect to different contact parameters given in Figure 4.10. In addition to the 20000 rpm results separation between forward and backward natural frequencies clearly increases as the connection parameters get stiffer at 50000 rpm. Green line which has the stiffest connection in Figure 4.10 has the biggest difference between forward and backward natural frequencies. This result shows that realistic connection parameter modeling is crucial for the accurate determination of the system dynamics. Yet in order to get more realistic results for micromachining, geometry and related bearing and connection parameters should be updated for specified micro milling machine.

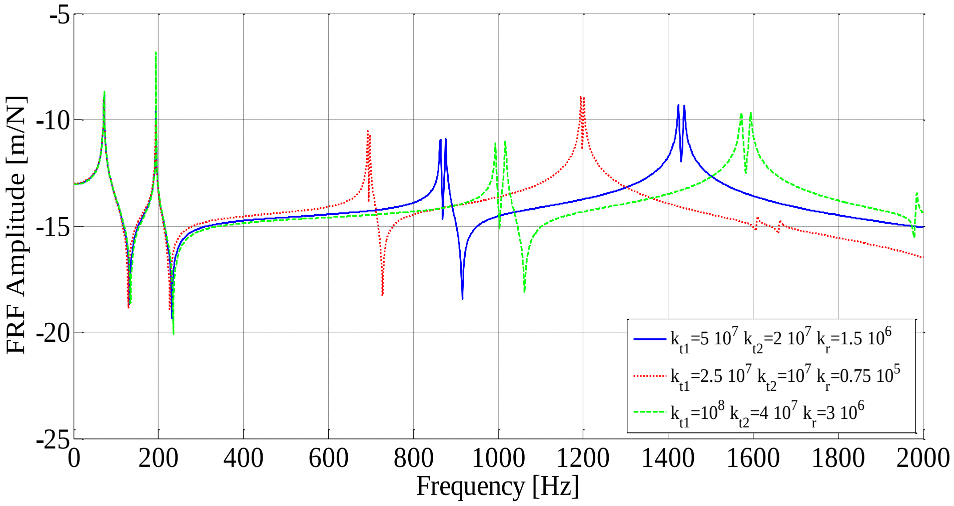

Figure 4.10 Effect of elastic connection elements on the tool point FRF at 50000 rpm

### 4.3 Higher Order Beam Theory Results

Bickford's higher order beam theory is used in modeling as described in Section 2.1.2. HOBM includes shape function coefficient in order to eliminate shear correction factor requirement. Although different shape functions can be employed, $\phi(z) = z\left(1 - \frac{4z^2}{3h^2}\right)$ is taken as a shape function in calculations. In literature, HOBM derivation is obtained considering only rectangular cross sections, thus only solutions of rectangular cross-sections are given in this section. HOBM results are compared with Timoshenko beam results considering different shear correction factors in calculations.

First, free-free beams are considered in calculations. Material properties are taken from Table 4.4. In the first case 1 m length beam with 0.05 m height and 0.1 m width is taken. For rectangular cross-sections width has no effect on natural frequencies as it is cancelled out in equations. Commonly recommended two different shear correction factors ($\kappa = 5/6$ and $\kappa = 14/17$) are used in Timoshenko beam calculations. HOBM and Timoshenko beam results for the first case are given in Table 4.12.

Table 4.12 Natural Frequencies of for 0.05 m Height

| Mode | HOBM [Hz] | Timoshenko $\kappa = 5/6$ [Hz] | Timoshenko $\kappa = 14/17$ [Hz] | % difference | % difference |
|---|---|---|---|---|---|
| 1 | 0 | 0 | 0 | 0 | 0 |
| 2 | 259.0 | 257.9 | 257.9 | 0.4 | 0.4 |
| 3 | 704.5 | 699.4 | 699.2 | 0.7 | 0.8 |
| 4 | 1353.9 | 1340.0 | 1339.6 | 1.0 | 1.1 |
| 5 | 2181.1 | 2152.7 | 2151.6 | 1.3 | 1.4 |
| 6 | 3160.4 | 3111.5 | 3109.1 | 1.5 | 1.6 |
| 7 | 4266.3 | 4191.0 | 4186.7 | 1.8 | 1.9 |
| 8 | 5475.8 | 5368.7 | 5361.9 | 2.0 | 2.1 |
| 9 | 6768.7 | 6625.2 | 6615.3 | 2.1 | 2.3 |
| 10 | 8128.5 | 7944.4 | 7930.6 | 2.3 | 2.4 |

According to Table 4.12, HOBM and Timoshenko results are very close to each other and error is below 2.5 % for the first ten modes. Both shear correction factors give very close results for Timoshenko beam model. In the second case, height of beam is increased to 0.1 m. Results of the second case are given in Table 4.13. It is seen that differences increase as the thickness of the beam is increased. Errors could go up to nearly 5%. However, both shear correction factors give close results with respect to each other. HOBM results are higher than Timoshenko results all the time. It is observed that Timoshenko beam results are more conservative than the HOBM solution.

Table 4.13 Natural Frequencies of for 0.1 m Height

| Mode | HOBM [Hz] | Timoshenko $\kappa = 5/6$ [Hz] | Timoshenko $\kappa = 14/17$ [Hz] | % difference | % difference |
|---|---|---|---|---|---|
| 1 | 0 | 0 | 0 | 0 | 0 |
| 2 | 510.6 | 502.7 | 502.6 | 1.5 | 1.6 |
| 3 | 1339.9 | 1307.6 | 1306.9 | 2.4 | 2.5 |
| 4 | 2458.4 | 2385.2 | 2382.8 | 3.0 | 3.1 |
| 5 | 3765.3 | 3639.5 | 3634.1 | 3.3 | 3.5 |
| 6 | 5190.9 | 5005.5 | 4995.9 | 3.6 | 3.8 |
| 7 | 6688.5 | 6438.4 | 6423.5 | 3.7 | 4.0 |
| 8 | 8287.7 | 7908.6 | 7887.4 | 4.6 | 4.8 |
| 9 | 9788.1 | 9395.3 | 9367.2 | 4.0 | 4.3 |
| 10 | 11352.4 | 10882.9 | 10847.1 | 4.1 | 4.5 |

In the final case study, height is increased to 0.2 m. Results are given at Table 4.14. According to results of Table 4.14, difference between HOBM and Timoshenko beam model increases dramatically after 8. mode. Again both shear correction factor gives close results. It is observed that as the slenderness ratio of the beam becomes smaller and smaller difference between HOBM and Timoshenko beam model increases considerably, vice versa. Timoshenko beam theory is again more conservative than the HOBM. It is also expected that for very high slenderness ratios, HOBM and Timoshenko beam solutions are similar to the Euler beam solutions.

Table 4.14 Natural Frequencies of for 0.2 m Height

| Mode | HOBM [Hz] | Timoshenko $\kappa = 5/6$ [Hz] | Timoshenko $\kappa = 14/17$ [Hz] | % difference | % difference |
|---|---|---|---|---|---|
| 1 | 0 | 0 | 0 | 0 | 0 |
| 2 | 967.3 | 921.2 | 920.7 | 4.8 | 4.8 |
| 3 | 2284.0 | 2153.2 | 2150.0 | 5.7 | 5.9 |
| 4 | 3801.4 | 3581.0 | 3573.1 | 5.8 | 6.0 |
| 5 | 5346.2 | 5041.7 | 5026.9 | 5.7 | 6.0 |
| 6 | 6837.6 | 6472.3 | 6449.6 | 5.3 | 5.7 |
| 7 | 7790.6 | 7642.8 | 7606.8 | 1.9 | 2.4 |
| 8 | 9598.3 | 8553.5 | 8513.0 | 10.9 | 11.3 |
| 9 | 10975.2 | 8672.0 | 8629.3 | 21.0 | 21.4 |
| 10 | 12712.6 | 10050.6 | 10004.3 | 20.9 | 21.3 |

### 4.4 Approximate Method Results

In Rayleigh-Ritz solution, $x^r$ type polynomials are directly used as trial functions. The spindle geometry is constructed step by step in order to investigate the efficiency of Rayleigh-Ritz method for different cases. In Rayleigh-Ritz solution maximum 16 trial functions can be used, on the other hand first 100 natural frequencies and mode shapes are used in the coupled model.

For the first case, spindle shaft given in Table 4.1 is modeled without bearings and natural frequencies of Rayleigh-Ritz solution are compared with the model using receptance coupling. Results of these two different methods are shown in Table 4.15. In Figure 4.11 FRF of the two solutions are given. According to natural frequencies and FRF results, Rayleigh-Ritz and coupled system solutions are very close to each other.

For the next step bearings are added onto the specified locations of the spindle shaft. In Rayleigh-Ritz method, bearings are employed just adding stiffness and damping terms into the related equations of stiffness matrices as explained in previous chapter. Spindle natural frequencies and tip point FRF comparisons are given in Table 4.16 and Figure 4.12. Natural frequencies are very close to each other and also coupled model and Rayleigh-Ritz FRFs match on top of each other very well.

Table 4.15 Spindle Shaft Free-Free Natural Frequencies

| Rayleigh-Ritz [Hz] | Coupled System [Hz] |
|---|---|
| 0 | 0 |
| 1529.1 | 1529.1 |
| 3558.6 | 3563.3 |
| 6036.4 | 6041.5 |
| 8745.9 | 8762.0 |

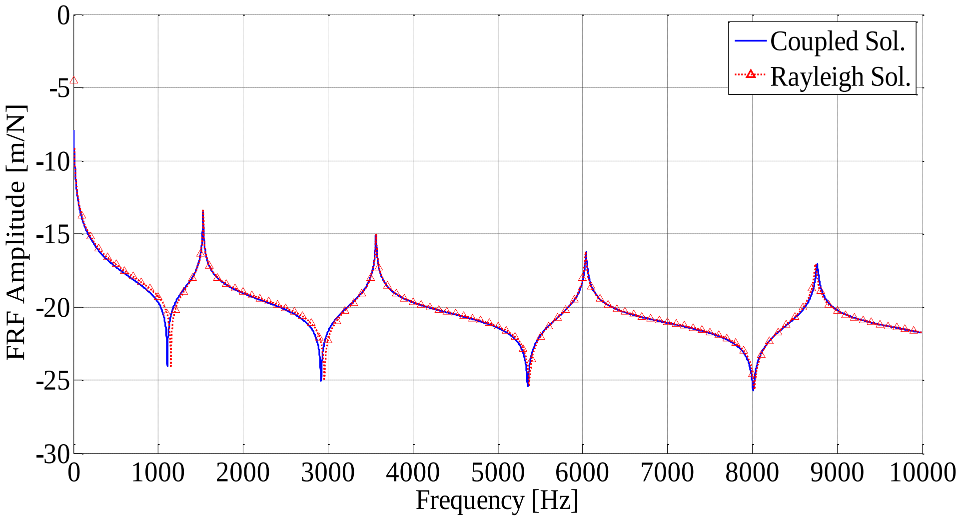

Figure 4.11 Free-Free BC Spindle Tip Point FRF for Rayleigh and Coupled Solution

Table 4.16 Spindle Shaft with Spring Natural Frequencies

| Rayleigh [Hz] | Coupled System [Hz] |
|---|---|
| 91.1 | 91.0 |
| 210.5 | 210.3 |
| 1537.6 | 1536.5 |
| 3568.8 | 3565.4 |
| 6036.6 | 6043.0 |
| 8744.4 | 8765.7 |

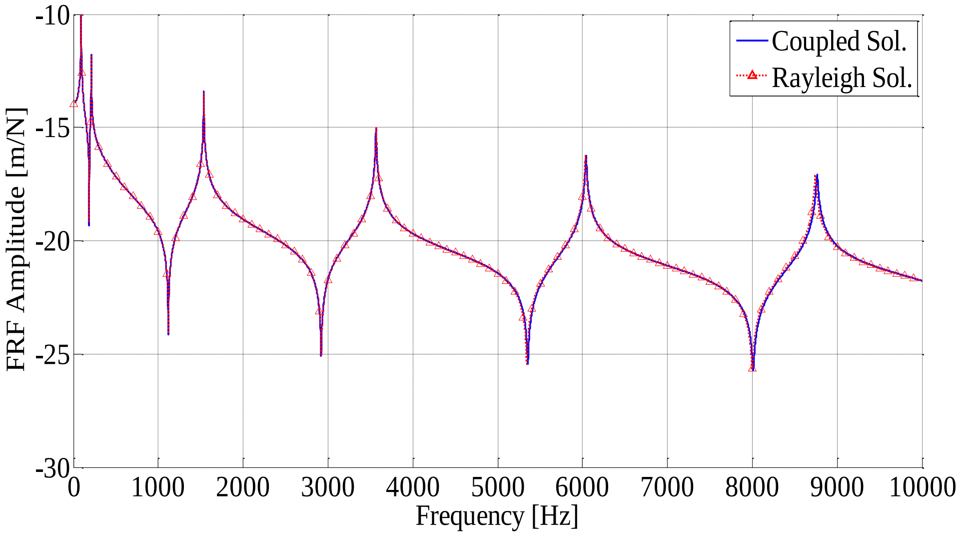

Figure 4.12 Spindle Tip Point FRF for Rayleigh and Coupled Solution with Added Bearings

Natural frequencies obtained by Rayleigh Ritz method must be always larger than the exact frequencies unless the exact eigenfunctions are used in that case they are equal to the exact solutions [29, 34]. However, in results shown in Table 4.15 and Table 4.16 some of the Rayleigh natural frequencies are smaller than the coupled system solution. Main cause of this result is that coupled solution is not an exact solution. It is not possible to include all natural frequencies and mode shapes into the coupling calculations because of the required memory and time for the process. Truncation error is added onto the coupled system solution and it can be said that if Rayleigh-Ritz solution is lower than coupled solution, Rayleigh-Ritz results at this natural frequency is better than coupled solution. The effect of truncation error on the tool point FRF of the system is studied in Figure 4.13. As the number of modes utilized in the coupling decreases towards 25, especially higher modes shift rightward and this explains why some of the coupled natural frequencies are higher than Rayleigh-Ritz solution.

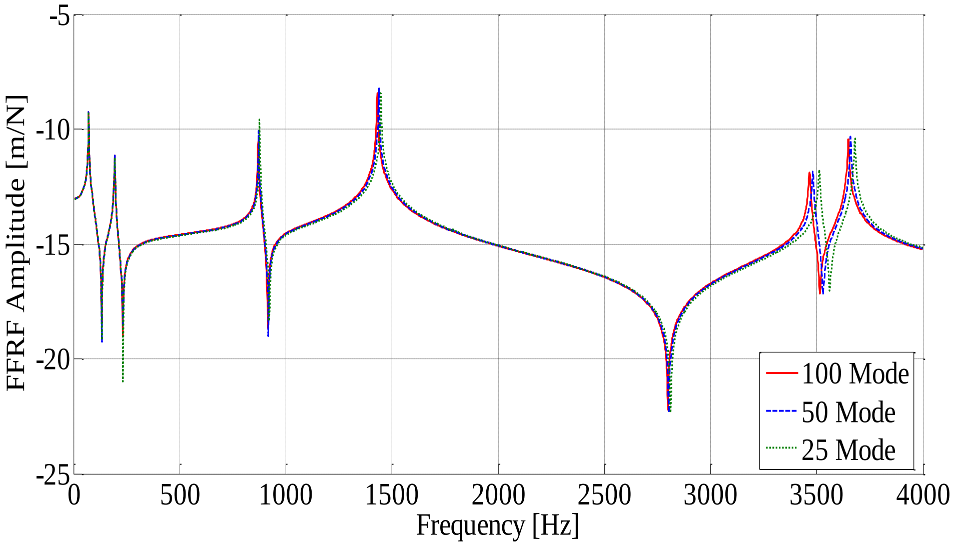

Figure 4.13 Effect of Taken Number of Modes on the Tool Point FRF of Coupled Solution

Similarly, FRF comparison is made for holder and tool parts and the natural frequencies obtained by Rayleigh-Ritz method are again very close to the coupled model solution. FRF's of the holder and tool calculated by Rayleigh-Ritz method and coupling solution is presented in Figure 4.14 and Figure 4.15. Both solutions are in good agreement in both cases.

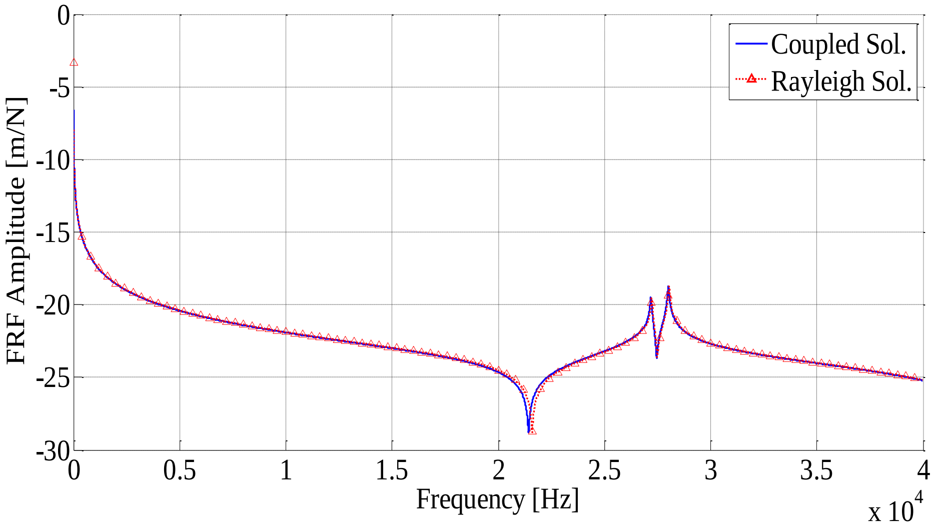

Figure 4.14 Free-Free Holder Tip Point FRF for Rayleigh and Coupled Solution

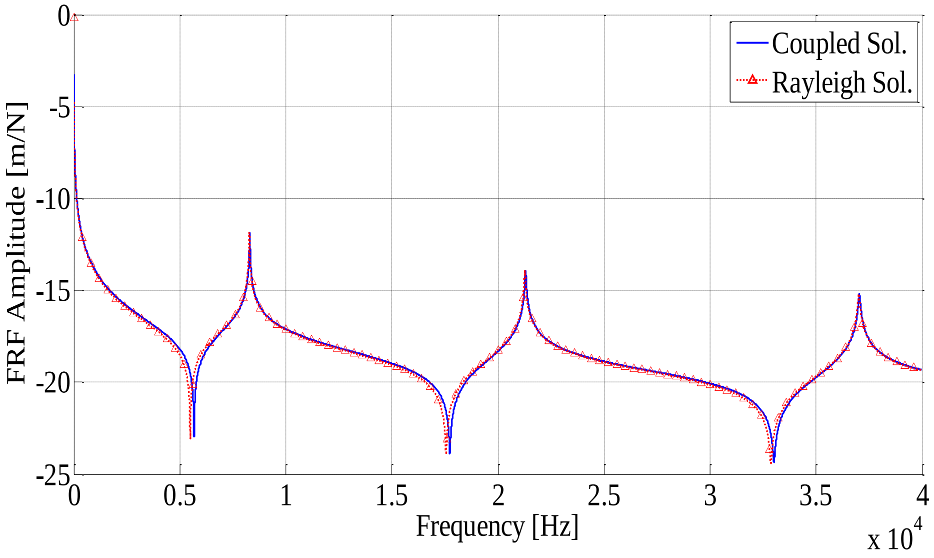

Figure 4.15 Free-Free Tool Tip Point FRF for Rayleigh and Coupled Solution

Having obtained receptances of spindle, holder and tool pieces, they are elastically coupled together using described connection parameters presented in Section 4.2. Natural frequencies of the spindle-holder-tool assembly considering Rayleigh-Ritz method, coupling method and two different ANSYS models are given in Table 4.17. Natural frequencies are very close to each other, largest error is at the 4th mode, where ANSYS 3D Solid Element solution is nearly 3% smaller than the other results.

Table 4.17 Tool Point Natural Frequencies

| Rayleigh-Ritz [Hz] | Coupled System [Hz] | ANSYS Timoshenko Beam Element [Hz] | ANSYS 3D Solid Element [Hz] |
|---|---|---|---|
| 71.7 | 71.6 | 71.6 | 71.3 |
| 194.0 | 193.8 | 193.9 | 193.0 |
| 871.9 | 870.2 | 867.5 | 867.7 |
| 1442.2 | 1430.9 | 1424.0 | 1387.4 |
| 1763.5 | 1763.5 | 1752.1 | 1752.3 |

Tool point FRF's of the coupled and Rayleigh-Ritz solutions are also quite similar to each other as shown in Figure 4.16.

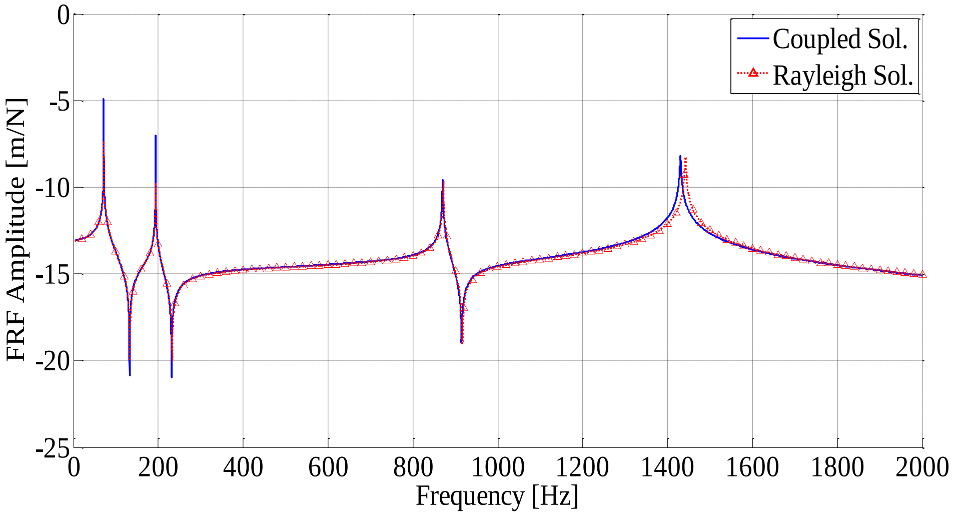

Figure 4.16 Tool Tip Point FRF for Rayleigh and Coupled Solution

Number of trial functions used in Rayleigh-Ritz method has important effect on the results. As the number of trial functions increases, convergence of the solution also increases. Figure 4.17 shows the results of tool point FRF with respect to different number of trial functions utilized. 10 and 16 trial functions are not much different from each other; however, if 5 trial functions are used, higher modes shifts towards right remarkably.

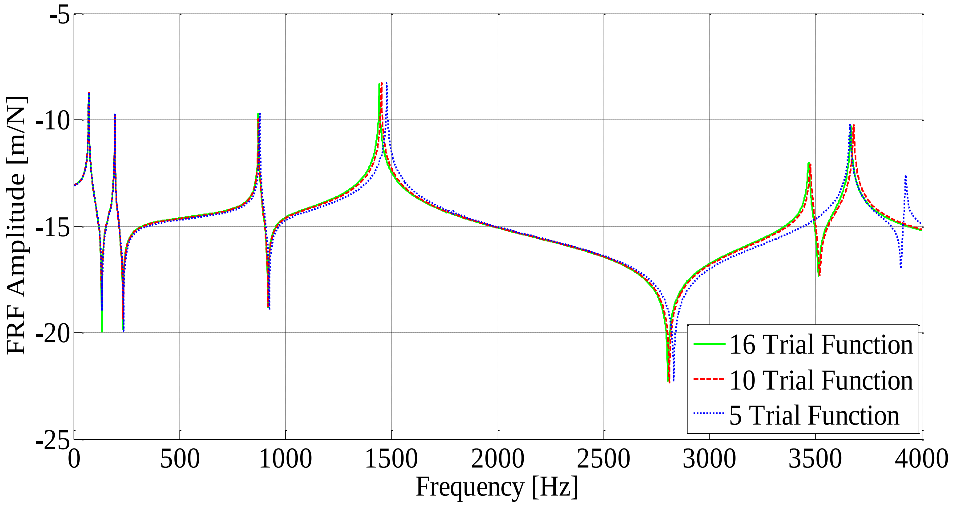

Figure 4.17 Convergence of Rayleigh-Ritz Method with respect to Number of Trial Functions Used

In addition to polynomials, mode shapes of free-free average diameter beam are also used as trial functions in Rayleigh-Ritz model. Maximum 9 free-free mode shapes can be used in the solution. In 16 polynomials are compared in Figure 4.18. They are in good agreement in general. Free-free trial functions give slightly higher natural frequencies at higher modes.

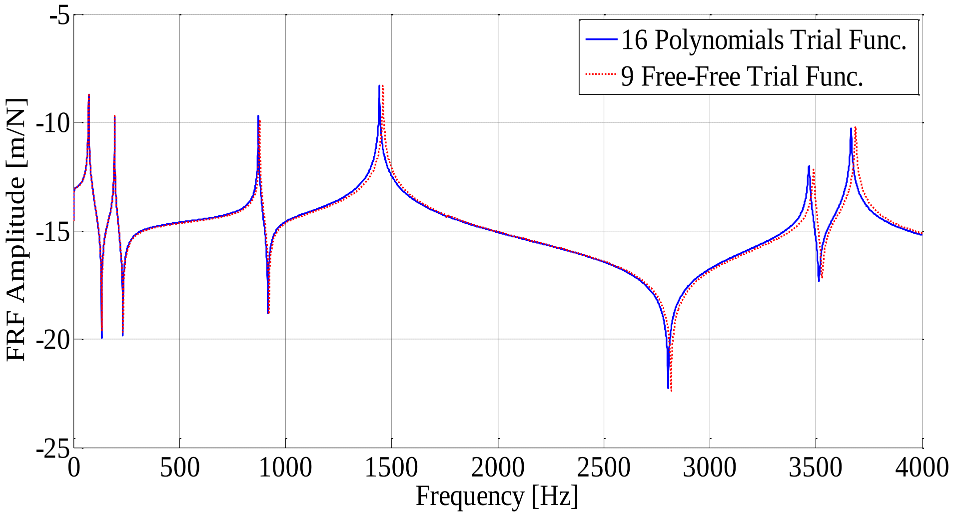

Figure 4.18 Comparison of FRFs Obtained by Polynomials and Free-Free Trial Functions

Convergence of free-free mode shapes is investigated in Figure 4.19. When the number of trial functions used is decreased to 5, higher deviations are observed at higher modes. Better convergence is obtained using 9 trial functions.

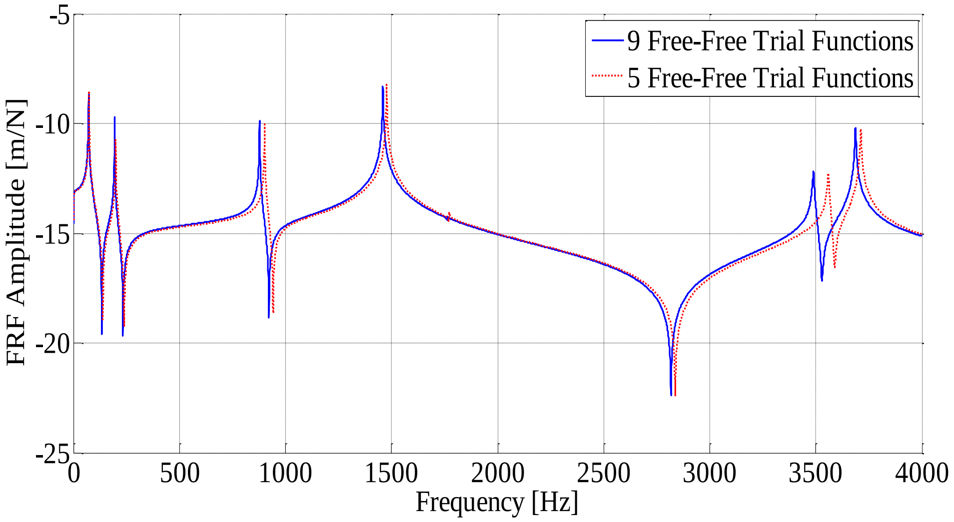

Figure 4.19 Comparison of 9 and 5 Free-Free Mode Shape Trial Functions

If elastic connection between spindle-holder and holder-tool subassemblies is assumed as rigidly connected to each other, dynamic response of total assembly can be obtained without using elastic coupling operation. If FRF of tool tip point is investigated, Figure 4.20, it is seen that the first two natural frequencies, which are due to shifted rigid body modes, match well yet other natural frequencies are not close enough. Especially Rayleigh-Ritz natural frequencies at higher modes are much larger than the coupled solution.

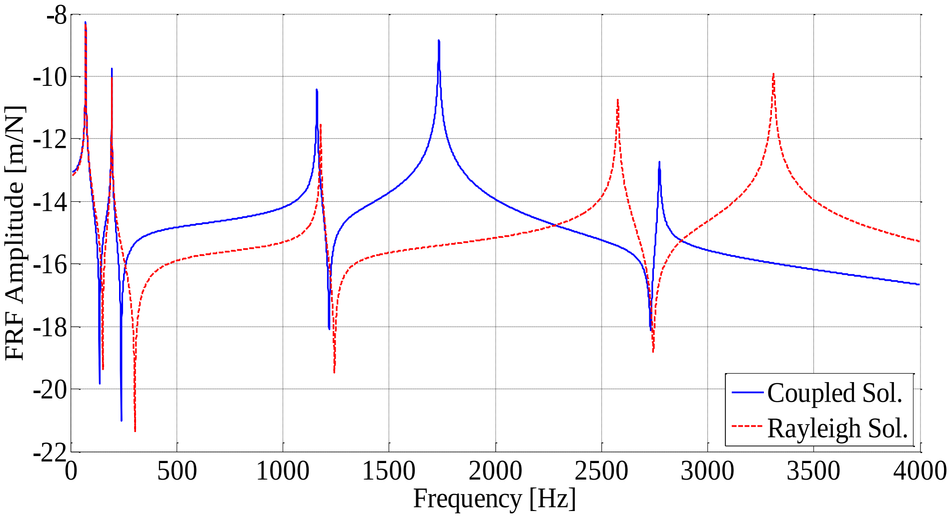

Figure 4.20 Rigidly Connected Tool Tip Point FRF

If mode shapes of rigidly connected system are investigated in FEM solution, it is seen that higher mode shapes are dominated by tool itself at the 4th mode at 1721 Hz as shown in

Figure 4.21. Mode shape of the 5th mode at 2749 Hz is shown in Figure 4.22. It can be said that trial functions used in Rayleigh-Ritz method cannot represent the exact mode shapes accurately at the given modes and solution stays far away from the exact values.

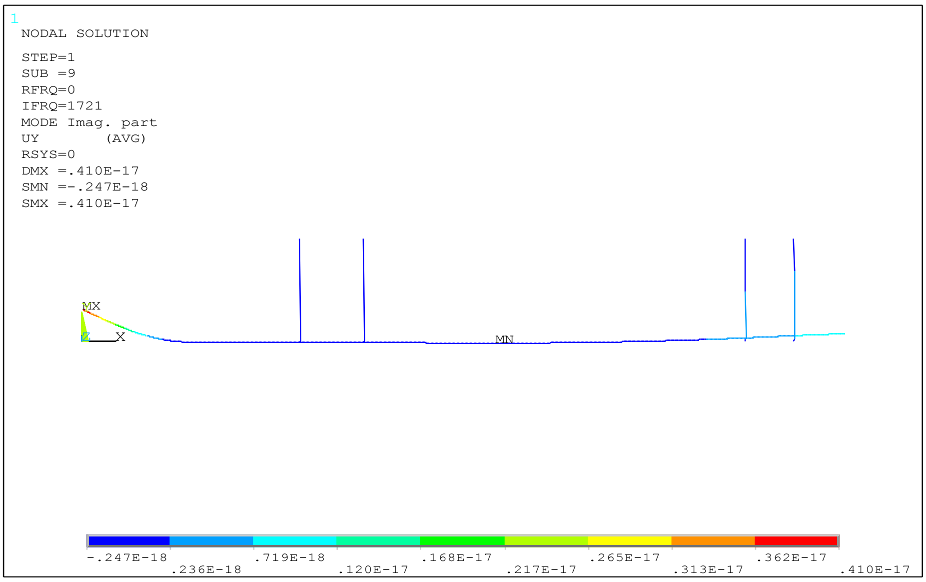

Figure 4.21 Tool Dominant Mode Shape at the 4th Mode

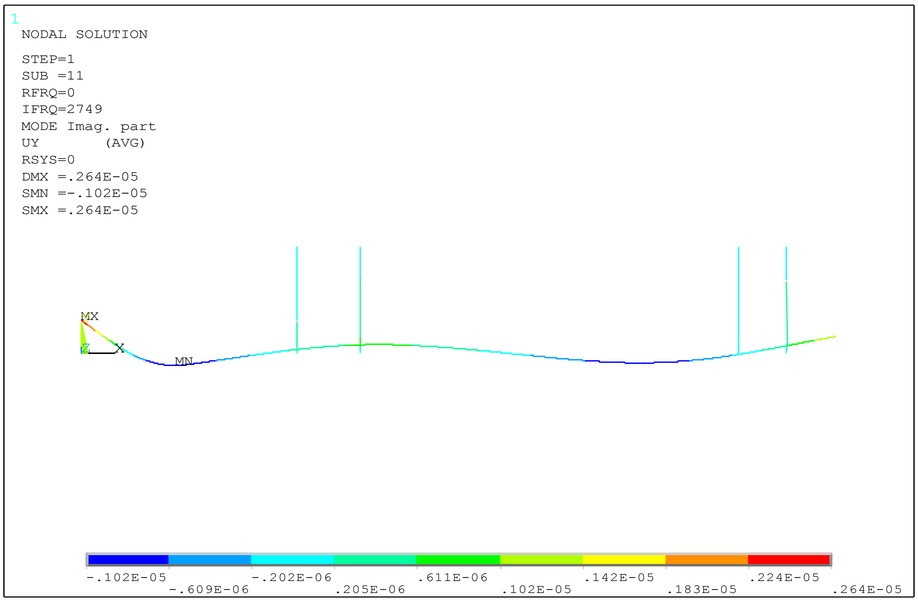

Figure 4.22 Tool Dominant Mode Shape at the 5th Mode

Then tool is removed from the assembly in order to understand the effect of tool related mode shapes. Results are given in Figure 4.23 and very good match is obtained between both solutions without tool. As a result trial functions used in Rayleigh-Ritz method should represent the systems exact mode shapes as closely as possible in order to converge to a good solution and if there is a significant difference in the diameters of the beam segments that portion should be modeled separately in order to attain good accuracy.

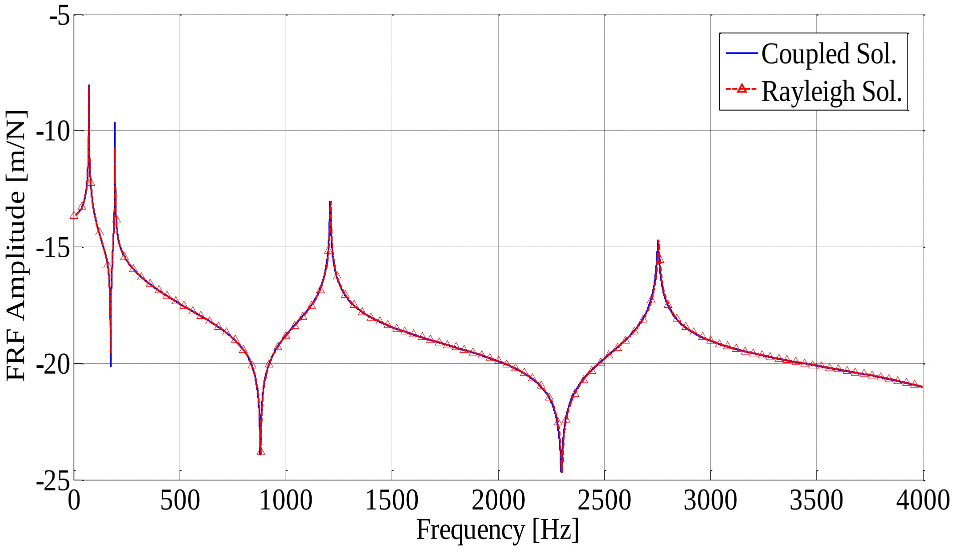

Figure 4.23 Rigidly Connected Tip Point FRF without Tool

As it is seen from the results, Rayleigh-Ritz method gives very accurate and reliable results, if used trial functions resemble the exact mode shapes.

Another advantage of Rayleigh-Ritz method is that it is very fast with respect to coupling operation. For the analysis performed on a computer with Intel i5 2.5 GHz processor and 4 GB Ram with 0.5 Hz increments in FRF construction from 0 to 2000 Hz, tool point FRF calculation takes 7.4 seconds if Rayleigh-Ritz method is used; however, coupling method takes 18 seconds. Rayleigh Ritz method is nearly 2.5 times faster than coupling method in tool point FRF calculations. This operation also includes flexible coupling. If rigid coupling is considered between spindle-holder and holder-tool, Rayleigh-Ritz method just takes 2 seconds, yet coupling takes 14.3 seconds. It is 7 times faster than the coupling method. Rayleigh-Ritz method saves a huge amount of time in calculations and also preparation time spend on the assembly is less than the coupling model.

### 4.5 Stability Lobes Results

Tool point FRF results obtained in Section 4.2 are used in order to construct stability lobes. In stability lobe construction process Budak's [32] milling stability equations are used. Stability lobes constructed considering different spindle speeds. Entry and exit angles are assumed as 0 and 90 degrees. $K_t$ and $K_r$ are taken as 796 MPa and 0.212 MPa [4]. The cutter is assumed to have 4 teeth. For the first case, stability lobes for 0 and 10000 rpm speeds are constructed as shown in Figure 4.24. Depth of cut at 10000 rpm is slightly higher than zero spindle speed condition. If other parts of stability lobe diagram are investigated, higher spindle speed results slightly higher depth of cut in general. Depth of cut increases from point A to point B as shown in the figure for 10000 rpm. Stability lobe diagram for 10000 rpm is only valid at point B because tool point FRF depends on spindle speed. Stability lobes for other desired speeds should be drawn separately.

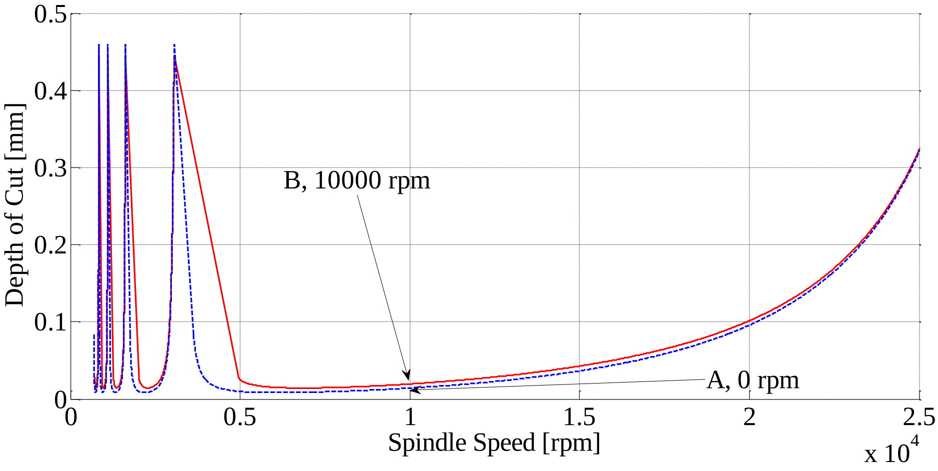

Figure 4.24 Stability Lobe at 10000 and 0 rpm Spindle Speed

In the second case, spinning speed is increased to 20000 rpm. Comparison for 0 and 20000 rpm is given in Figure 4.25. Depth of cut at 20000 rpm moves from point C to D and it is slightly increased. If comparison is made with Figure 4.24, depth of cut at 20000 rpm is larger than 10000 rpm in general. It can be said that increase in the spindle speed shifts stability lobes a little bit upward with respect to 0 spinning speed case. In both figures, there are high depth of cut pockets around 0 and 5000 rpm. At these locations depth of cut goes to very high values. It can be noticed that there is also such pocket towards 25000 rpm spindle speed. Although solutions for these two figures are only valid for 10000 and 20000 rpm, rough estimation can be done about depth of cut just considering only 0 rpm as they are slightly higher than 0 rpm results. In other words effect of spinning is limited on the stability lobe diagrams.

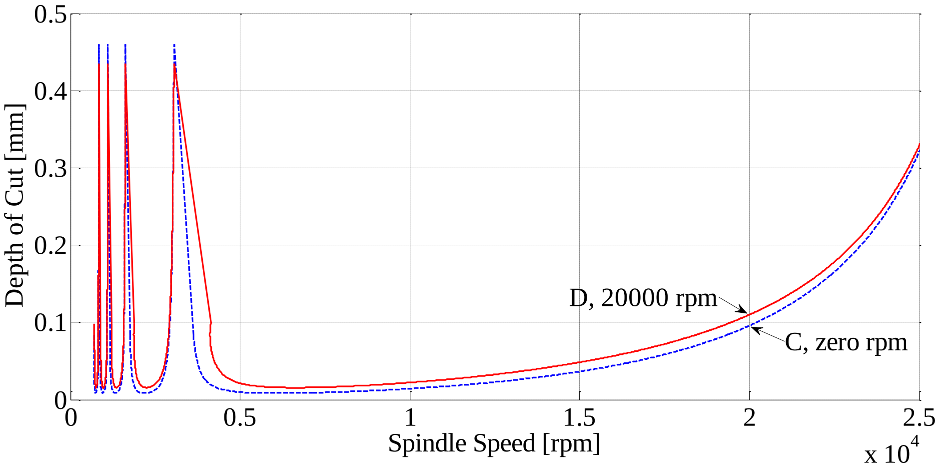

Figure 4.25 Stability Lobe at 20000 and 0 rpm Spindle Speed

However, if the exact value of depth of cut is required in one diagram, change in the tool point FRF with respect to spindle speed should be considered in the stability calculations. Considering 15000-20000 rpm spindle speeds, an example of exact stability lobe diagram is given in Figure 4.26. Green line is for 15000 rpm which is only valid at 15000 rpm point and blue line is only valid at 20000 rpm. Red line is drawn iteratively considering depth of cut at mid speeds. Red line is valid for all spindle speeds between 15000 and 20000 rpm. Full stability diagram can be obtained applying a similar procedure. However in real life situation, 0 rpm stability results are sufficient enough as the differences are not considerable; moreover, they are conservative as well.

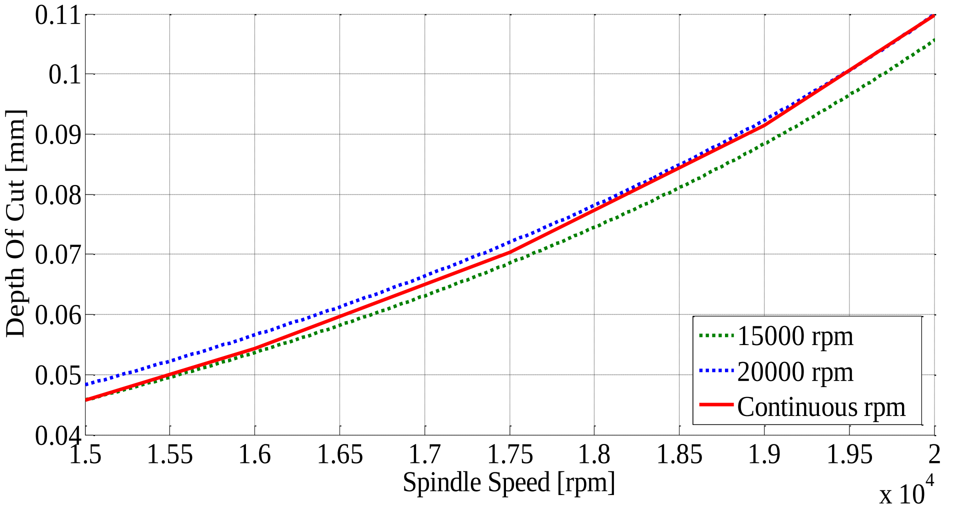

Figure 4.26 Continuous Stability Lobe Between 15000 and 20000 rpm

In Figure 4.27 stability lobe comparison for Rayleigh-Ritz model and coupled model is given. It is observed that they are nearly identical.

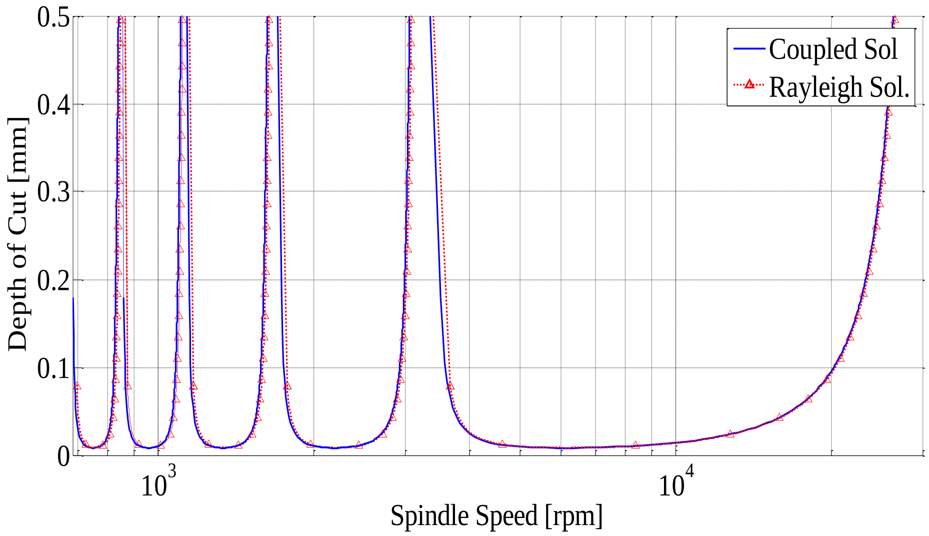

Figure 4.27 Stability Lobe Comparison for Rayleigh-Ritz and Coupled Model

# CHAPTER 5

# SUMMARY AND CONCLUSIONS

In this thesis, effects of spinning speed on the tool point FRF of the spindle-holder-tool assembly which is the most important dynamic parameter for the chatter stability are presented. Previous study is improved by including spinning into the Timoshenko beam model. Changes in the chatter stability lobe diagrams are studied considering different spindle speeds. In addition, HOBM is applied to a rectangular cross section beam and results are compared with Timoshenko beam model in order to investigate the effect of shear correction factor on the beam characteristics and changes in the natural frequencies especially for stub beams. As an alternative approach to a coupling operation, Rayleigh-Ritz method is studied in modeling of the spindle-holder-tool assembly. Tool point FRF of the system and chatter stability lobes are obtained by using Rayleigh-Ritz method as well.

## 5.1 Modeling of Spindle Assembly

Milling or turning machines can reach at very high rotational speeds, thus gyroscopic effects should be taken into account. For this reason spinning Timoshenko beam theory is employed in the continuous beam modeling.

Considering finite length beam, spinning Timoshenko beam solution is explained applying free-free end boundary conditions. Characteristic equations and related mode shapes are obtained for two different cases depending on frequency range. Since, the requirement of shear correction factor is eliminated in HOBM; it is superior with respect to Timoshenko beam theory. HOBM characteristic equation for free-free end boundary conditions is explained using a previously defined shape function.

Spindle-holder-tool assembly is composed of multiple segmented beams, each one of them is modeled as a free-free end uniform beam and those are rigidly coupled to each other using end point FRF information obtained by spinning Timoshenko beam model. Only end point receptances of the coupled structures are obtained as a result of rigid coupling operation; in other words, connection point information is no longer available. Also, bearings are added using structural modification method to the related points. In addition to this, there are flexible connections between spindle-holder and holder-tool subassemblies. In order to represent flexible connection, elastic coupling method is applied to those subassemblies. Although more time and effort is required, impedance coupling method can also be used instead of all three described coupling methods (rigid coupling, elastic coupling and structural modification methods). In impedance coupling technique, not only connection point information but also information of all desired points can also be kept; as a result of this higher order matrices should be dealt in calculations. In coupling operation, if high accuracy is desired, high number of natural frequencies and related mode shapes should be calculated for each single beam element of the assembly. Then, they are coupled together in the desired frequency range. Yet, this range is scanned step by step frequency increments meaning very long and time consuming operation. Furthermore, Rayleigh-Ritz method allows obtaining coupled response of the assembly without needing coupling operation. Huge amount of time is saved as a result of Rayleigh-Ritz method. FEM model is constructed using Timoshenko beam elements and combination elements. In addition to the Timoshenko beam elements, the assembly is also analyzed using 3D solid elements in finite element software.

## 5.2 Stability Lobe Construction

Stability lobes are determined in order to avoid chatter. Turning is an orthogonal cutting operation in which feed direction is perpendicular to the cutting direction. Turning stability lobes are easy to construct as it only needs cutting coefficient and real tool point FRF. However, milling is a more complicated process, milling geometry and related variables are time dependent. Analytical solution for milling operation is explained which results in a very fast and accurate stability lobe construction.

### 5.3 Numerical Results and Comparison

Tool point FRF of the assembly is obtained using spinning Timoshenko beam considering different spindle speeds. It is observed that, addition of the spindle speed to the model, natural frequencies of the spindle split into two part as forward and backward natural frequencies. As the spindle speed increases, difference between forward and backward natural frequencies increases as well. The same assembly with similar spindle speeds is constructed in commercial finite element software. Other than the first two natural frequencies, which are actually modification of the rigid body modes due to bearing supports, the results obtained for the elastic modes are in good agreement with the finite element solution. Difference between the finite element and analytical results are less than 1% for the first 7 natural frequencies. It should be noted that amount of separation is not significant for practical applications, as the forward and backward natural frequencies peaks are very close to each other. They could not be detected separately because of the damping in the system.

For rectangular cross section free-free end condition beam, HOBM and Timoshenko beam model are compared utilizing commonly advised shear correction factors. It is observed that commonly advised shear correction factors taken from literature gives very close results for specified rectangular beam. For the first case, beam with high slenderness ratio gives close results in both HOBM and Timoshenko beam where the difference is less than 3%. However, as the slenderness ratio is decreased, difference between HOBM and Timoshenko beam starts to increase which is dominant at higher natural frequencies. Especially at the third case, differences at the highest natural frequencies are more than 20%.

In this thesis, spindle-holder-tool assembly is constructed using Rayleigh-Ritz method and it is compared with coupled system solution assuming zero spinning speed. Natural frequencies and FRF’s of spindle shaft, holder and tool are in very good agreement for both of the solutions. Weak point of Rayleigh-Ritz is observed when the rigid connection is assumed between spindle-holder and holder-tool assemblies. If there is sharp change in the cross sections of the beams, used trial functions cannot simulate exact mode shapes and Rayleigh-Ritz natural frequencies stay far above from the exact natural frequencies. However, this deficiency is overcome by considering the assembly in two parts for which Rayleigh-Ritz method is applied separately and the obtained results are coupled to each other. It is observed that Rayleigh-Ritz method reduces computational time considerably with respect to coupling operation. For elastically connected assembly and for rigidly connected assembly, it requires 2.5 and 7 times less computational time, respectively.

Stability lobes are compared considering spinning and non-spinning cases for the coupled spindle-holder-tool assembly. It is observed that spinning speed increases the limiting depth of cut to a slightly. All stability lobes are shifted upward depending on the spinning speed. For practical applications it can be expressed that amount of shift in stability lobes is not significant. Stability lobes obtained by Rayleigh-Ritz and coupling methods are also compared and similar results are obtained.

### 5.4 Suggestions for Future Research

Bearing and contact parameters has an important role in the resultant tool point FRF. Stiffness and damping parameters are related to the type of contact used in connection point and type of bearings. Thus more realistic bearing and contact parameters can be applied to the model. Also, HOBM can be extended to the circular cross sections. More realistic tool point FRF and stability lobe calculations can be performed by using HOBM, since coupling model uses beam solutions for which the slenderness ratio is very small and application of Timoshenko beam model to those beams may not yield correct results.

# REFERENCES

[1] Tobias, S.A. and Fishwick, W. The chatter of lathe tools under orthogonal cutting conditions. *Trans. ASME.* 1958, Vol. 80, pp. 1079-1088.

[2] Tlusty, J. and Polacek, M. The stability of machine tools against self-excited vibrations in machining. *Proceedings of ASME International Research in Production Engineering, Pittsburg, USA.* 1963, pp. 465-474.

[3] Merritt, H. E. Theory of Self-Excited Machine-Tool Chatter: Contribution to Machine-Tool Chatter Research---1. *Journal of Engineering for Industry* 87(4) (1965) pp 447-454.

[4] Altintas, Y. *Manufacturing Automation.* s.l. : Cambridge University Press, 2000.

[5] F. Koenigsberger and J. Tlusty. Machine Tool Structures. Pergamon Press, 1970.

[6] R. Sridhar, R.E. Hohn, and G.W. Long. A Stability Algorithm for the General Milling Process: Contribution to Machine Tool Chatter Research---7. *Journal of Engineering for Industry* 90(2) (1968) pp 330-334.

[7] I. Minis, T. Yanushevsky. A new theoretical approach for the prediction of machine tool chatter in milling, Transactions of ASME, *Journal of Engineering for Industry* 115 (1993) 1–8.

[8] Altintaş, Y. and E. Budak. Analytical Prediction of Stability Lobes in Milling. *CIRP Annals - Manufacturing Technology* 44(1) (1995) pp 357-362.

[9] Timoshenko, S. P. On the transverse vibrations of bars of uniform cross-section. *Philosophical Magazine* 43, no. 6 (1922): 125-131.

[10] Zu, J.W. and Han, P.S. Natural frequencies and normal modes of a spinning Timoshenko beam with general boundary conditions. *Journal of Applied Mechanics.* (1992), Vol. 59, pp. 197-204.

[11] G. R. Cowper. The shear coefficient in Timoshenko's beam theory. *Journal of Applied Mechanics.* Vol 33, (1966) pp. 335-340.

[12] J.R. Hutchinson, Shear coefficients for Timoshenko beam theory, *ASME Journal of Applied Mechanics* 68 (2001) 87-92.

[13] Levinson, M. A new rectangular beam theory. *Journal of Sound and Vibration* 74, no. 1 (1981) pp. 81-87.

[14] Eisenberger, M. Dynamic stiffness vibration analysis using a high-order beam model. *International Journal for Numerical Methods in Engineering* Vol 57, (11) (2003) pp. 1603-1614.

[15] Soldatos, K. P. and C. Sophocleous On shear deformable beam theories: the frequency and normal modes of the homogeneous orthotropic bickford beam. *Journal of Sound and Vibration* Vol 242 (2) (2001) pp 215-245.

[16] T.L. Schmitz and R. Donaldson. Predicting high-speed machining dynamics by substructure analysis. *Annals of the CIRP*, 49(1):303–308, 2000.

[17] N. Arakere, T. Schmitz, C. Cheng, Rotor dynamic response of a highspeed machine tool spindle, *Proceedings of the 23rd International Modal Analysis Conference,* January 30 – February 3, 2005, Orlando, FL (on CD).

[18] Özgüven, H.N. A new method for harmonic response of nonproportionally damped structures using undamped modal data. *Journal of Sound and Vibration*, Vol. 117, (1987) pp 313-328

[19] M. Namazi. Mechanics and dynamics of the toolholder-spindle interface. *International Journal of Machine Tools and Manufacture*, 47:1333–1341, 2007.

[20] Y. Cao. Modeling of High-Speed Machine Tool-Spindle Systems. PhD thesis, The University of British Columbia, 2006.

[21] T.L. Schmitz and G.S. Duncan. Three-component receptance coupling substructure analysis for tool point dynamics prediction. Transactions of ASME - *Journal of Manufacturing Science and Engineering*, 127: 781–790, November 2005.

[22] O. Özşahin, H.N. Özgüven, and E. Budak. Estimation of dynamic contact parameters for machine tool spindle-holder-tool assemblies using artificial neural networks. *In 3rd International Conference on Manufacturing Engineering (ICMEN)*, Chalkidiki, Greece, November 2008.

[23] Movahhedy, M. R. and P. Mosaddegh. Prediction of chatter in high speed milling including gyroscopic effects. *International Journal of Machine Tools and Manufacture* 46(9) (2006) pp 996-1001.

[24] Y. Cao and Y. Altıntaş. A general method for the modeling of spindle bearing systems. *Journal of Mechanical Design*, 126:1089–1104, 2004.

[25] Ertürk, A. Dynamic modeling of spindle-tool assemblies in machining centers, M. Sc. Thesis, METU Mech. Eng. Dept., Ankara (2006).

[26] Z. M. Kılıç. Nonlınear dynamic modeling and analysis of spindle-tool assemblies in machining centers. M. Sc. Thesis, METU Mech. Eng. Dept., Ankara (2009).

[27] Han, Seon M., Haym Benaroya, and Timothy Wei. Dynamics of transversely vibrating beams using four engineering theories. *Journal of Sound and Vibration* 225, no. 5 (1999): 935-988.

[28] Bickford, W. B. A consistent higher order beam theory. *Developments in Theoretical and Applied Mechanics* 11 (1982) pp. 137-150.

[29] L. Meirovitch. Fundamentals of Vibrations. McGraw-Hill, 2001.

[30] Zhou, D. and Y. K. Cheung Vibrations of Tapered Timoshenko Beams in Terms of Static Timoshenko Beam Functions. *Journal of Applied Mechanics* 68(4) (2001) pp 596-602.

[31] T. Kocatürk, M. Şimşek. Free vibration analysis of elastically supported Timoshenko beams. *Sigma* (2005): 3.

[32] Budak, E. Analytical models for high performance milling. Part II: Process dynamics and stability. *International Journal of Machine Tools and Manufacture.* 2006, Vol. 46, pp. 1489-1499.

[33] Heyliger, P. R., and J. N. Reddy. A higher order beam finite element for bending and vibration problems. *Journal of Sound and Vibration* 126, no. 2 (1988) pp. 309-326.

[34] Rao, S. S. Mechanical Vibrations, Addison-Wesley, 1995.

# APPENDIX A

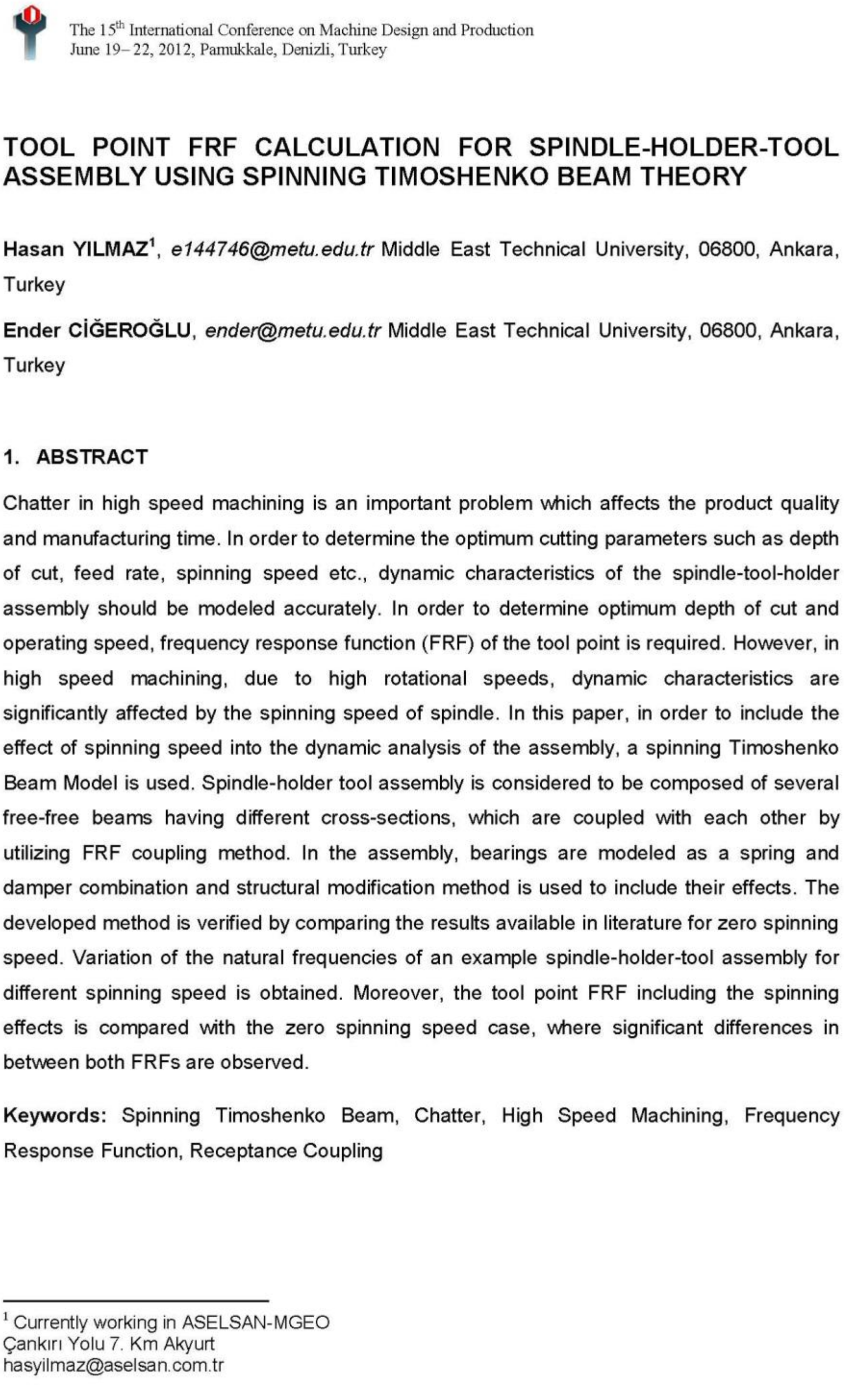

The 15th International Conference on Machine Design and Production
June 19– 22, 2012, Pamukkale, Denizli, Turkey

## TOOL POINT FRF CALCULATION FOR SPINDLE-HOLDER-TOOL ASSEMBLY USING SPINNING TIMOSHENKO BEAM THEORY

**Hasan YILMAZ**[1], *e144746@metu.edu.tr* Middle East Technical University, 06800, Ankara, Turkey

**Ender CİĞEROĞLU**, *ender@metu.edu.tr* Middle East Technical University, 06800, Ankara, Turkey

### 1. ABSTRACT

Chatter in high speed machining is an important problem which affects the product quality and manufacturing time. In order to determine the optimum cutting parameters such as depth of cut, feed rate, spinning speed etc., dynamic characteristics of the spindle-tool-holder assembly should be modeled accurately. In order to determine optimum depth of cut and operating speed, frequency response function (FRF) of the tool point is required. However, in high speed machining, due to high rotational speeds, dynamic characteristics are significantly affected by the spinning speed of spindle. In this paper, in order to include the effect of spinning speed into the dynamic analysis of the assembly, a spinning Timoshenko Beam Model is used. Spindle-holder tool assembly is considered to be composed of several free-free beams having different cross-sections, which are coupled with each other by utilizing FRF coupling method. In the assembly, bearings are modeled as a spring and damper combination and structural modification method is used to include their effects. The developed method is verified by comparing the results available in literature for zero spinning speed. Variation of the natural frequencies of an example spindle-holder-tool assembly for different spinning speed is obtained. Moreover, the tool point FRF including the spinning effects is compared with the zero spinning speed case, where significant differences in between both FRFs are observed.

**Keywords:** Spinning Timoshenko Beam, Chatter, High Speed Machining, Frequency Response Function, Receptance Coupling

---

[1] Currently working in ASELSAN-MGEO
Çankırı Yolu 7. Km Akyurt
hasyilmaz@aselsan.com.tr

## 2. INTRODUCTION

In milling and turning operations, high-speed rotation is used to decrease operation time and cost. Chatter is a phenomenon, which results in poor surface quality due to unstable machining operation. Depending on cutting speed and depth of cut, negative effect of chatter might be seen on the workpiece. In order to maximize economical gain, operating speed should be increased and negative effects of chattering on the workpiece surface needs to be eliminated. Therefore, it is absolutely necessary that stable and unstable operating areas should be determined for the working machine.

Regenerative chatter in orthogonal cutting was first explained by Tobias [1] and Tlustiy [2]. Altintas [3] developed an analytical solution for stability lobe diagram (plot of depth of cut vs. cutting speed), which includes tool point frequency response function (FRF) and a cutting constant. FRF of tool point can be either found by experimental means or analytical modeling of the spindle-holder-tool assembly. Experimental methods require significant amount of time and it is not practical to repeat the experiments considering the possible changes in the elements of the system. Therefore, in this paper, in order to predict the tool point FRF, an analytical model of the spindle-holder-tool assembly is constructed. In this model, the spindle-holder-tool assembly is modeled by series of beams, each one of which is modeled as a free-free spinning Timoshenko beam, and coupled by using FRF coupling method. Analytical solution for the spinning Timoshenko beam model for various boundary conditions is given by Zu [4]. Using the analytical natural frequencies and mode shapes of the free-free beam given in [4], end point receptances of each segment are obtained which are coupled to give the tool point FRF. In order to include the effects of bearings at various locations on the spindle, springs and dampers are added to the model by utilizing Özgüven`s structural modification method [5]. Moreover, spindle-holder and holder-tool assemblies are coupled by using elastic coupling elements.

## 3. ANALYTICAL MODELING

### Beam modeling:

In modeling of each beam segment, spinning Timoshenko beam model with free-free boundary conditions is used. Coordinate frame and rotation axis for a finite length free- free beam is shown in Fig. 1.

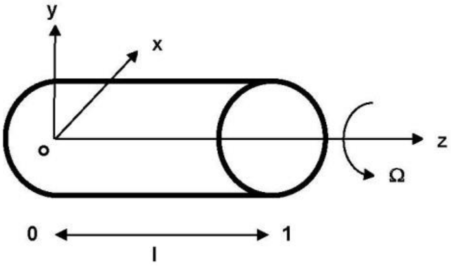

Figure 1: Reference frame for spinning shaft

Uncoupled equations of motion for the spinning Timoshenko beam obtained by Zu [4] can be given as follows

$$\frac{\rho^2 I}{\kappa G}\frac{\partial^4 u}{\partial t^4} - i\Omega\frac{\rho J_z}{\kappa G}\frac{\partial^3 u}{\partial t^3} + \rho A\frac{\partial^2 u}{\partial t^2} - \frac{\rho I}{l^2}\left(1+\frac{E}{\kappa G}\right)\frac{\partial^4 u}{\partial \zeta^2 \partial t^2} + i\Omega\frac{J_z}{l^2}\frac{\partial^3 u}{\partial \zeta^2 \partial t} + \frac{EI}{l^4}\frac{\partial^4 u}{\partial \zeta^4} = 0, \tag{1}$$

$$\frac{\rho^2 I}{\kappa G}\frac{\partial^4 \psi}{\partial t^4} - i\Omega\frac{\rho J_z}{\kappa G}\frac{\partial^3 \psi}{\partial t^3} + \rho A\frac{\partial^2 \psi}{\partial t^2} - \frac{\rho I}{l^2}\left(1+\frac{E}{\kappa G}\right)\frac{\partial^4 \psi}{\partial \zeta^2 \partial t^2} + i\Omega\frac{J_z}{l^2}\frac{\partial^3 \psi}{\partial \zeta^2 \partial t} + \frac{EI}{l^4}\frac{\partial^4 \psi}{\partial \zeta^4} = 0, \tag{2}$$

where $\rho$ is density, $I$ is transverse moment of inertia, $J_z$ is polar mass moment of inertia, $E$ is Young`s modulus, $G$ is shear modulus, $A$ is area, $\Omega$ is spin speed $\kappa$ is shear correction coefficient and $\zeta$ is the non dimensional axial position which is equal to $z/l$. In Eqs. (1) and (2)

$$u = u_x + iu_y, \tag{3}$$

$$\psi = \psi_x + i\psi_y. \tag{4}$$

where $u_x$ and $u_y$ are the deflections of the beam in $x$ and $y$ directions, respectively. Similarly, $\psi_x$ and $\psi_y$ are the corresponding bending angles in $x$ and $y$ directions. Boundary conditions for the free-free beam can be given as follows:

$$\begin{aligned} &\psi'(\zeta_0,t)=0, \quad \zeta_0=0,1 \\ &\frac{1}{l}u'(\zeta_0,t)-\psi(\zeta_0,t)=0, \quad \zeta_0=0,1 \, . \end{aligned} \tag{5}$$

The following form of solutions satisfy the partial differential equations given by Eqs. (1) and (2):

$$u(\zeta,t)=U_0 e^{ik_u\zeta}e^{i\omega t}\,, \tag{6}$$

$$\psi(\zeta,t)=\Psi_0 e^{ik_\psi\zeta}e^{i\omega t}\,, \tag{7}$$

where $U_0$ and $\Psi_0$ are complex amplitudes and $\omega$ is the natural frequency. It should be noted there is no damping in the system and complex amplitudes are used to differentiate the motions perpendicular to each other as indicated by Eqs. (3) and (4) Substituting Eqs. (6) and (7) into Eqs. (1) and (2), the following relations are obtained

$$ak_u{}^4-bk_u{}^2+c=0\,, \tag{8}$$

$$ak_\psi{}^4-bk_\psi{}^2+c=0\,. \tag{9}$$

In these equations $k_u$ and $k_\psi$ characterize the normal modes of the solution. Coefficients of these equations are given as

$$a=\frac{EI}{l^4\rho\mathrm{A}}, \quad b=\frac{I}{l^2\mathrm{A}}\left(1+\frac{E}{\kappa G}\right)\omega^2-\frac{\Omega J_z}{l^2\rho\mathrm{A}}\omega, \quad c=\frac{\rho I}{\kappa\mathrm{A}G}\omega^4-\frac{\Omega J_z}{\kappa\mathrm{A}G}\omega^3-\omega^2\,. \tag{10}$$

Since the coefficients of Eqs. (8) and (9) are the same, their solutions are as well the same and depends on $\omega$. Two different form of solutions are obtained for $\sqrt{b^2-4ac}>b$ and $\sqrt{b^2-4ac}<b$. For the former case the solution becomes

$$k_{1,2}=\pm is_1,\pm s_2 \tag{11}$$

where

$$s_1=\sqrt{\frac{-b+\sqrt{b^2-4ac}}{2a}}\,, \tag{12}$$

$$s_2=\sqrt{\frac{b+\sqrt{b^2-4ac}}{2a}}\,. \tag{13}$$

Using Eqs. (12) and (13) normal modes of $u$ and $\psi$ can be obtained as follows

$$U(\zeta)=\mathrm{A}_1\cosh(s_1\zeta)+\mathrm{A}_2\mathit{sinh}(s_1\zeta)+\mathrm{A}_3\cos(s_2\zeta)+\mathrm{A}_4\sin(s_2\zeta)\,, \tag{14}$$

$$\Psi(\zeta)=\mathrm{A}_1{}'\sinh(s_1\zeta)+\mathrm{A}_2{}'\cos h(s_1\zeta)+\mathrm{A}_3{}'\sin(s_2\zeta)+\mathrm{A}_4{}'\cos(s_2\zeta)\,, \tag{15}$$

where

$$A_1{}'=c_1A_1,\quad A_2{}'=c_1A_2,\quad A_3{}'=c_2A_3,\quad A_4{}'=-c_2A_4\,, \tag{16}$$

$$c_i=\frac{1}{s_i}\left(\frac{\rho l}{\kappa G}\omega^2+(-1)^{i+1}\frac{1}{l}s_i{}^2\right),\quad i=1,2\,. \tag{17}$$

For $\sqrt{b^2-4ac}<b$ , the solution becomes .

$$k_{1,2}=\pm s_1{}',\pm s_2, \tag{18}$$

where

$$s_1{}'=\sqrt{\frac{b-\sqrt{b^2-4ac}}{2a}}\,. \tag{19}$$

Using Eqs. (13) and (19) normal modes of $u$ and $\psi$ can be found as follows

$$U(\zeta)=\mathrm{A}_1\cos(s_1{}'\zeta)+\mathrm{A}_2\mathit{sin}(s_1{}'\zeta)+\mathrm{A}_3\cos(s_2\zeta)+\mathrm{A}_4\sin(s_2\zeta), \tag{20}$$

$$\Psi(\zeta)=\mathrm{A}_1{}'\sin(s_1{}'\zeta)+\mathrm{A}_2{}'\cos(s_1{}'\zeta)+\mathrm{A}_3{}'\sin(s_2\zeta)+\mathrm{A}_4{}'\cos(s_2\zeta)\,, \tag{21}$$

where

$$A_1{}'=c_1{}'A_1,\ A_2{}'=-c_1{}'A_2,\ A_3{}'=c_2A_3,\ A_4{}'=-c_2A_4\,, \tag{22}$$

$$c_1{}'=\frac{1}{s_1{}'}\left(\frac{\rho l}{\kappa G}\omega^2+\frac{1}{l}s_1{}'^2\right). \tag{23}$$

In order to obtain the solution, free-free end boundary conditions given in Eq. (5) are applied to Eqs. (14), (15), (20) and (21). Then the characteristic equation and the mode shapes for free-free boundary condition are obtained and for $\sqrt{b^2-4ac}>b$ , they are given as

$$\begin{aligned}&c_1s_1\left(\frac{1}{l}s_1-c_1\right)[\cosh(s_1)-\cos(s_2)]^2-\left(c_1s_1\sinh(s_1)-\frac{s_1/l-c_1}{s_2/l+c_2}c_2s_2\sin(s_2)\right)\\&*\left[\left(\frac{1}{l}s_1-c_1\right)\sinh(s_1)+\frac{c_1s_1}{c_2s_2}\left(\frac{1}{l}s_2+c_2\right)\sin(s_2)\right]=0\end{aligned}, \tag{24}$$

$$U(\zeta)=U_0\left[\cosh(s_1\zeta)-\frac{d}{s_1/l-c_1}\sinh(s_1\zeta)-\frac{c_1s_1}{c_2s_2}\cos(s_2\zeta)+\frac{d}{s_2/l+c_2}\sin(s_2\zeta)\right], \tag{25}$$

$$\Psi(\zeta)=\Psi_0\left[c_1\sinh(s_1\zeta)-\frac{dc_1}{s_1/l-c_1}\cosh(s_1\zeta)-\frac{c_1s_1}{s_2}\sin(s_2\zeta)-\frac{dc_2}{s_2/l+c_2}\cos(s_2\zeta)\right], \tag{26}$$

where

$$d=\frac{\left(\frac{1}{l}s_1-c_1\right)\sinh(s_1)+\frac{c_1s_1}{c_2s_2}\left(\frac{1}{l}s_2+c_2\right)\sin(s_2)}{\cosh(s_1)-\cos(s_2)}. \tag{27}$$

For $\sqrt{b^2-4ac}<b$, the characteristic equation and the mode shapes become as follows

$$\begin{gathered}c_1's_1'\left(\frac{1}{l}s_1'+c_1'\right)\left[\cos(s_1')-\cos(s_2)\right]^2+\left(c_1's_1'\sin(s_1')-\frac{s_1'/l+c_1'}{s_2/l+c_2}c_2s_2\sin(s_2)\right)\\ *\left[\left(\frac{1}{l}s_1'+c_1'\right)\sin(s_1')-\frac{c_1's_1'}{c_2s_2}\left(\frac{1}{l}s_2+c_2\right)\sin(s_2)\right]=0\end{gathered}, \tag{28}$$

$$U(\zeta)=U_0\left[\cos(s_1'\zeta)+\frac{d'}{s_1'/l-c_1'}\sin(s_1'\zeta)-\frac{c_1's_1'}{c_2s_2}\cos(s_2\zeta)-\frac{d'}{s_2/l+c_2}\sin(s_2\zeta)\right], \tag{29}$$

$$\Psi(\zeta)=\Psi_0\left[c_1'\sin(s_1'\zeta)-\frac{d'c_1'}{s_1'/l+c_1'}\cos(s_1'\zeta)-\frac{c_1's_1'}{s_2}\sin(s_2\zeta)+\frac{d'c_2}{s_2/l+c_2}\cos(s_2\zeta)\right], \tag{30}$$

$$d'=\frac{\left(\frac{1}{l}s_1'+c_1'\right)\sin(s_1')-\frac{c_1's_1'}{c_2s_2}\left(\frac{1}{l}s_2+c_2\right)\sin(s_2)}{\cos(s_1')-\cos(s_2)}. \tag{31}$$

$U_0$ and $\Psi_0$ are the mass normalized eigenfunctions which are obtained as follows

$$\int_0^l\begin{Bmatrix}U_s(x)\\ \Psi_s(x)\end{Bmatrix}^T\begin{bmatrix}\rho\mathrm{A} & 0\\ 0 & \rho I\end{bmatrix}\begin{Bmatrix}U_r(x)\\ \Psi_r(x)\end{Bmatrix}dx=\begin{cases}1 & \text{for} \quad s=r\\ 0 & \text{for} \quad s\neq r\end{cases}. \tag{32}$$

In addition to the elastic modes, there exist translational and rotational rigid body modes of the beam due to the free-free boundary condition, which can be given as

$$\Phi_{tr}=\frac{1}{\sqrt{\rho\mathrm{A}l}}, \tag{33}$$

$$\Phi_{rot}=\frac{1}{\sqrt{\frac{\rho\mathrm{A}l^3}{12}+\rho Il}}. \tag{34}$$

Using the mass normalized eigenfunctions, receptances of the end points of the free-free beam can be obtained. Receptance functions are denoted as $H_{jk}, N_{jk}, L_{jk}, P_{jk}$ . $H_{jk}$ and $L_{jk}$

represent linear displacement receptance of point $j$ due to a force and moment applied at point $k$, respectively. Similarly, $N_{jk}$ and $P_{jk}$ represent angular displacement receptance of point $j$ due to a force and moment applied at point $k$, respectively. These receptances can be defined as

$$H_{jk}=\sum_{r=0}^{\infty}\frac{U_r(x_j)U_r(x_k)}{(1+i\gamma)\omega_r^2-\omega^2},\ N_{jk}=\sum_{r=0}^{\infty}\frac{\Psi_r(x_j)U_r(x_k)}{(1+i\gamma)\omega_r^2-\omega^2},$$
$$L_{jk}=\sum_{r=0}^{\infty}\frac{U_r(x_j)\Psi_r(x_k)}{(1+i\gamma)\omega_r^2-\omega^2},\ P_{jk}=\sum_{r=0}^{\infty}\frac{\Psi_r(x_j)\Psi_r(x_k)}{(1+i\gamma)\omega_r^2-\omega^2}, \tag{35}$$

where $\gamma$ is the loss factor for structural damping, which is assumed to be a very small value. Substituting Eqs. (29), (30), (34) and (35) into Eq. (36), end point receptances can be obtained. For instance, $H_{11}$, linear displacement receptance of the end point due to a force applied at that point, is given as

$$H_{11}=\frac{\Phi_{tr}\Phi_{tr}+\Phi_{rot}\Phi_{rot}}{-\omega^2}+\sum_{r=1}^{\infty}\frac{U_r(l)U_r(l)}{(1+i\gamma)\omega^2-\omega^2}, \tag{36}$$

where other receptances can be obtained in a similar manner.

**Coupling of beams**

Having obtained receptances of each beam element with sufficient number of modes, these beams are coupled to each other in order to obtain the combined receptance information. After this coupling operation, receptance information of the connection points is lost and only the end point FRF information is retained. It should be noted that, in the receptance coupling of these beam elements, only inverse of 2x2 matrices is needed.

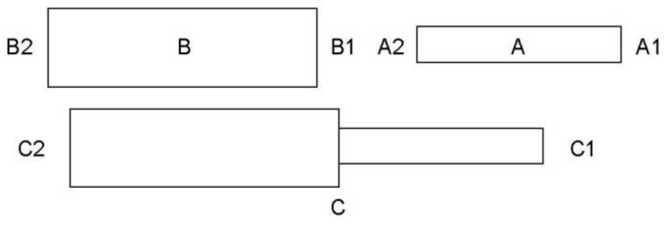

Figure 2: Coupling of beams

Receptance matrices of beam A and B can be written as follows

$$[A]=\begin{bmatrix}[A_{11}] & [A_{12}]\\ [A_{21}] & [A_{22}]\end{bmatrix},\quad [B]=\begin{bmatrix}[B_{11}] & [B_{12}]\\ [B_{21}] & [B_{22}]\end{bmatrix}. \tag{37}$$

$[A_{11}]$ is given as an example

$$[A_{11}]=\begin{bmatrix}H_{A1A1} & L_{A1A1}\\ N_{A1A1} & P_{A1A1}\end{bmatrix}. \tag{38}$$

remaining submatrices of $[A]$ and $[B]$ can be obtained similarly. End points of the new coupled structure are represented by points $C_1$ and $C_2$. After writing proper displacement and force relations at connection point, receptance matrix of the new structure, $C$ can be given as follows

$$[C]=\begin{bmatrix}[C_{11}] & [C_{12}]\\ [C_{21}] & [C_{22}]\end{bmatrix}, \tag{39}$$

where,

$$\begin{aligned}
[C_{11}]&=[A_{11}]-[A_{12}]\left[[A_{22}]+[B_{11}]\right]^{-1}[A_{21}],\\
[C_{12}]&=[A_{12}]\left[[A_{22}]+[B_{11}]\right]^{-1}[B_{12}],\\
[C_{21}]&=[B_{21}]\left[[A_{22}]+[B_{11}]\right]^{-1}[B_{21}],\\
[C_{22}]&=[B_{22}]-[B_{21}]\left[[A_{22}]+[B_{11}]\right]^{-1}[B_{12}].
\end{aligned} \tag{40}$$

It should be noted that, in order to support the spindle, bearings are used at different locations. Effect of bearings are included into the model as spring and damper elements by using Özgüven`s structural modification method [5]. Including the effects of bearings, the receptance of the structure can be written as follows

$$[\alpha_{c'}]=\left[[I]+[\alpha_c][D]\right]^{-1}[\alpha_c], \tag{41}$$

$$[\alpha_c]=\begin{bmatrix}H_{C1C1} & L_{C1C1} & H_{C1C2} & L_{C1C2}\\ N_{C1C1} & P_{C1C1} & N_{C1C2} & P_{C1C2}\\ H_{C2C1} & N_{C2C1} & H_{C2C2} & L_{C2C2}\\ N_{C2C1} & N_{C2C1} & N_{C2C2} & P_{C2C2}\end{bmatrix}, \tag{42}$$

In Eqn. (41) effect of bearing is included in $[D]$ matrix. If bearing is located at $[C_2]$ in Fig. 2, dynamic stiffness matrix of bearing can be written as follows,

$$[D]=\begin{bmatrix} 0 & 0 & 0 & 0 \\ 0 & 0 & 0 & 0 \\ 0 & 0 & k_y+i\omega c_y & 0 \\ 0 & 0 & 0 & k_\theta+i\omega c_\theta \end{bmatrix}. \tag{43}$$

Where $(k_y, c_y)$ and $(k_\theta, c_\theta)$ are translational and rotational stiffness and damping coefficients of the bearings, respectively. Computational effort in the calculation of Eq. (41) can be decreased if the matrices are reordered such that connection degrees of freedoms are grouped at the upper left corner. The reordered dynamic stiffness matrix can be written in the following form,

$$[D]=\begin{bmatrix} [D_{11}] & 0 \\ 0 & 0 \end{bmatrix},\ [D_{11}]=\begin{bmatrix} k_y+i\omega c_y & 0 \\ 0 & k_\theta+i\omega c_\theta \end{bmatrix}. \tag{44}$$

In addition to this, $[\alpha_c]$ is rearranged in the same manner. Reordering these matrices as described above, size of the inverted matrix decreases from 4 to 2. Therefore, the receptance matrix of the coupled system including the bearings can obtained as follows

$$\begin{aligned} \left[\alpha_{c'}{}^{11}\right] &= \left[[I]+\left[\alpha_c{}^{11}\right]\left[D^{11}\right]\right]^{-1}\left[\alpha_c{}^{11}\right], \\ \left[\alpha_{c'}{}^{12}\right]^T &= \left[\alpha_{c'}{}^{21}\right]=\left[\alpha_c{}^{21}\right]\left[[I]-\left[D^{11}\right]\left[\alpha_{c'}{}^{11}\right]\right], \\ \left[\alpha_{c'}{}^{22}\right] &= \left[\alpha_c{}^{22}\right]-\left[\alpha_c{}^{21}\right]\left[D^{11}\right]\left[\alpha_{c'}{}^{12}\right]. \end{aligned} \tag{45}$$

The receptances obtained by Eq. (45) should be reordered back to the original form in order to get similar submatrices as before. For the coupling of tool holder to the spindle assembly, flexible receptance coupling is needed on the contrary to rigid receptance coupling. Formulation of flexible receptance coupling includes spring and damper elements between two beam segments (A and B). The coupling stiffness matrix can be written in the following form

$$[K_{AB}]=\begin{bmatrix} k_y{}^{AB}+i\omega c_y{}^{AB} & 0 \\ 0 & k_\theta{}^{AB}+i\omega c_\theta{}^{AB} \end{bmatrix}, \tag{46}$$

where $k_y{}^{AB}$ and $k_\theta{}^{AB}$ are translational and rotational stiffnesses, and, $c_y{}^{AB}$ and $c_\theta{}^{AB}$ are translational and rotational damping coefficients of the flexible connection. In flexible receptance coupling, force and displacement relations are written at the connection point similar to rigid coupling where equations for the stiffness and damping elements areas well included in equations. The resulting equations for the receptance is given as follows.

$$\begin{aligned}
[C_{11}] &= [A_{11}] - [A_{12}]\left[[A_{22}] + [K_{AB}]^{-1} + [B_{11}]\right]^{-1}[A_{21}],\\
[C_{12}] &= [A_{12}]\left[[A_{22}] + [K_{AB}]^{-1} + [B_{11}]\right]^{-1}[B_{12}],\\
[C_{21}] &= [B_{21}]\left[[A_{22}] + [K_{AB}]^{-1} + [B_{11}]\right]^{-1}[B_{21}],\\
[C_{22}] &= [B_{22}] - [B_{21}]\left[[A_{22}] + [K_{AB}]^{-1} + [B_{11}]\right]^{-1}[B_{12}].
\end{aligned} \tag{47}$$

**Verification of the model**

For a case study, the spindle-holder-tool model given by Erturk [6, 7] and shown in Fig. 3 is used in this study. The results given by Erturk [6, 7] are for zero spinning speed and they are used here in order to verify the developed model. The material and geometrical properties of the spindle-holder-tool assembly are given in Table 1. At 4 locations, springs are added to simulate bearings. Location of each bearing and the corresponding stiffness values are given in Table 2.

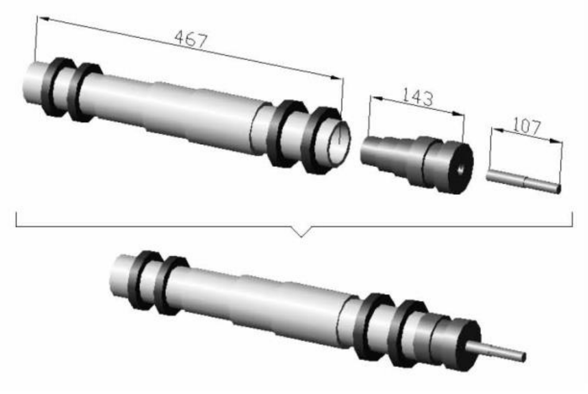

Figure 3: Spindle assembly [6]

Table 1a: Spindle Dimensions [6]

| **Segment Number** | **1** | **2** | **3** | **4** | **5** | **6** | **7** | **8** | **9** | **10** |
|---|---|---|---|---|---|---|---|---|---|---|
| **Length (mm)** | 26 | 26 | 26 | 38 | 100 | 66 | 75 | 30 | 40 | 40 |
| **Outer Diameter (mm)** | 66 | 66 | 66 | 66 | 76 | 70 | 62 | 58 | 58 | 58 |
| **Inner Diameter (mm)** | 54 | 48 | 40 | 32 | 32 | 32 | 32 | 32 | 32 | 32 |

Table 1b: Holder Dimensions [6]

| **Segment Number** | 1 | 2 | 3 | 4 | 5 | 6 |
|---|---|---|---|---|---|---|
| **Length (mm)** | 22 | 19 | 24 | 26 | 26 | 26 |
| **Outer Diameter (mm)** | 72 | 60 | 70 | 54 | 48 | 40 |
| **Inner Diameter (mm)** | 16 | 16 | 16 | 16 | 16 | 16 |

Table 1c: Tool Dimensions [6]

| **Segment Number** | 1 | 2 |
|---|---|---|
| **Length (mm)** | 50 | 57 |
| **Outer Diameter (mm)** | 14 | 26 |
| **Inner Diameter (mm)** | 0 | 0 |

Table 1d: Material Properties [6]

| | |
|---|---|
| **$\rho$ (density)** | 7800 kg/m^3 |
| **$\nu$ (poisson ratio)** | 0.3 |
| **$\gamma$ (damping factor)** | 0.003 |
| **E (Young's Modulus)** | 200 Gpa |

Table 2a: Bearing and Interface Properties [6]

| | **Translational Stiffness (N/mm)** | **Rotational Stiffness (N/mm)** |
|---|---|---|
| **Front Bearings (for each)** | 7.5 x10^5 | - |
| **Rear Bearings (for each)** | 2.5 x10^6 | - |
| **Spindle Holder Interface** | 5 x10^7 | 1.5 x10^6 |
| **Holder Tool Interface** | 2 x10^8 | 1.5 x10^6 |

Table 2b: Bearing Locations [6]

| **Bearing No** | **Bearing 1** | **Bearing 2** | **Bearing 3** | **Bearing 4** |
|---|---|---|---|---|
| **Distance (mm)** | 26 | 78 | 387 | 427 |

Table 3 gives the comparison of natural frequencies obtained by the current method and the method developed by Ertürk et al. [7]. Natural frequencies are obtained from frequency response function which is determined by using 0.1 Hz increments. Since damping included in the system is very small resonance frequencies in the FRF corresponds to the natural frequencies of the spindle-holder-tool assembly with an error of $\pm$0.1 Hz. It is observed that the results for zero spinning speed are very close to the results obtained from the literature. It should be noted that the maximum error compared to Ansys is less than 3% in the first seven modes. Additionally, receptance of tool point is given in Fig. 4 which is identical to the one given in [7]

Table 3: Natural Frequencies and comparison with previous work

| | Current Model | Erturk [6] | Ansys [6] | % Difference wrt Erturk [6] | % Difference wrt Ansys |
|---|---|---|---|---|---|
| **Mode 1** | 72 | 71,7 | 71,6 | 0,42 | 0,56 |
| **Mode 2** | 195,1 | 195 | 193,8 | 0,05 | 0,67 |
| **Mode 3** | 881,5 | 877,8 | 867,5 | 0,42 | 1,61 |
| **Mode 4** | 1452,3 | 1438,3 | 1424,3 | 0,96 | 1,97 |
| **Mode 5** | 1793,1 | 1819,5 | 1752,6 | 1,47 | 2,31 |
| **Mode 6** | 3529,5 | 3639,3 | 3442,5 | 3,11 | 2,53 |
| **Mode 7** | 3698,6 | 3812,5 | 3634,8 | 3,08 | 1,76 |

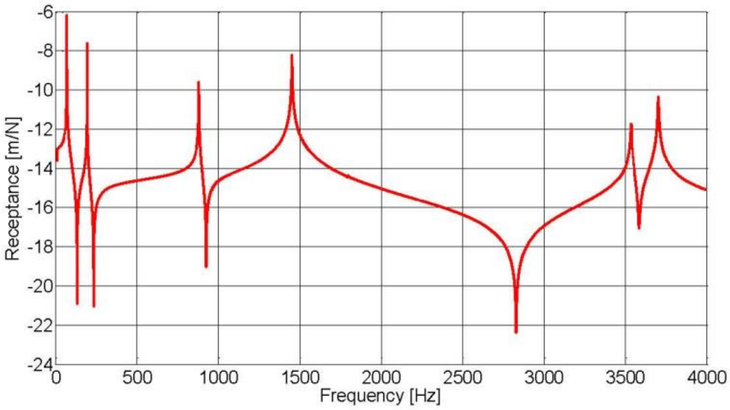

Figure 4: Tool point FRF results of current work

**Effect of spinning on free-free end conditioned beam**

Dynamic characteristics of rotating beams change with respect to spinning speed. Natural frequencies split as backward and forward natural frequencies. As spinning speed increases, difference between backward and forward natural frequencies increases as well. In order to examine the difference, a steel cylinder of 1 m length and 0.2 m diameter is studied. First, for zero spinning speed , natural frequencies are obtained and taking the first natural frequency as a reference ($\omega_1 = 5290\, rad/s$), spinning speed of $\omega_1$ and $2\omega_1$ are considered. The first three natural frequencies obtained for the three cases are given in Table 4. It is observed that for higher modes the difference between the forward and backward frequencies increases. In addition to natural frequencies, end point receptance of the free-free beam is obtained for $\Omega = 0$ and $\Omega = \omega_1$, which are given in Figure 5. It is observed, single modes split in to two modes having natural frequencies lower and larger than the zero spin case as predicted by the natural frequencies. Moreover, there is an additional mode at a very low frequency (49 Hz) for the case including gyroscopic effects. This frequency is not presented in Table 4 for easy comparison.

Table 4: Natural frequencies rad/s at $0$, $\omega_1$ and $2\omega_1$

| | | $\Omega = \omega_1$ | | | | $\Omega = 2\omega_1$ | | | |
|---|---|---|---|---|---|---|---|---|---|
| | $\Omega = 0$ | **FWD** | **% Diff. wrt** $\Omega = 0$ | **BWD** | **% Diff. wrt** $\Omega = 0$ | **FWD** | **% Diff. wrt** $\Omega = 0$ | **BWD** | **% Diff. wrt** $\Omega = 0$ |
| **1. Nat. Freq** | 5290 | 5805 | 9,7 | 4792 | 9,4 | 6346 | 20,0 | 4338 | 18,0 |
| **2. Nat. Freq** | 12770 | 13569 | 6,3 | 11963 | 6,3 | 14367 | 12,5 | 11186 | 12,4 |
| **3. Nat. Freq** | 21780 | 22717 | 4,3 | 20809 | 4,5 | 23631 | 8,5 | 19852 | 8,9 |

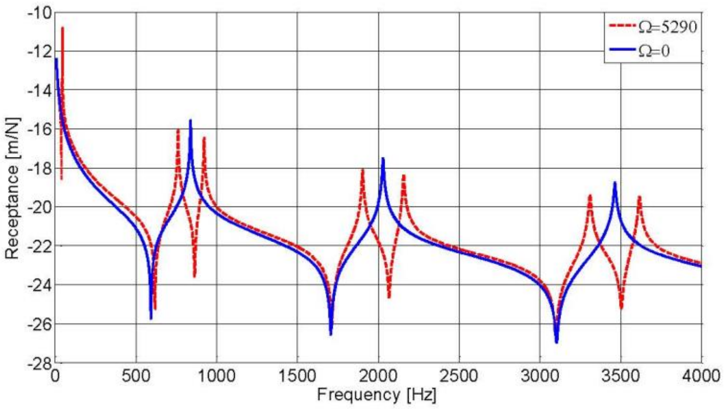

Figure 5: Forward and backward natural frequencies at $\omega_1$

## 4. CONCLUSIONS

In this paper, spindle-holder-tool assembly is constructed employing receptance coupling of several free free beams. Spinning Timoshenko beam model is used to model the free free beam segments. Springs are utilized at different locations to simulate bearings and small damping, which does not affect the natural frequencies, is assumed in the connections. The results of present work is verified by comparing the results available in literature for zero spinning speed, which are determined to be very close to each other.

In order to investigate the effects of spinning speed natural frequencies of a free-free beam are obtained for different spinning speeds. It is observed that natural frequencies split into forward and backward natural frequencies and the amount of separation increases as the spinning speed of the beam increases. The same results also observed for the end point FRF of the free beam; hence, this will have significant effects on the stability lobe diagrams. Therefore, for high speed machining, in order to obtain optimum cutting parameters accurately, gyroscopic effects should as well be included into the model of the spindle-holder-tool assembly. As a future work, the developed model will be used to obtain the tool point FRF and the corresponding stability lobe diagram of the spindle-holder-tool assembly and the effect of variation of spindle speed will be studied.

## 5. REFERENCES

1. **Tobias, S.A. and Fishwick, W., (1958),** "The chatter of lathe tools under orthogonal cutting conditions", Trans. ASME, Vol. 80, pp 1079-1088.

2. **Tlusty, J. and Polacek, M., (1963),** The stability of machine tools against self-excited vibrations in machining", Proceedings of ASME International Research in Production Engineering, Pittsburg, USA, pp 465-474.

3. **Altıntaş , Y., (2000),** "Manufacturing Automation", Cambridge University Press.

4. **Zu, J.W. and Han, P.S., (1992),** "Natural Frequencies and Normal Modes of a Spinning Timoshenko Beam With General Boundary Conditions", Journal of Applied Mechanics, Vol. 59, pp 197-204.

5. **Özgüven, H.N., (1987),** "A new method for harmonic response of nonproportionally damped structures using undamped modal data", Journal of Sound and Vibration, Vol. 117, pp 313-328.

6. **Ertürk, A., (2006),** "Dynamic modeling of spindle-tool assemblies in machining centers ", M. Sc. Thesis, METU Mech. Eng. Dept., Ankara.

7. **Ertürk, A. Özüven, H.N. and Budak, E., (2006),** "Analytical modeling of spindle-tool dynamics on machine tools using Timoshenko beam model receptance coupling for the prediction of tool point FRF", International Journal of Machine Tools and Manufacture, Vol. 46, pp 1901-1912.

# APPENDIX B

*IMAC A Conference and Exposition on Structural Dynamics 11-14 February 2013 California USA*

## Effect of Spin Speed on Stability Lobes in High Speed Machining

Hasan Yılmaz[†‡], Ender Cigeroglu[†]

[†] Middle East Technical University, 06800, Ankara, Turkey

[‡] Aselsan MGEO, 06750, Ankara, Turkey

### ABSTRACT

In milling and turning processes high speed rotation is used to decrease operation time; as a result, the cost of machining operation is as well reduced. In order to estimate the stability lobes and determine optimum cutting conditions, tool point Frequency Response Function (FRF) is required. Euler and Timoshenko beam models are employed in literature in order to obtain tool point FRF of spindle-holder-tool assemblies. However, due to the high speed rotation of spindle, it is also necessary to consider gyroscopic effects for the determination of tool point FRF. In this paper, spindle-holder-tool assembly is modeled by Timoshenko beam theory considering gyroscopic effects as well. Considering the analytical modal solution available in literature and structural coupling methods, FRF of the tool point is obtained. A case study is performed on an example of spindle-holder-tool assembly, which is as well modeled by finite elements in order to verify the results obtained by the continuous model. Next, using the continuous model, stability lobes are obtained for different spin speeds and the effect of gyroscopic forces are studied.

**Keywords:** Spinning, Timoshenko beam, Chatter, Vibrations, Gyroscopic effects, High speed machining, Stability lobes

### INTRODUCTION

High speed machining is employed in milling or turning operation in order to decrease machining time as well as the cost of the operation. As a result of this dynamics of the spinning system is crucial to satisfy design requirements, especially for mass production. Inaccurate modeling of spindle-holder-tool dynamics may cause chatter which results in poor surface quality in the work piece. Regenerative chatter in orthogonal cutting was first explained by Tobias [1] and Tlusty [2]. Milling stability analysis is different than orthogonal cutting process which includes time dependent geometry and variables. Budak [3, 4] developed an analytical solution for milling stability lobe diagram. Altintas [5] explained constructing stability lobes for both orthogonal and milling cutting operations using specified Frequency Response Functions (FRF). Tool point FRF of the system is required to construct milling stability lobe diagrams. FRF of the tool point can be either found by experiments or analytical modeling of the spindle-holder-tool assembly. Experimental methods require significant amount of time and it is not practical to repeat the experiments considering the possible changes in the elements of the system. Therefore, in this paper, in order to predict the tool point FRF, an analytical model of the spindle-holder-tool assembly is constructed. In this model, the spindle-holder-tool assembly is modeled by series of beams, each one of which is modeled as a free-free spinning Timoshenko beam, and coupled by using FRF coupling method. Analytical solution for the spinning Timoshenko beam model for various boundary conditions is given by Zu [6]. Using the analytical natural frequencies and mode shapes of the free-free beam given by Zu [6], end point receptances of each segment are obtained which are coupled to give the tool point FRF. In order to include the effects of bearings at various locations on the spindle, springs and dampers are added to the model by utilizing Özgüven`s structural modification method [7]. Moreover, spindle-holder and holder-tool assemblies are coupled by using elastic coupling elements.

## ANALYTICAL MODEL

### Spinning Timoshenko Beam Model

In the modeling of spindle, a spinning Timoshenko beam model having free-free boundary conditions is employed. Non-dimensional partial differential equations of motion are given as follows [6]:

$$\frac{\partial^2 u}{\partial t^2}+\frac{\kappa G}{\rho l^2}\left(l\frac{\partial \psi}{\partial \zeta}-\frac{\partial^2 u}{\partial \zeta^2}\right)=F, \tag{1}$$

$$\frac{\partial^2 \psi}{\partial t^2}-i\frac{\Omega J_z}{\rho I}\frac{\partial \psi}{\partial t}-\frac{E}{\rho l^2}\frac{\partial^2 \psi}{\partial \zeta^2}+\frac{\kappa AG}{\rho Il}\left(l\psi-\frac{\partial u}{\partial \zeta}\right)=0, \tag{2}$$

where $u$ is the transverse displacement, $\psi$ is the rotation of the cross-section and $F$ is the applied transverse force. In these equations, $l$ is beam length, $\rho$ is density, $I$ is transverse moment of inertia, $J_z$ is polar mass moment of inertia, $E$ is Young`s modulus, $G$ is shear modulus, $A$ is cross-sectional area, $\Omega$ is spin speed, $\kappa$ is shear correction factor and $\zeta$ is the non-dimensional axial position. Solution of Eqs. (1) and (2) can be written in the following form [6]

$$U(\zeta)=\mathrm{A}_1\cosh(s_1\zeta)+\mathrm{A}_2 sinh(s_1\zeta)+\mathrm{A}_3\cos(s_2\zeta)+\mathrm{A}_4\sin(s_2\zeta), \tag{3}$$

$$\Psi(\zeta)=\mathrm{A}_1'\sinh(s_1\zeta)+\mathrm{A}_2'\cos h(s_1\zeta)+\mathrm{A}_3'\sin(s_2\zeta)+\mathrm{A}_4'\cos(s_2\zeta), \tag{4}$$

where $\mathrm{A}_1$, $\mathrm{A}_1'$, $s_1$ and $s_2$ are related parameters which are given in [6] in detail. Using free-free boundary conditions and substituting Eqs. (3) and (4) into Eqs. (1) and (2), natural frequencies and mode shapes of free-free spinning beam is obtained. Solutions for this BC's and other desired BC's are given in [6].

Eqs. (1) and (2) can be written in matrix form as follows

$$[M]\{\dot{W}(x,t)\}-[K]\{W(x,t)\}=\{F\}, \tag{5}$$

$$\{W\}=\{\dot{U}(x,t)\ U(x,t)\ \dot{\Psi}(x,t)\ \Psi(x,t)\}^T, \tag{6}$$

$$\{F\}=\{0\ F\ 0\ 0\}^T, \tag{7}$$

where $[M]$ and $[K]$ matrices are given as follows

$$[M]=\begin{bmatrix} 0 & \rho A & 0 & 0 \\ \rho A & 0 & 0 & 0 \\ 0 & 0 & 0 & \rho I \\ 0 & 0 & \rho I & -i\Omega J_z \end{bmatrix},\quad [K]=\begin{bmatrix} \rho A & 0 & 0 & 0 \\ 0 & \frac{\kappa AG}{l^2}\frac{\partial^2}{\partial \zeta^2} & 0 & -\frac{\kappa AG}{l}\frac{\partial}{\partial \zeta} \\ 0 & 0 & \rho I & 0 \\ 0 & \frac{\kappa AG}{l}\frac{\partial}{\partial \zeta} & 0 & \frac{E}{l}\frac{\partial^2}{\partial \zeta^2}+\kappa AG \end{bmatrix}. \tag{8}$$

Using the modal expansion theorem, solution of this system can be written in terms of its mode shapes as

$$\{W(x,t)\} = \sum_{r=-N_m}^{N_m} z_r(t)\{W_r(x)\}, \tag{9}$$

where $z_r$ is the modal coefficient of the $r^{th}$ mode. Multiplying each side of Eq.(5) by $\{W_s\}^T$, integrating over the length and using the orthogonality conditions, the following equation of motion is obtained,

$$M_r\dot{z}_r(t) - K_r z_r(t) = Q_r(t) \tag{10}$$

where $M_r$, $K_r$ and $Q_r(t) = U_r(x_k)F(t)$ are the modal mass and modal stiffness and the modal forcing for the $r^{th}$ mode. Solution of this uncoupled differential equation for a harmonic forcing of $F(t) = Fe^{i\omega t}$ applied at $x = x_k$ becomes as follows

$$z_r(t) = \frac{U_r(x_k)Fe^{i\omega t}}{M_r(i\omega - \lambda_r)}. \tag{11}$$

Total response of the beam becomes as follows,

$$\{W(x,t)\} = \sum_{r=-N_m}^{N_m} \frac{U_r(x_k)Fe^{i\omega t}}{M_r(i\omega - \lambda_r)}\{W_r(x)\} \tag{12}$$

where $N_m$ is the number of modes used in the modal expansion. Using the mass normalized eigenfunctions, receptances of the end points of the free-free beam can be obtained for a transverse forcing applied on the beam. Receptance functions are denoted as $H_{jk}, N_{jk}, L_{jk}, P_{jk}$. $H_{jk}$ and $L_{jk}$ represent linear displacement receptance of point $j$ due to a unit force and moment applied at point $k$, respectively. Similarly, $N_{jk}$ and $P_{jk}$ represent angular displacement receptance of point $j$ due to a force and moment applied at point $k$, respectively. If small structural damping is assumed as $(1+i\gamma)$. Following a similar procedure, receptance for an applied moment can be obtained all these receptances can be defined as

$$H_{jk} = \sum_{r=-N_m}^{N_m} \frac{U_r(x_j)U_r(x_k)}{i\omega - \lambda_r(1+i\gamma)}, N_{jk} = \sum_{r=-N_m}^{N_m} \frac{\Psi_r(x_j)U_r(x_k)}{i\omega - \lambda_r(1+i\gamma)}, L_{jk} = \sum_{r=-N_m}^{N_m} \frac{U_r(x_j)\Psi_r(x_k)}{i\omega - \lambda_r(1+i\gamma)}, P_{jk} = \sum_{r=-N_m}^{N_m} \frac{\Psi_r(x_j)\Psi_r(x_k)}{i\omega - \lambda_r(1+i\gamma)}, \tag{13}$$

where $\gamma$ is the loss factor for structural damping, which is assumed to be a very small value in the case studies considered.

### Coupling of Beams

After obtaining the receptances of each beam element utilizing sufficient number of modes, these beams are coupled to each other in order to obtain the combined receptance of the tool point. Fig. 1 shows coupling of two beamsegments. Receptance matrices for beams A and B can be found utilizing Eq. (13) at the two extreme points. The coupled structure is represented as beam C.

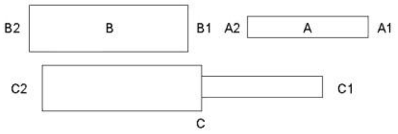

**Fig. 1** Coupling of Beams

Receptance matrix of the coupled structure can be found as follows [8]:

$$\begin{aligned}
[C_{11}] &= [A_{11}] - [A_{12}]\big[[A_{22}] + [B_{11}]\big]^{-1}[A_{21}], \\
[C_{12}] &= [A_{12}]\big[[A_{22}] + [B_{11}]\big]^{-1}[B_{12}], \\
[C_{21}] &= [B_{21}]\big[[A_{22}] + [B_{11}]\big]^{-1}[B_{21}], \\
[C_{22}] &= [B_{22}] - [B_{21}]\big[[A_{22}] + [B_{11}]\big]^{-1}[B_{12}],
\end{aligned} \tag{14}$$

where $[A_{11}]$ is given as follows

$$[A_{11}] = \begin{bmatrix} H_{A1A1} & L_{A1A1} \\ N_{A1A1} & P_{A1A1} \end{bmatrix}, \tag{15}$$

and $[B_{11}]$ can be found in a similar fashion. It should be noted that, in order to support the spindle, bearings are used at different locations. Effect of bearings are included into the model as translational/rotational spring and damper elements by using Özgüven`s structural modification method [7]. Although impedance coupling can as well be used to include spring and damper elements, it is computationally expensive due to inversion of higher order matrices. In addition to the bearing, elastic elements can as well be added to various locations, especially between holder and tool connections. In order to include these elastic elements the following equations are used

$$\begin{aligned}
[C_{11}] &= [A_{11}] - [A_{12}]\big[[A_{22}] + [K_{AB}]^{-1} + [B_{11}]\big]^{-1}[A_{21}], \\
[C_{12}] &= [A_{12}]\big[[A_{22}] + [K_{AB}]^{-1} + [B_{11}]\big]^{-1}[B_{12}], \\
[C_{21}] &= [B_{21}]\big[[A_{22}] + [K_{AB}]^{-1} + [B_{11}]\big]^{-1}[B_{21}], \\
[C_{22}] &= [B_{22}] - [B_{21}]\big[[A_{22}] + [K_{AB}]^{-1} + [B_{11}]\big]^{-1}[B_{12}],
\end{aligned} \tag{16}$$

$$[K_{AB}] = \begin{bmatrix} k_y{}^{AB} + i\omega c_y{}^{AB} & 0 \\ 0 & k_\theta{}^{AB} + i\omega c_\theta{}^{AB} \end{bmatrix}, \tag{17}$$

where $[K_{AB}]$ is composed of translation and rotational stiffness and damping elements. $k_y{}^{AB}$ and $k_\theta{}^{AB}$ are translational and rotational stiffnesses, and, $c_y{}^{AB}$ and $c_\theta{}^{AB}$ are translational and rotational damping coefficients of the flexible connection. It can be seen that Eq. (16) is very similar to Eq. (14) where the only difference is due to $[K_{AB}]$ term added into the equations.

### Stability Lobes

The first analytical formulation for milling operation is obtained by Budak [3, 4] . In the milling dynamics, two orthogonal degrees of freedom are assumed in the cutting operation as shown in Fig. 2. Equation of motion for milling is given below as,

$$\{F\}e^{i\omega_c t} = \frac{1}{2} a K_t \begin{bmatrix} \alpha_{xx} & \alpha_{xy} \\ \alpha_{yx} & \alpha_{xx} \end{bmatrix} [G(i\omega_c)]\{F\}e^{i\omega_c t}, \tag{18}$$

where $a$ is axial depth of cut, $K_t$ is cutting force coefficient, $[\alpha]$ is the matrix of average directional cutting coefficients and $[G(i\omega_c)]$ is the summation of tool point FRF and workpiece FRF matrices identified in the orthogonal cutting directions. For simplicity only tool point FRF matrices is used in this paper and workpiece is assumed as a rigid. $[G(i\omega_c)]$ and $[\alpha]$ is given as

$$[G(i\omega_c)] = \begin{bmatrix} G(i\omega_c)_{xx} & G(i\omega_c)_{xy} \\ G(i\omega_c)_{yx} & G(i\omega_c)_{yy} \end{bmatrix}, \tag{19}$$

$$\begin{aligned} \alpha_{xx} &= \frac{1}{2}\left[\cos 2\phi - 2K_r\phi + K_r \sin 2\phi\right]_{\phi_{st}}^{\phi_{ex}}, \\ \alpha_{xy} &= \frac{1}{2}\left[-\sin 2\phi - 2\phi + K_r \cos 2\phi\right]_{\phi_{st}}^{\phi_{ex}}, \\ \alpha_{yx} &= \frac{1}{2}\left[-\sin 2\phi + 2\phi + K_r \cos 2\phi\right]_{\phi_{st}}^{\phi_{ex}}, \\ \alpha_{xx} &= \frac{1}{2}\left[-\cos 2\phi - 2K_r\phi - K_r \sin 2\phi\right]_{\phi_{st}}^{\phi_{ex}}. \end{aligned} \tag{20}$$

Average directional cutting factors depend on $K_r$, $\phi_{ex}$ and $\phi_{st}$ which are radial cutting constant, entry angle and exit angle, respectively. Entry and exit angles are related to the cutting type (e.g. end milling, down milling and up milling).

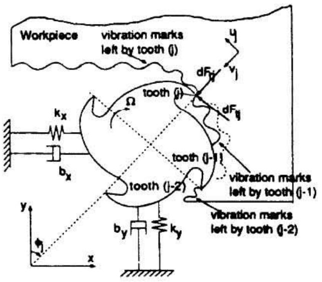

**Fig. 2** Cross Sectional View of an End Mill Showing Differential Forces [4]

Eq.(18) has a non-trivial solution if

$$\det\left[[I]+(\Lambda)\left([A_0][G(i\omega_c)]\right)\right]=0, \tag{21}$$

where

$$\Lambda = -\frac{N_t}{4\pi} aK_t(1-e^{i\omega_c T}), \qquad [A_0]=\frac{N_t}{2\pi}\begin{bmatrix} \alpha_{xx} & \alpha_{xy} \\ \alpha_{yx} & \alpha_{xx} \end{bmatrix}. \tag{22}$$

For orthogonal cutting condition off-diagonal terms $G(i\omega_c)_{yx}$ and $G(i\omega_c)_{xy}$ can be taken as zero. Then, using Eq. (21) eigenvalue $\Lambda$ can be found as

$$\Lambda = -\frac{1}{2a_0}\left(a_1 \pm \sqrt{a_1^{\,2} - 4a_0}\right), \tag{23}$$

where

$$\begin{aligned} a_0 &= G(i\omega_c)_{xx}G(i\omega_c)_{yy}(\alpha_{xx}\alpha_{yy} - \alpha_{xy}\alpha_{yx}), \\ a_1 &= \alpha_{xx}G(i\omega_c)_{xx} + \alpha_{yy}G(i\omega_c)_{yy}. \end{aligned} \tag{24}$$

FRFs at the tool point have complex values; hence, $\Lambda$ is a complex number. Since depth of cut must be a real value, $\Lambda$ is decomposed into real and imaginary components as $\Lambda = \Lambda_R + i\Lambda_I$. After some manipulations, to get only real valued depth of cut, real and imaginary part of $\Lambda$ should have the following proportion

$$\kappa = \frac{\Lambda_I}{\Lambda_R} = \frac{\sin \omega_c T}{1 - \cos \omega_c T}, \tag{25}$$

where $T$ is spindle period and $\omega_c$ is chatter frequency. Eq. (25) can be related with the spindle speed as follows [4],

$$\begin{aligned} &\omega_c T = \varepsilon + 2k\pi, \\ &\varepsilon = \pi - 2\psi, \\ &\psi = \tan^{-1}\kappa, \\ &n = \frac{60}{N_t T}. \end{aligned} \tag{26}$$

$\varepsilon$ is the phase shift between inner and outer modulations, $k$ is the corresponding vibration waves with in period, and $N_t$ is the tooth number. Finally stabile limiting depth of cut is found from Eq.(22) as,

$$a_{\lim} = -\frac{2\pi\Lambda_R}{N_t K_t}(1 + \kappa^2). \tag{27}$$

Eqs. (27) and (26) can be employed to find the related spindle speed for a given depth of cut or limiting depth of cut for a given spindle speed..

## Spindle Geometry

For a case study, the spindle-holder-tool model given by Erturk [8, 9] is used in this study. The material and geometrical properties of the spindle-holder-tool assembly are given in Table 1. At four locations, springs and dampers are added to simulate bearings. Location of each bearing and the corresponding stiffness values are given in Table 2.

**Table 1a** Spindle Dimensions [9]

| **Segment Number** | **1** | **2** | **3** | **4** | **5** | **6** | **7** | **8** | **9** | **10** |
|---|---|---|---|---|---|---|---|---|---|---|
| **Length (mm)** | 26 | 26 | 26 | 38 | 100 | 66 | 75 | 30 | 40 | 40 |
| **Outer Diameter (mm)** | 66 | 66 | 66 | 66 | 76 | 70 | 62 | 58 | 58 | 58 |
| **Inner Diameter (mm)** | 54 | 48 | 40 | 32 | 32 | 32 | 32 | 32 | 32 | 32 |

**Table 1b** Holder Dimensions [9]

| **Segment Number** | **1** | **2** | **3** | **4** | **5** | **6** |
|---|---|---|---|---|---|---|
| **Length (mm)** | 22 | 19 | 24 | 26 | 26 | 26 |
| **Outer Diameter (mm)** | 72 | 60 | 70 | 54 | 48 | 40 |
| **Inner Diameter (mm)** | 16 | 16 | 16 | 16 | 16 | 16 |

**Table 1c** Tool Dimensions [9]

| **Segment Number** | **1** | **2** |
|---|---|---|
| **Length (mm)** | 50 | 57 |
| **Outer Diameter (mm)** | 14 | 26 |
| **Inner Diameter (mm)** | 0 | 0 |

**Table 1d** Material Properties [9]

| | |
|---|---|
| **ρ (density)** | 7800 kg/m^3 |
| **ν (poisson ratio)** | 0.3 |
| **γ (damping factor)** | 0.003 |
| **E (Young's Modulus)** | 200 Gpa |

**Table 2a** Bearing and Interface Properties [9]

| | **Translational Stiffness (N/mm)** | **Rotational Stiffness (N/mm)** |
|---|---|---|
| **Front Bearings (for each)** | $7.5 \times 10^5$ | - |
| **Rear Bearings (for each)** | $2.5 \times 10^6$ | - |
| **Spindle Holder Interface** | $5 \times 10^7$ | $1.5 \times 10^6$ |
| **Holder Tool Interface** | $2 \times 10^7$ | $1.5 \times 10^6$ |

**Table 2b** Bearing Locations [9]

| Bearing No | Bearing 1 | Bearing 2 | Bearing 3 | Bearing 4 |
|---|---|---|---|---|
| **Distance (mm)** | 26 | 78 | 387 | 427 |

## RESULTS

After constructing the spindle-holder-tool assembly for specified geometrical and connection parameters, case study is performed considering different spindle speeds. First, spindle speed is taken as zero and corresponding natural frequencies and FRF of the tool point is obtained using the analytical model. Then spindle speed is increased to 20000 rpm and comparison is made with respect to zero spin speed. Stability lobes are constructed for both cases and change in the depth of cut is observed between two cases. In addition, finite element model (FEM) of the system is constructed in ANSYS and the results obtained are compared with results of the analytical model. In ANSYS, beam 188 element which uses Timoshenko beam model is used to model the spindle and combin 14 element is used to model bearing stiffness and damping.

Table 3 gives the comparison of natural frequencies obtained by the analytical method and FEM for zero spin speed.. Natural frequencies are obtained from the frequency response function which is determined by using 0.1 Hz increments in the finite element software. It is observed that the results for zero spinning speed are very close to the results obtained from the FEM. It should be noted that the maximum error compared to FEM is less than 1% in the first five modes.

**Table 3** Comparison of Natural Frequencies for Zero Spin Speed

| | Analytical Model | ANSYS | % Difference wrt FEM |
|---|---|---|---|
| **Mode 1** | 71.6 | 71.6 | 0.0 |
| **Mode 2** | 193.8 | 193.8 | 0.0 |
| **Mode 3** | 870.3 | 867.5 | 0.3 |
| **Mode 4** | 1430 | 1424.3 | 0.4 |
| **Mode 5** | 1764 | 1752.6 | 0.6 |

Dynamic characteristics of rotating beams change with respect to spinning speed. Natural frequencies split as backward and forward natural frequencies. As spinning speed increases, difference between backward and forward natural frequencies increases as well. In Table 4, comparison of natural frequencies between analytical method and FEM at 20000 rpm spin speed is given. In the analytical solution, the first two modes do not change, since they correspond to the rigid body modes of the spindle around bearings. In contrast, finite element solution splits them as forward and backward modes. If the elastic modes starting with the third mode are considered, analytical solutions also splits as backward and forward modes and their comparison with results of the FEM gives a maximum error less than 1% . Comparison of tool point FRF at 20000 rpm and 0 rpm, calculated by the analytical method, is given in Fig. 3. It can be seen that two FRFs are very close to the each other in general. If close investigation is done on the natural frequencies, forward and backward separation can be observed as shown in Fig. 4. The effect of separation of forward and backward frequencies on FRF is dominant only around the natural frequencies; whereas, other parts of the FRF are similar to the zero spin speed case.

**Table 4** Comparison of Forward and Backward Natural Frequencies

| | Backward Analytical | Forward Analytical | Backward FEM | Forward FEM | % Dif. Forward | % Dif. Backward |
|---|---|---|---|---|---|---|
| **Mode 1** | 71.3 | 71.3 | 70.3 | 72.9 | 1.4 | 2.2 |
| **Mode 2** | 193.8 | 193.8 | 190.2 | 197.7 | 1.9 | 2.0 |
| **Mode 3** | 867.5 | 872.7 | 862.9 | 871 | 0.5 | 0.2 |
| **Mode 4** | 1428 | 1433.8 | 1422.2 | 1425.8 | 0.4 | 0.6 |
| **Mode 5** | 1751.5 | 1774.3 | 1734.9 | 1769.5 | 0.9 | 0.3 |

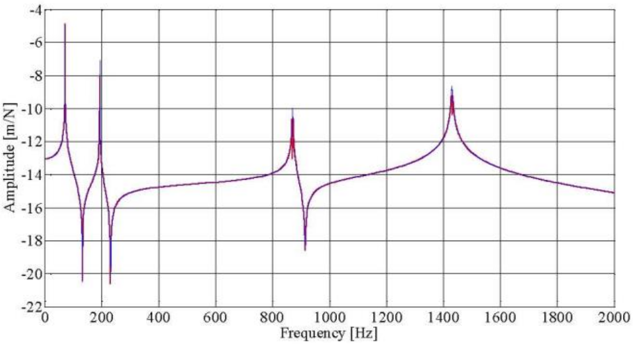

**Fig. 3** Comparison of Tool Point FRF at 20000 rpm and 0 rpm

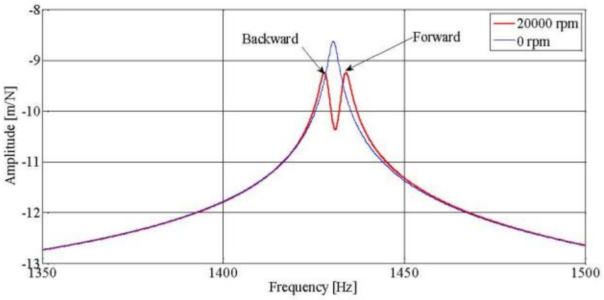

**Fig. 4** Separation of Forward and Backward Modes

Stability lobe for the case study given is constructed by considering the rotational speed of the tool. The spindle speed is 20000 rpm; hence depth of cut at 20000 rpm is the main focus point in the stability lobe diagram. Depth of cut at 20000 rpm is investigated for by including and excluding the effects of the spin speed. Cutting parameters are taken from [5]. The results obtained are given in Fig. 5. It is observed that depth of cut increases from 10% at 20000 rpm spindle speed if spin speed effects are included. As a result of this, depth of cut can be increased this also increases the material removal rate.

## CONCLUSIONS

Effect of spindle speed on the dynamics of milling operation is investigated in this paper. A Timoshenko beam model is used to model different cross sectioned beams and receptance coupling method is employed to construct the complete spindle model. Spring and dampers are added to various locations using structural modification method in order to include the effect of bearings used. It is observed that, addition of spindle speed into the model, natural frequencies of the spindle split into two parts forward and backward natural frequencies. The results obtained for the elastic modes are in good agreement with the finite element solution. Using the analytical model developed stability lobes are obtained for spin speed of 0 rpm and 20000 rpm which are compared with each other. It is observed that 10% increase in depth of cut is obtained by including the gyroscopic effects into the formulation.

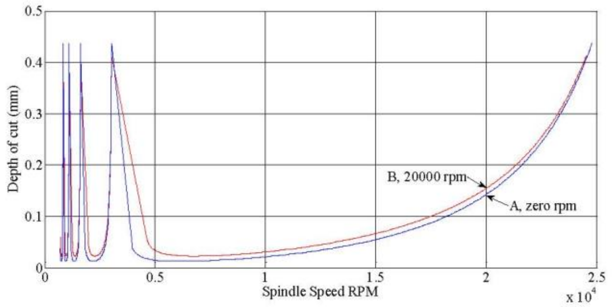

**Fig. 5** Comparison of stability Lobes at Zero and 20000 rpm

## REFERENCES

1. **Tobias, S.A. and Fishwick, W.** The chatter of lathe tools under orthogonal cutting conditions. *Trans. ASME.* 1958, Vol. 80, pp. 1079-1088.

2. **Tlusty, J. and Polacek, M.** The stability of machine tools against self-excited vibrations in machining. *Proceedings of ASME International Research in Production Engineering, Pittsburg, USA.* 1963, pp. 465-474.

3. **Budak, E.** Analytical models for high performance milling. Part I: Cutting forces, structural deformations and tolerance integrity. *International Journal of Machine Tools and Manufacture.* 2006, Vol. 46, pp. 1478-1488.

4. **Budak, E.** Analytical models for high performance milling. Part II: Process dynamics and stability. *International Journal of Machine Tools and Manufacture.* 2006, Vol. 46, pp. 1489-1499.

5. **Altintas, Y.** *Manufacturing Automation.* s.l. : Cambridge University Press, 2000.

6. **Zu, J.W. and Han, P.S.,.** Natural Frequencies and Normal Modes of a Spinning Timoshenko Beam With General Boundary Conditions. *Journal of Applied Mechanics.* 1992, Vol. 59, pp. 197-204.

7. **Özgüven, H.N.** A new method for harmonic response of nonproportionally damped structures using undamped modal data. 1987, Vol. 117, pp. 313-328.

8. **Ertürk, A.** Dynamic modeling of spindle-tool assemblies in machining centers. *M. Sc. Thesis, METU Mech. Eng. Dept.* 2006.

9. **Ertürk, A. Özüven, H.N. and Budak, E.** Analytical modeling of spindle-tool dynamics on machine tools using Timoshenko beam model receptance coupling for the prediction of tool point FRF. 2006, Vol. 46, pp. 1901-1912.